Radiation Dosimetry
of
Irregularly Shaped Objects

by Jonathan Griffin

Submitted for the degree of Master of Science in Medical Physics
at the University of Canterbury
August 2006

Abstract

Electron beam therapy planning and custom electron bolus design were identified as areas in which improvements in equipment and techniques could lead to significant improvements in treatment delivery and patient outcomes.

The electron pencil beam algorithms used in conventional Treatment Planning Systems do not accurately model the dose distribution in irregularly shaped objects, near oblique surfaces or in inhomogeneous media. For this reason, at Christchurch Oncology Centre the TPS is not relied on for planning electron beam treatments.

This project is an initial study of ways to improve the design of custom electron bolus, the planning of electron beam therapy, and other radiation therapy simulation tasks, by developing a system for the accurate assessment of dose distributions under irregular contours in clinically relevant situations.

A shaped water phantom system and a diode array have been developed and tested. The design and construction of this water phantom dosimetry system are described, and its capabilities and limitations discussed.

An EGS/BEAM Monte Carlo simulation system has been installed, and models of the Christchurch Oncology Centre linacs in 6MeV and 9MeV electron beam modes have been built and commissioned.

A test was run comparing the EGS/BEAM Monte Carlo system and the CMS Xio conventional treatment planning system with the experimental measurement technique using the water phantom and the diode array. This test was successful as a proof of the concept of the experimental technique.

At the conclusion of this project, the main limitation of the diode array system was the lack of data processing software. The array produces a large volume of raw data, but not enough processed data was produced during this project to match the spatial resolution of the computer models. An automated data processing system will be needed for clinical use of the array.

It has been confirmed that Monte Carlo and pencil-beam algorithms predict significantly different dose distributions for an irregularly shaped object irradiated with megavoltage electron beams. The results from the diode array were consistent with the theoretical models.

This project was an initial investigation. At the time of writing, the diode array and the water phantom systems were still at an early stage of development. The work reported here was performed to build, test and commission the equipment. Additional work will be needed to produce an instrument for clinical use. Research into electron beam therapy could be continued, or the equipment used to expand research into new areas.

Acknowledgements

This project would not have been possible without the help of many people.

Graham Sorell had the original idea of using a water tank and patient immobilisation masks to measure the dose distribution under and within irregularly shaped objects.

Mat Hasler supervised the project, assisted with the water phantom and diode array experiments, and proofread and advised on the thesis.

Steve Morgan took over day to day supervision of the project when Mat departed from Christchurch.

Deloar Hossain taught me the art of Monte Carlo simulation. His knowledge and experience with Linux, EGS/BEAM and associated software was immensely helpful. The Monte Carlo section of this project could not have been done without him.

Steve Sylvander was the first to work on Monte Carlo simulation at Christchurch Oncology, trialling GEANT4.

Lou Reinisch was my supervisor at Canterbury University, helping with administrative and academic matters, advising on the direction of the project and reviewing the thesis.

Dave Pinchin designed a diode-based radiation detector as a QA tool some years ago. For this project, Dave modified that design and built the prototype diode radiation detector.

After the prototype radiation detector was tested and refined, Geoff Graham built the diode array.

Neville Turner, Chris Roberts, Johann Bader, Brian Temple and Brian Connell in the Christchurch Hospital mechanical workshops built all the phantoms and mounts for this project, including the mask mounts for the water phantom, the CT mask phantom, the angular dependence 'mushroom' phantom and the diode detector mounts.

Ray Pointon helped to get me started on Matlab.

Mat Hasler, Deloar Hossain and Mark Bird trained me in the use of Xio.

Mark Bird, Dave Rogers and Jenny Lydon advised and helped with the revisions to make this final version of the thesis.

Thank you all for your assistance and advice.

Contents

List of Figures

1 Introduction

The aim of this project was to develop a system for accurate assessment of dose distribution under irregular contours in clinically relevant situations.

Electron beam therapy is used as a treatment for superficial cancers. The depth dose of an electron beam has a narrow build-up region, a high dose plateau, and then a steep drop in dose with increasing depth (Fig 1). The build-up region gives a skin-sparing effect, and the steep drop off at depth spares deeper tissues. The high dose plateau increases in depth with increasing beam energy. These characteristics make electrons suitable for superficial therapy.

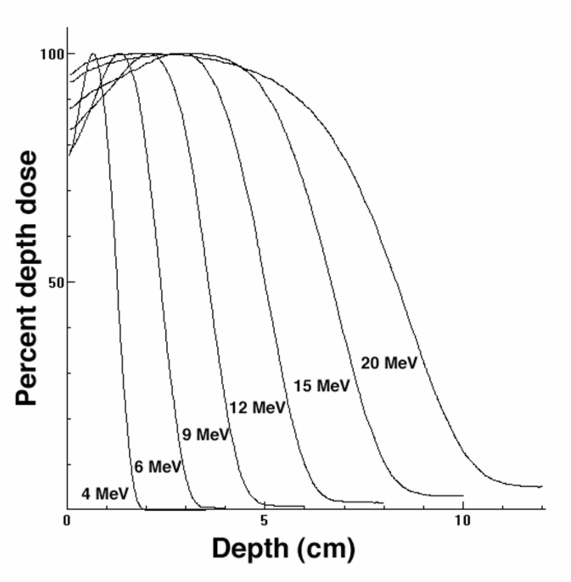

Figure 1: Relative depth dose curves for electron beams over a range of energies. *Reproduction of Fig 8.4 from [8].*

Skin lesions and other superficial cancers can occur on irregularly shaped body parts, such as the head, face and neck. The irregular shapes make it difficult to plan and administer an optimum radiation dose to the treatment site. The algorithms used in conventional Treatment Planning Systems (TPS) do not accurately predict the dose distribution in irregularly shaped objects [1].

In cases where the shape of the treatment site adversely affects the dose distribution, material called bolus can be placed on a patient's skin to alter the apparent shape of the body and allow improved treatment. Fig 2 shows the effect of bolus on the electron beam depth dose. The depth dose curve starts from the surface of the bolus, so from the point of view of the underlying patient tissue, the depth dose is shifted up. The skin dose is increased, and the dose at depth (below the target volume) is reduced. Bolus that has been designed for treatment of a specific site for an individual patient is called custom electron bolus (see Fig 3).

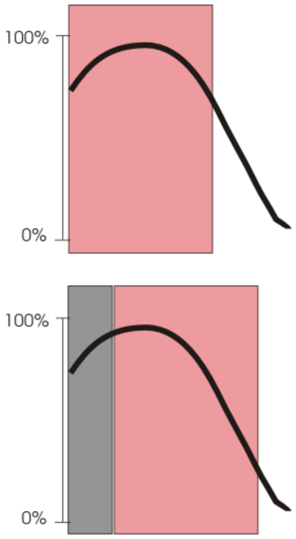

Figure 2: Electron beam depth dose curves without and with bolus in place.

At Christchurch Hospital, custom electron bolus is designed manually from information such as measured depth dose curves. The CMS Xio treatment planning system used in Christchurch can only simulate bolus with very simple shapes.

This project was an initial study of ways to incorporate immobilisation masks into scanning water phantom measurements in order to to improve the design of custom electron bolus, the planning of electron beam therapy, and other radiation therapy simulation tasks.

In order to rapidly build a three dimensional dose map in these situations, a diode detector array has been developed. The array can be mounted on an existing commercial water tank system which allows the whole array to be scanned in three dimensions. The original water tank was designed for performing Quality Assurance (QA) tests on linear accelerators.

The design, construction and testing of the water tank system is de-

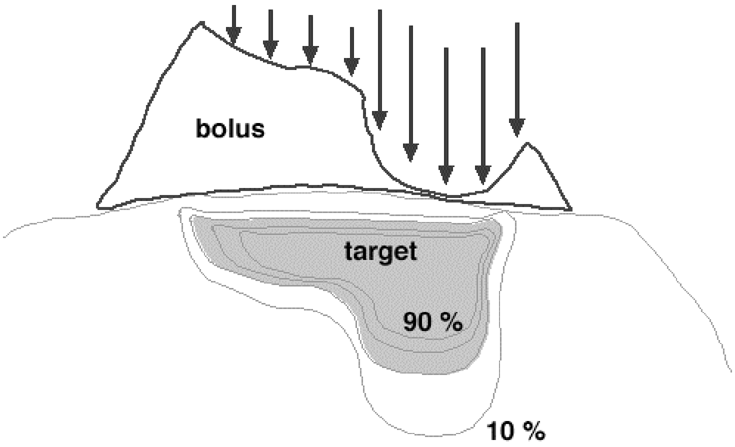

Figure 3: Custom or conformal bolus permits the patient anatomy and the treatment volume to have different shapes. The patient or distal surface of the bolus matches the shape of the patient's body. The beamward or proximal surface is shaped to match the dose distribution to the Planned Treatment Volume (PTV). *Reproduction of Fig 8.10 from [8].*

scribed in Sections 3 and 5.

Given the previously mentioned limitations of the Xio pencil beam algorithm (described in more detail in Section 2), the scope of the project was extended to include Monte Carlo simulations of the irradiation configurations investigated with the diode array. This should give the most accurate theoretical representation of the dose distribution for the purpose of validating the performance of the detector array.

Monte Carlo based treatment planning systems are currently considered the best replacement for conventional treatment planning algorithms. EGS/BEAM is the preferred Monte Carlo software for radiation therapy research. Work on simulating radiotherapy linear accelerators (linacs) with EGS/BEAM is reviewed, as are comparisons between EGS/BEAM and other Monte Carlo software.

Work on simulating the Christchurch Hospital linacs with EGS/BEAM is presented. Comparisons between Monte Carlo simulations, plans made with the conventional Xio TPS, and experimental results obtained with the water tank system have been made.

A system for manufacturing shape-modifying custom electron bolus has already been developed by a team at the University of Texas. A literature review of this work is presented in Section 2.2. The Texas University group uses a special treatment planning system called COPPERPlan. This software was written in-house and uses the pencil-beam algorithm for modelling electron beams.

This project is an initial investigation. The experiments reported here were performed to build, test and commission the equipment for further use. Future work could improve the water tank dosimetry system and the EGS/BEAM Monte Carlo capabilities. Research into electron beam therapy could be continued, or the equipment used to expand research into new areas.

2 Literature Review

There is a vast body of published scientific literature on subjects relevant to this project, which include electron beam therapy, cancer of the head and neck, radiation detectors and phantoms for use in radiation therapy, amplifiers and signal processing, and Monte Carlo software.

Accordingly this will be a brief review of only the most relevant papers found.

2.1 Electron Beam Modelling Theory

Theoretical models of electron beams and the interaction of beams with matter are of interest for basic scientific reasons and for treatment planning. A radiation therapy prescription specifies a desired dose and a volume of tissue to irradiate. Treatment planning determines the best way to achieve the prescription.

Theoretical models for predicting the interaction of electron beams with matter have been a subject of continuous research since electron beam therapy came into common use more than 50 years ago.

The first step in electron beam modelling was an algorithm to describe the central axis depth dose, proposed in 1953 [4]. In the following decades a number of analytical models were proposed to predict dose distributions using algorithms and empirical data or parameters. A theory based on diffusion was the subject of a number of publications [4].

The most successful analytical model to date is the Pencil Beam Algorithm by Hogstrom *et al* (1981). This model is used by current treatment planning systems such as CMS Xio [1]. The Hogstrom pencil beam algorithm as used in Xio is discussed briefly below.

The Monte Carlo modelling technique has long been considered the best approach to modelling a probabilistic system like radiation interacting with matter. Historically the use of Monte Carlo was restricted by the available computer technology [2]. As computer technology has improved, research into and use of Monte Carlo techniques has expanded. The use of Monte Carlo in radiation therapy modelling, and the EGS/BEAM system in particular, is reviewed below.

2.1.1 Pencil Beam Model

The Electron Pencil Beam Model is an algorithmic system that models dose distribution in a phantom or patient by dividing the incident beam into many beamlets.

The properties of each pencil beam, such as intensity profile, are represented by functions. These are convolved [5] with other functions representing the effects of interactions with such things as air in the beam path, collimators, and eventually the phantom material or patient [1]. The various parameters of these functions are determined empirically for each radiotherapy machine at commissioning time.

In the CMS Xio treatment planning system, relative depth doses imported from the linac commissioning data are used as the basis for beamlet models (consequently, the central axis depth dose at the standard source-to-surface distances will always be perfect). Comparison is then made between measured beam profiles and the predictions of the pencil beam algorithm. The aim of the comparison is to tweak the modelling parameters to give as close a match as possible between the measured and calculated beams.

One parameter adjusts the divergence of the pencil beams (which are modelled as having a Gaussian cross section) and another controls the spread of scatter radiation in the outer penumbra of the beam. These two parameters affect the shape of the penumbral region on the edge of the beam. The user can also alter the intensity across the whole beam profile by supplying (through a graphical interface) a set of points specifying radius from the beam centre and a factor to adjust the intensity at that radius. The last method is used to arbitrarily compensate for the beam profile not being ideally flat across the centre. This procedure must be performed for all beam energies, with all applicator sizes, and commonly used SSDs.

The convolved algorithm is used to calculate the resulting depth dose of each pencil beam, and these results are combined to give the dose distribution from the entire electron beam.

In the Xio treatment planning system, the equation representing the overall process of convolving the electron pencil beam intensity distribution is [1]:

$$
\begin{aligned}
D(x,y,z) = &\int_{-\infty}^{+\infty}\int_{-\infty}^{+\infty} S_{air}(x'',y'',z) * \frac{1}{2\pi * fmcs * \sigma_{MCS}^2(x'',y'',z)} * \\
&* \exp\left\{ -\frac{(x-x'')^2+(y-y'')^2}{2 * fmcs * \sigma_{MCS}^2(x'',y'',z)} \right\} * \\
&* G_{H_2O}\big(0,0,Z_{eff}(x'',y'',z)\big)\left\{\frac{SSD_{beam}+Z_{eff}(x'',y'',z)}{SSD_{beam}+z}\right\}^2 dx''dy'' + \\
&+ D_{photon}\big(x,y,Z_{eff}(x,y,z)\big) \qquad (1)
\end{aligned}
$$

where:

$Z_{eff}(x'',y'',z)$	is the effective depth of a point.
$fmcs$	is the factor by which the scattering variance in the medium is multiplied at each depth.
$\sigma_{MCS}^2(x'',y'',z)$	is the scattering variance due to multiple Coulomb scattering in the medium.
$S_{air}(x'',y'',z)$	is the air-convolved intensity distribution.
$G_{H_2O}(0,0,Z_{eff})$	is the central axis dose in water.
D_{photon}	is the component of the dose due to photons.
SSD	is the source to surface distance.

A brief description of the modelling process follows; the complete set of equations and description of how the algorithm works is available in the software manual [1] and has not been reproduced here.

Modelling of the pencil beamlets starts from the final plane of collimation. Electron and photon dose contributions are separated in the calculations. The calculation of the (minor) photon contribution is much simpler than the calculation of the electron contribution, and is not covered here.

- The initial electron intensity distribution is modified by convolution to include the effects of an electron cutout (or other 'customised port') and scatter in the collimators.

- The intensity distribution function is convolved with a function describing the scattering of the beam in air.

- Central-axis relative depth dose and inverse square law factors are included.
- A function describing the scatter of electrons in the medium is convolved with the intensity distribution. Information about the medium composition is included at this stage.

The initial intensity distribution, in-air scatter and medium scatter are all Gaussian functions. Electron dose and photon dose components are summed to give the total dose. This completed algorithm describing the simulation is evaluated for each point in a three dimensional grid. The density of points in the grid and the volume it covers can be adjusted by the user. Grid points are not vertically aligned, they are aligned along the same diverging rays that the pencil beams follow.

For each point, measured sample beam data is deconvolved into the components described above, combined with the parameters describing the point location being simulated, the algorithm is convolved and evaluated to give the calculated dose at that point. For each pencil beam (or point), the attenuating material varies only with depth. The algorithm contains the assumption that any inhomogeneities are infinite in lateral extent. This leads to local inaccuracies in the calculated dose. *"…Pencil-beam algorithms have been proved useful for broadbeam electron dose calculations in radiotherapy. However, all pencil-beam models encounter significant limitations (i.e., lateral discontinuities as well as those in depth) when applied to nonslab geometries… This error results from the basic assumption that the different materials along the central axis of each pencil beam are infinite in their lateral extent for the purpose of determining the dose to the patient from that pencil beam…"* [K. R. Hogstrom, 1991]

This and other approximations made to reduce the computational workload of the pencil beam model give it an accuracy of ±4% in ideal circumstances, with errors from 10% to 20% in extreme situations.

2.1.2 Monte Carlo Technique

The Monte Carlo method is widely accepted as the most accurate method for modelling radiotherapy treatments [2, 3].

Algorithmic modelling is a top-down approach of finding a function that fits the observed macroscopic properties and behaviour of a system. Monte

Carlo is a bottom-up technique which involves modellng the interactions of a very large number of individual particles.

The Monte Carlo technique was named after a famous casino in Monaco, and like the casino, the technique works on statistical probabilities. Any given particle moving through a material has a certain probability of undergoing each of the possible interactions. Each interaction has a range of possible outcomes. Particles produced by one interaction may undergo subsequent interactions, until all the energy of the incident radiation is absorbed by the target material [3].

By modelling a very large number of particles, macroscopic properties like the distribution of absorbed dose in a material can be determined with high statistical accuracy.

A Monte Carlo program consists of a source of random numbers (often a random initial seed and a pseudorandom algorithm for generating more numbers) and probability functions that represent the processes occurring in a system (Compton scattering for example) and yield results consistent with those processes.

There are, of course, many ways to implement physical processes in computer code using this general technique. So of the number of independent Monte Carlo programs available for radiation therapy applications, not all programs are suitable for all applications, and different programs can give different results from the same initial conditions [21].

It is generally believed that the use of fundamental physics and statistics makes Monte Carlo an inherently more accurate method of modelling.

2.2 Custom Electron Bolus

Cancers of the head, face and neck can be difficult to treat with radiation therapy. The difficulties include small, shallow treatment volumes, proximity to sensitive organs such as glands and mucosa, and irregularly shaped and inhomogenous treatment volumes, especially where surgery has been performed.

A range of techniques has been used to administer radiotherapy in these situations. Combinations of photon and electron beams, multiple electron beams with different energies and wedges have been used [7].

Bolus is an important tool in these treatments. As previously described, bolus shifts the depth dose curve in underlying tissue (Section 1).

Electron bolus has been defined by Hogstrom as *"a specifically shaped material, which is usually tissue equivalent, that is normally placed either in direct contact with the patients skin surface, close to the patients skin surface, or inside a body cavity. This material is designed to provide extra scattering or energy degradation of the electron beam. Its purpose is usually to shape the dose distribution to conform to the target volume and/or to provide a more uniform dose inside the target volume"* [6].

Custom or conformal bolus is more complicated than a simple slab (see Fig 3). The patient surface of the bolus has to be molded to the shape of the treatment site. The beamward side of the bolus must be shaped to achieve the desired dose distribution at the treatment site.

A system has been developed and tested by a group at the Department of Radiation Physics and Department of Radiation Oncology, The University of Texas and M. D. Anderson Cancer Center, for manufacturing conformal bolus to enable delivery of improved electron beam therapy to superficial treatment sites. The main application for this bolus shaping technology so far is treatment of sites on the head and face [7], although it has also been used for post-mastectomy treatment of the chest wall [9].

The treatment process developed by the Texas group can be summarised as follows:

1. **CT data acquisition**
   The patient is positioned and fitted with immobilisation equipment. The patient is scanned using Computed Tomography (CT) to obtain a 3D model of them.

2. **Initial plan for bolus design**
   The CT data is used to define the planning target volume (PTV). This is done by oncologists, using the Pinnacle TPS. The data is transferred to another TPS, called COPPERplan, which was written in-house by the researchers. COPPERplan uses a pencil-beam algorithm for electron treatment simulation. The conformal bolus is designed in COPPERplan using a set of operators. There are bolus creation operators, bolus modification operators and bolus extension operators.

3. **Bolus fabrication**
   The bolus shape has to be transferred from the TPS to a computer controlled milling machine via CAD/CAM software. The bolus ma-

terial was modelling wax. The milling procedure takes several hours. Fig 4 shows both sides of a piece of bolus made for treatment of a site on the neck.

4. **Bolus QA and final plan**
   Once the bolus has been made, the patient is scanned by CT again with the bolus in place (Fig 5). This CT data is loaded into the Pinnacle TPS. Remodelling the treatment with the bolus in place in the Pinnacle system provides verification of the COPPERplan model.

5. **Treatment**
   Treatment is typically given in daily fractions, with a single field in each fraction. Each custom bolus can only be used for a single field - meaning one beam from one direction. Conventional treatment plans often use multiple beams from different angles.

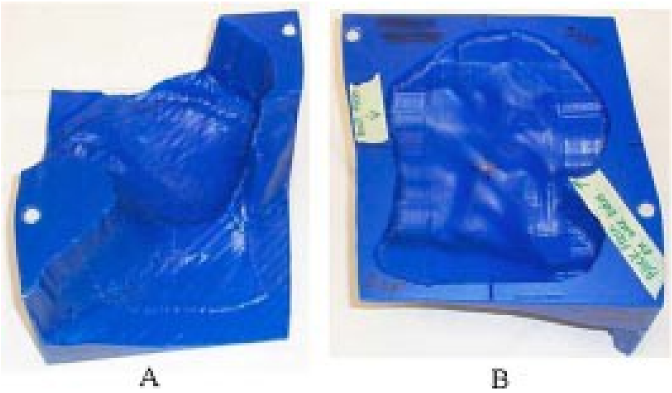

Figure 4: **A:** Distal surface. The patient surface, shaped to fit the surface of the patient. **B:** Proximal surface. The beamward surface of the bolus, shaped to give the desired dose distribution. *Reproduced from [7].*

In cases where a therapeutic dose is not required at the skin surface, bolus can also have undesirable effects on the dose distribution. When bolus is used, the skin sparing effect of the build-up region of an electron beam in tissue is lost. Skin erythema and moist desquamation are side effects that have resulted from irradiation using the conformal bolus technique [9, 7]. In some cases, some fractions of the electron treatment have been replaced with x-rays to reduce skin damage.

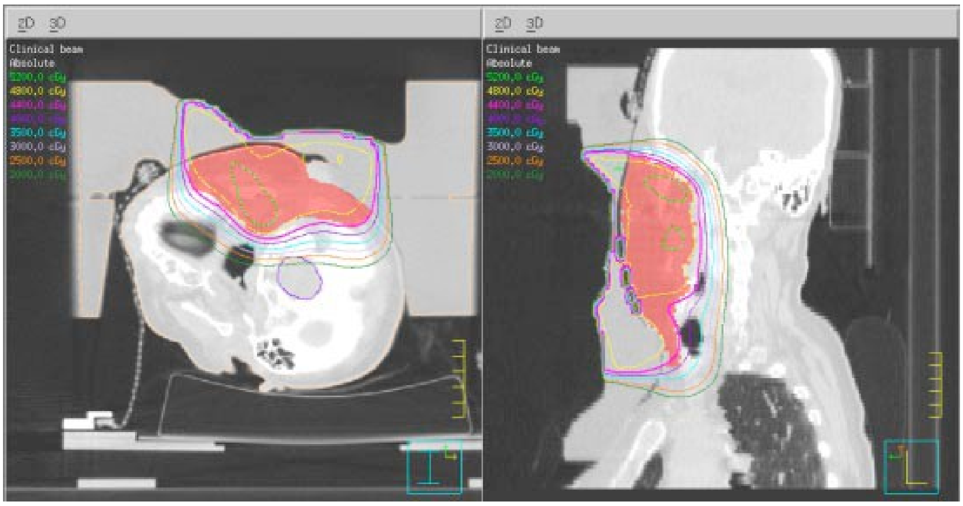

Figure 5: Bolus design is verified by scanning the patient in CT with the bolus in place, and simulating treatment of the patient with bolus in the Pinnacle TPS. The pink area depicts the Planning Target Volume. *Reproduced from [7].*

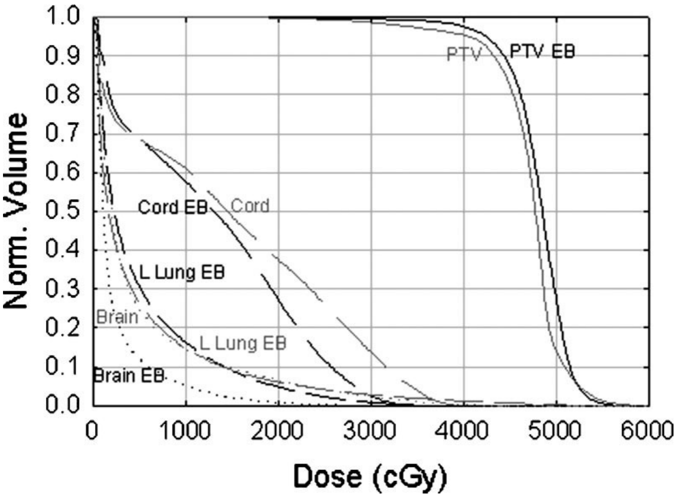

Figure 6: A Dose Volume Histogram comparing the head and neck treatment shown in Fig 5 with a conventional electron beam treatment for the same area. Black lines labelled 'EB' denote the results of treatment using custom electron bolus. *Reproduced from [7].*

A 1cm thick ring shaped lead shield can be placed between the patient's skin and the bolus to minimise enlargement of the electron penumbra by scatter from the bolus at the edge of the treatment field. This collimation can reduce the dose to critical structures without reducing the dose to the PTV [10].

COPPERPlan Treatment Planning System

The COPPERPlan TPS [11] uses a variation of the pencil beam algorithm described above (Section 2.1.1) for modelling electron beams. Operators have been added to the TPS for designing custom electron bolus. These operators will be described only briefly here, for contrast with the methods used in this project.

Bolus creation operators add bolus to each pencil beam fan line to give a constant distance from the proximal bolus surface to the distal surface of the treatment volume. Operators work on either physical distance or water-equivalent distance. Bolus modification operators edit existing bolus, changing the thickness along fan lines to meet user-defined constraints, such as a maximum dose at the proximal surface of a critical structure. Bolus extension operators set the thickness of bolus beyond the lateral extent of the treatment volume, avoiding sharp changes in bolus thickness.

These operators do not guarantee the best possible bolus design for any given plan, and multiple designs for the same treatment plan can differ significantly depending on the order the bolus operators are applied in.

Bolus materials

A number of materials can be used as bolus. The Texas group uses a type of modelling wax, which is milled to shape. At Christchurch, another type of wax is softened by heating and manually shaped. A commercial dental molding material has also been evaluated for use as bolus [12]. Bolus material is preferably equivalent to tissue for interactions with radiation, so that it does not perturb the beam in undesirable ways, and can be reliably modelled in treatment planning systems. A material that can be easily shaped but can also hold a given shape is also desirable. Dental molding material is of interest because it can be manually shaped at body temperature, and so can be shaped directly on the patient's skin.

2.3 Monte Carlo for Radiation Therapy

Several Monte Carlo programs have been used for radiation therapy simulations, including MCNP, XVMC, GEANT4 and EGS. Papers relating to the two most promising Monte Carlo software packages are reviewed here. EGS is of the most interest in this project, as it is a popular choice for radiotherapy simulations, and was chosen as the software for the Monte Carlo component of this project.

Methods of modelling radiotherapy linear accelerators are the focus of the review. The actual accelerating waveguide and associated beamline components are never modelled. The linac head is sometimes modelled in detail, but simplified radiation sources, stored data from prior simulations and non-Monte Carlo algorithms have been used with success.

2.3.1 GEANT4 and EGS/BEAM

GEANT4 is a relatively new Monte Carlo toolkit that has been used for modelling radiation transport over a wide energy range. A paper has been published which compares three models available in GEANT4 that are suitable for radiotherapy simulations, the standard, low energy and Penelope models, with EGSnrc [21].

The paper discusses how GEANT4 models the interaction processes of photons (the photoelectric effect, Compton scattering, pair production and Rayleigh scattering) and electrons (including ionisation, Bremsstrahlung and scattering). The data used by the GEANT4 models, for example the mass attenuation coefficients and stopping powers for each process, was compared to data from other sources, such as ICRU publications and the PEGS4 data used by EGS/BEAM.

A variety of simulations were run: monoenergetic electron and photon beams, and model clinical beams, onto flat water phantoms, air interfaces, and materials that are often found in linacs, such as aluminium and tungsten. The results varied between the three physics models, but the authors found the electron transport mechanics were not sufficiently accurate for radiotherapy simulations, although their requirement of 2% accuracy is sometimes not attained by conventional radiotherapy treatment planning systems.

GEANT4 was found to be satisfactory for simulations where electron transport is not of critical importance, and it was noted that the software is still being improved and updated.

2.3.2 About EGS/BEAM

The first version of the Monte Carlo simulation software that became EGS (Electron Gamma Shower) was written in the early 1960s [33]. EGS models coupled photon, electron and positron interactions with matter. The latest version of EGS at the time this thesis was written, EGSnrcMP, from a group at the National Research Council of Canada, is popular for medical physics applications, especially radiation therapy simulations. A large part of this popularity is due to the BEAM package. The BEAM package is described in more detail in Section 4.

2.3.3 Modelling Linear Accelerators

EGS, and Monte Carlo software in general, allows the user freedom to create whatever geometric structure they desire to simulate, with relatively few restrictions. This freedom extends to the geometry and other characteristics of radiation sources. This means there are many options to consider even when the system to be simulated is a known, specific object like a linac.

The most obvious approach is to reproduce the entire structure of the linac in the simulation (see Fig 7 for an example). This was the approach used by researchers at NRC for modeling medical linacs as part of the development and testing of BEAM [32]. In that work, linacs from several manufacturers were modelled, and electron beams from 5MeV to 50MeV simulated and compared to measured data. One of these linacs was a Varian 2100C, similar to the linacs used in this project. The accelerator beamline, including the waveguide and bending magnet, was not modelled. The narrow, high energy, monoenergetic electron beam exiting the bending magnetic was the starting point for the simulations. All components of the linac head which intersect the beam path were modelled. Good results were obtained, closely matching the measured beam data.

Simulated particle ‘histories’ were recorded in phase space files, and the origin of each particle recorded in the LATCH section of the history. The LATCH feature allowed particles produced in different components of the linac to be isolated. For example, an energy spectrum just of electrons produced in interactions with applicator scrapers can be plotted.

A phase space file records all parameters of particles incident on a specified plane in the simulation. A phase space file can also be used as the source of particles in a simulation. So separate simulations can be combined by using phase space files. In this way, a given system or object does not have to be simulated all at once.

Later work at NRC using the EGS/BEAM software followed a similar approach, but simulated photon beams, and extended the modelling of linear accelerators to deriving the linac structure from measured data such as beam profiles and depth doses [17, 18]. This information was considered to be more easily accessible than complete and accurate plans of linac heads, which may be proprietary information.

That work verified BEAM simulations of linac heads by comparing simulated depth dose curves, off-axis factors and energy spectra with existing compilations of measured data. Simulation parameters were also varied to determine which parameters had the greatest influence on the dose distribution and energy spectrum. In addition, the LATCH and ZLAST features were used to determine the proportion of the scatter particle fluence emitted by individual components of the linac.

Another approach is to simulate the radiation beam with analytic algorithms while simulating the dose distribution in patients and phantoms by Monte Carlo calculation [16]. The calculated radiation source used in that paper to simulate megavoltage photon beams consisted of two Gaussian-shaped photon sources, corresponding to the target and the flattening filter, and a uniform source of electron contamination also located at the flattening filter. This radiation source was designed to match measured dose distributions, with only some geometric parameters obtained from linac manufacturers' documentation. The analytic source model was compared with measurements and BEAM simulations. The Monte Carlo software used for calculating the dose distribution in phantoms was XVMC. This modelling technique was called Virtual Energy Fluence modelling, and the authors believe use of standard measurements, and the reduced computational workload compared to full simulation of a linac head, make this a potentially useful technique for future treatment planning systems.

A similar approach was taken in the development of the first commercial, Monte Carlo based, IMRT treatment planning system, PEREGRINE [19]. PEREGRINE does not model the entire linac head either. BEAMnrc linac simulations were used to create a radiation source composed of a set of histograms representing the properties of each of four source components.

PEREGRINE generates particles with parameters from the histogram data, and uses Monte Carlo calculations to model particle transport through collimators (jaws and a MLC) and determine the dose distribution in a patient or phantom.

A range of tests were done comparing PEREGRINE to EGSnrc calculations and experimental measurements. The experimental measurements used water phantoms, solid water phantoms and heterogenous solid slab phantoms made up of slabs of material equivalent to water, bone and lung tissue. A combination of ion chambers (NACP and Exradin A14P), diodes (Scanditronix shielded photon diodes, since this work investigated 6MV photon beams for IMRT) and TLD700 thermoluminescent dosimeters were used.

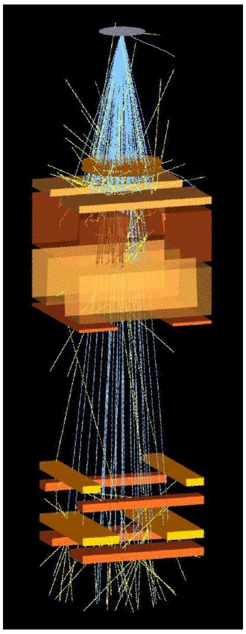

Figure 7: BEAM simulation of a 20MeV electron beam from an AECL Therac 20 linac. The design of this AECL linac head is quite different from the Varian linacs used in this project. *Reproduced from [29].*

2.4 Experimental Techniques

Determining the actual dose distribution within a patient during radiation therapy is very difficult. Inserting and accurately positioning radiation detectors within a human body is impractical, and would be invasive and unpleasant for the patient.

Experimental techniques have been developed for testing the accuracy and precision of computerised treatment planning systems using phantoms with varying levels of geometric complexity and anthropomorphic accuracy.

Treatments can be planned for the simple phantoms commonly available for QA testing, such as flat field water tanks and plastic (eg. solid water) blocks [13]. But these tests do not simulate the geometric complexity and inhomogenous composition of a human body.

Simple solid phantoms can be modified to include examples of geometry that cause problems for treatment planning systems [15]. In that paper, as well as simulating tissue with epoxy resin, wax bolus was simulated by pieces of PMMA (perspex).

A more complex phantom was developed for experimental verification of megavoltage photon beam treatment planning and delivery [14]. The phantom consisted of a solid central block flanked by two sealed water phantoms. Markers defining a target volume can be inserted in the central block. This phantom was used for comparing treatment planning and delivery for prostate cancer between several radiotherapy facilities. A similar plan was developed at NRL, in which a commercial anthropomorphic chest phantom and MOSFET dosimetry system would be used to compare lung treatments at facilities around New Zealand.

Using an anthropomorphic phantom such as the RANDO (Alderson Research Labs, Stanford, CA.), which has the shape of a generic human torso, inclusions simulating the lungs, and a real human skeleton, is another option.

Thermoluminescent dosimeters (TLDs) are commonly used as the radiation detectors in experiments using complex phantoms [15], because of they are small and do not need cables. Film is also used [13] for similar reasons. TLDs are usually calibrated by intercomparison with an ionisation chamber.

2.5 Diodes

Silicon diode dosimeters designed for use in radiation therapy commonly have shielding built in to attenuate low energy x-rays. Photoelectric absorbtion of low energy x-rays by materials increases with increasing atomic number. The atomic number of silicon is significantly greater than the effective atomic number of human tissue or substitutes such as water and tissue equivalent plastic. So an unshielded silicon diode detector will report a higher absorbed dose from low energy x-rays than tissue or an equivalent phantom would actually receive.

In the high energy photon and electron beams used for radiotherapy, low energy x-rays are produced in the phantom or patient from interactions with the primary beam. Consequently this dose enhancement effect is most noticeable in large fields, where there is a large volume of irradiated material.

The metal shielding, however, enhances production of secondary electrons in the detector, and scatters electron beams more strongly than semiconductor or tissue equivalent material. These effects can cause errors in dose measurement in electron beams and in the buildup region for photon beams.

A research group, in collaboration with a manufacturer of radiation detectors for radiotherapy, built and tested an unshielded diode detector [27]. Electron beam depth doses were measured with shielded and unshielded diodes, and a Roos type ionisation chamber. Their primary aim was to build an improved detector for photon beam IMRT, but the point that the internal structure and composition of a diode detector can have significant effects on the absorbed dose readings obtained is important in this project too.

The dose rate dependence of diode detector response has been reported in a pair of papers [25, 26]. Variation in the sensitivity of diodes to pulsed and continuous radiation was investigated. A range of commercial dosimetry diodes was tested. Ordinary electronics diodes were not. The sensitivity of various diodes varied by up to $\sim 7\%$ over the range of dose rates from continuous irradiation by a Co-60 source to the instantaneous dose rate of a pulsed linac beam.

The effect of dose rate on the sensitivity of diodes was not investigated as part of this project, as all the measurements made here were relative dose measurements. The diode radiation detectors constructed as part of this project are not intended for absolute dosimetry without further development work.

3 Water Phantom and Diode Array System

Planning for radiotherapy procedures is generally done by theoretical beam modelling on computers, but most commercial planning systems have limited accuracy when used for electron beam modelling. As such, monitor unit calculations for irregularly shaped electron cutouts (Section 4.2.3) are often checked by experimental measurement. Further dosimetric challenges arise if the surface contour is highly irregular, or if compensating bolus is required.

This Section covers the development of the water phantom dosimetry system, the design and construction of the various components made for this project, and the tests done to characterise the system's performance. The original idea of using a water tank based experimental system to help with the design of electron bolus was Graham Sorell's. The water tank system and associated equipment evolved over a series of experiments. Fig 8 shows an early test configuration of the water tank dosimetry system.

Figure 8: An early configuration of the water tank system, showing a mask in position for scanning and a single Scanditronix diode detector beneath.

The procedure for using the water tank phantom dosimetry is as follows: A mask is placed in the water tank, filled with water and raised above the bulk water surface to form the shaped water phantom. A radiation detector (or detectors) is positioned just under the mask. During irradiation, the detector is lowered to obtain the relative depth dose curve under that particular point. More depth dose scans are performed at different points until the desired volume has been scanned at the desired resolution.

3.1 Masks

Patients undergoing radiation therapy to their head or neck are typically fitted with an immobilisation mask to assist them in remaining stationary during irradiation. Immobilisation is used very frequently with head and neck treatment because the small size of anatomical features in the head and neck, and the close proximity of tumours and treatment volumes to critical structures. Any movement during irradiation could cause serious side effects. These masks are custom made for each patient.

3.1.1 Laser Scanner vs Plaster Casting

At the time of this project, there were two methods available at Christchurch Hospital for manufacturing masks, plaster casting and laser scanning.

Plaster casting is the older, more established method. A plaster negative is made directly from the patient's face and head. A plaster positive bust is cast from the negative. A vacuum former is used to shape a plastic mask from the positive bust (see Fig 10). The plastic cannot be molded directly on the patient because it is rigid at body temperature, and only becomes flexible and ductile at much higher temperatures.

The laser scanning mask manufacturing method uses an ARANZ hand held laser scanner (Fig 9) to capture a three dimensional representation of the patient's face and head on a computer. A computer controlled milling machine is then used to mill a plaster bust from the patient data. The plaster bust is then used to form the plastic mask as in the previous method.

3.1.2 Mask Mounts

The masks which form the custom shaped water phantom must be supported at the correct height in the water tank. Two perspex panels were cut to hang

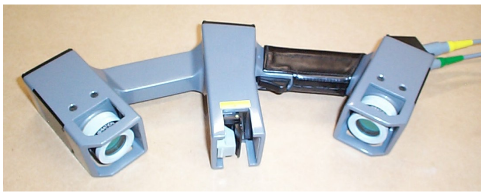

Figure 9: The handheld ARANZ laser scanner has a fan-beam laser emitter in the middle, and two cameras, one at each end. A Polhemus magnetic positioning system is used to determine the location and orientation of the scanner.

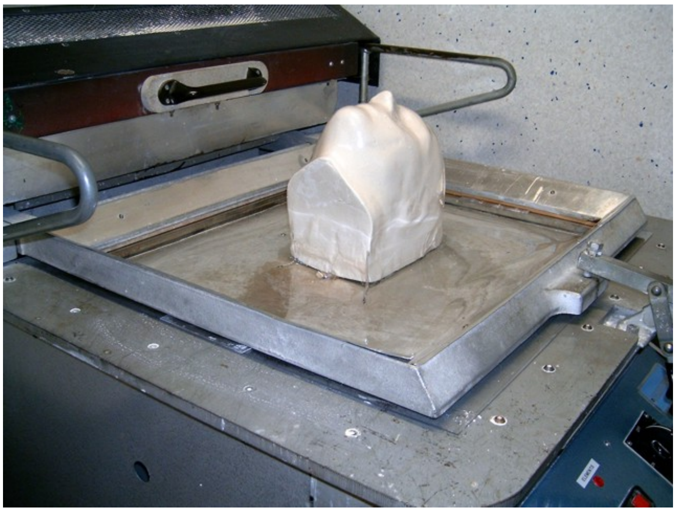

Figure 10: A sheet of plastic (not easily visible here because it is transparent) is heated until it becomes flexible. The plaster bust is then raised through the plane of the plastic sheet while a vacuum pump evacuates the space in between. When it has cooled, the plastic mask is removed and trimmed.

from the edges of the water tank and support a mask between them.

In the first setup, the mask was attached by G-clamps to the two hanging panels. Perspex inserts gave additional rigidity to the end faces of the mask. This setup is shown in Fig 8. This early mask was prone to distortion from the weight of the water inside the mask. Detector positions programmed with the water tank empty were out of position when the mask was filled with water. The mask could slip between the G-clamps or rotate around the axis formed by the clamp points. One axis of the mask position in the tank depended on the rigidity of the mask, which was limited. As well as making experiments more difficult, distortion of the mask meant the water phantom was not accurately reproducing the shape of the patient. A better mask mount was needed.

A full frame was designed and built to support the mask in the correct shape in all three axes. When a mask is molded in the vacuum former, it is surrounded by flat, undistorted plastic sheet. A strip of this flat plastic was left intact around the periphery of the mask. Two perspex rectangular frames were made. These are placed above and below the peripheral strip round the mask like a sandwich, and held together by four nylon screws. The frame is screwed to the two hanging panels.

3.2 Single Detector Mounts

If a single radiation detector is used, the RFA detector positioning system must be programmed to make multiple depth dose scans, and the starting positioning under the mask must be found for each scan. For example, scanning a 5 × 5cm field at 1cm resolution will require 25 depth dose scans. To reduce the time required with a linac and treatment room, it was preferred to program the detector movements before an experiment.

It is important that the detector start each scan as close as possible to the inside surface of the mask, however if the detector hits the mask, then the position will be inaccurate and probably not reproducible. If the detector hits the mask on a curved surface, it is usually deflected sideways. If the detector cannot be deflected, the mask may deform, or the detector may be damaged. Several collision detection systems were tried.

Visual Checking for collisions by visual inspection was unsuccessful, because refraction effects from the plastic mask and the water produced optical distortions that were very difficult to discern from collisions and deflections. Fig 11 shows an example of this.

Spring switch The first detector mount with collision detection used a mechanical switch (see Fig 12). Deflection of the diode closes a circuit between a hollow cup and a metal post. This system was not sensitive enough. The gap between the two contacts could not be made small enough, a deflection large enough to close the circuit could already be identified visually.

Strain gauge A more successful system used strain gauges. The mount was a slightly flexible plastic tube (see Fig 13). Two strain gauges in a bridge circuit (see Fig 14) were stuck to the tube $\sim 90^\circ$ apart using glue. The strain gauges and electrical contacts were waterproofed with a silicone sealant. A digital voltmeter measured the voltage across the bridge, collisions were easily seen as changes in the voltage. This system was sufficiently sensitive, but the motorised positioning system could not reproduce preprogrammed positions accurately enough after being turned off.

Scan positions were programmed on the day before the experiment and verified on the day. The verification tests revealed errors of 0.5mm to 1.0mm in the scan positions. The cause of these could not be found. The mask and mask mount was quite rigid, and the position of the mask in the tank was reproducible to within 2mm. The origin of the detector position coordinate system was reset to compensate for any change in the mask position. The detector positions were reproducible to within $\sim$ 0.2mm on each day, but not from one day to the next, with the system shutdown over night. The tolerance specification of the water tank positioning system is 2mm, so these errors do not indicate a fault.

3.3 Diode Array Radiation Detector System

The diode array mount (see below) does not require detector positions to be preprogrammed. Using multiple detectors, fewer scans with the mount are required. The detectors can be positioned manually during the experiment in an acceptable amount of time.

Figure 11: Two views of the diode array in use with a mask water phantom. With the mask full of water, refraction and the irregular shape cause significant optical distortions, making it difficult to position the detectors visually.

Figure 12: Diode detector mount with spring switch collision detection. An RFA diode (red) is mounted. A post protrudes through the spring into a cup machined into the inside of the diode holder (which has a grey cable exiting on the left).

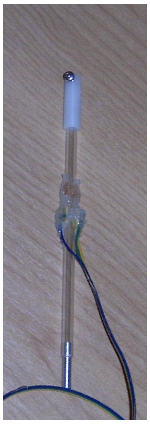

Figure 13: Diode detector mount with strain gauges for collision detection. Two strain gauges are affixed around the centre of the plastic tube. The diode screws into the white holder at the top of the mount, and the metal plug at the bottom fits the RFA detector mount.

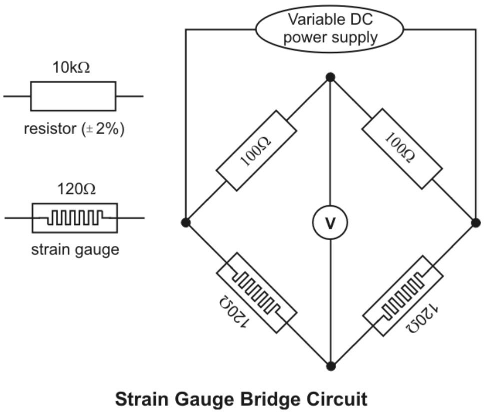

Figure 14: Circuit diagram for the strain gauge collision detection system.

The diode array mount is described in Section 3.4. This subsection describes the design, construction and testing of the diode radiation detectors used in the array. The choice of diode detectors is discussed first, followed by design and construction of a radiation detector. The detectors were tested for dependence on radiation dose rate, particle type and energy, angle of incidence, and for effects of radiation hardening.

3.3.1 Detector Selection

MOSFET - Thomson-Nielsen system

A Thomson—Nielsen MOSFET radiation detector system has been considered for use in the water tank experiments [22].

MOSFET stands for Metal Oxide Semiconductor Field Effect Transistor (see Fig 15). In a field effect transistor the current between two electrodes, the Source and the Drain, is controlled by the voltage on a third electrode called the Gate. When the gate is charged, its electric field attracts charge carriers to a region called the channel, allowing conduction between the source and drain. Metal Oxide Semiconductor refers to the construction of the transistor. The metal gate electrode is separated from the semiconductor channel (typically silicon) by a layer of insulating silicon dioxide.

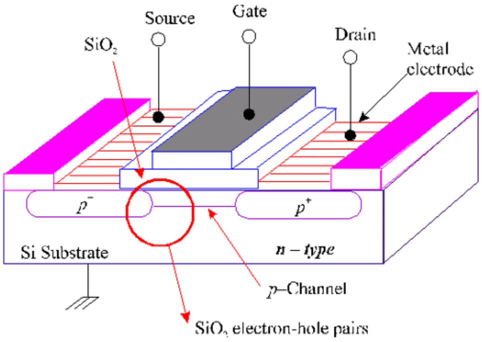

Figure 15: A MOSFET radiation detector. When a voltage is applied to the Gate, the electric field from the Gate forms a conducting channel between the Source and the Drain. Irradiation forms electron-hole pairs in the insulator between the Gate and the channel, altering the relationship between Gate voltage and Source to Drain conductivity. *Reproduced from Thomson—Nielsen website [22].*

Semiconductors can be categorised as n-type, in which the charge carriers are electrons, and p-type, where the charge carriers can be considered holes or vacancies. The Thomson—Nielsen radiation detector is a p-channel MOSFET, meaning the substrate is n-type silicon, and the transistor is turned on when a negative gate voltage repels electrons to form a p-type channel from source to drain.

When a MOSFET is exposed to radiation, ionisations occur in the insulating oxide layer between the gate and the channel. If a positive voltage is on the gate electrode during irradiation, the electrons freed by ionisation will migrate to the gate, leaving the oxide enriched in holes. This effective positive charge means a greater negative voltage must be applied to the gate to turn on the transistor. This change in the characteristics of the transistor can be used to measure the dose it was exposed to.

MOSFET detectors are cumulative dosimeters that have a limited life. When the maximum useable gate voltage is reached by accumulated radiation exposure, the MOSFET has to be replaced.

Diode

Diodes are widely used as dosimeters in radiation therapy applications, although ionisation chambers are considered to be more accurate. The main advantage of a diode over an ion chambers is smaller size, giving greater spatial resolution.

A semiconductor diode is formed by producing p-type material (semiconductor doped to have an excess of holes) adjacent to n-type material (doped to have an excess of electrons). The diode behaviour arises from the properties of the junction between the materials.

Diode radiation detectors behave like photovoltaic cells. Photons with energy greater than the band gap of silicon can generate electron-hole pairs in a diode. At the diode junction, the electric field of the depletion layer separates the radiation-generated electrons and holes, producing a reverse current through the diode.

The base material for diodes is most commonly silicon. Common dopants are boron and aluminium (for n-type), and phosphorus (for p-type). Electrical contacts are typically copper. The envelope or casing of a diode is usually plastic or glass. With the possible exception of plastic casings, none of these materials is tissue or water equivalent in interactions with photon or electron radiation used for radiotherapy.

Silicon has a higher atomic number than air, water, biological tissue or graphite (which is a common material for ion chamber walls). As a consequence of the photoelectric effect, which is Z dependent, silicon diodes are more sensitive than ion chambers to low energy photons. Diamond detectors are one way to avoid this problem, replacing silicon with carbon. At the time of this work, however, diamond detectors remain uncommon and expensive.

Many types of silicon diode manufactured for dosimetry have built-in metal shielding around the semiconductor. This shielding blocks low energy scattered photons produced in the phantom material around the detector. The effects of detector shielding were discussed in Section 2.5.

It has been decided not to use the MOSFET system, first because of the limited life of the devices, and second because the Thomson—Nielsen system is designed to measure a dose and then be read out, while a continuous measurement of dose rate is more useful for the planned experiments.

Some years ago a radiation detector system based on a diode was designed and built in the Oncology Department of Chistchurch Hospital. This system can be duplicated and modified for this project. This system measures dose rate, and any components that wear out can be replaced at low cost. For these reasons, diodes were selected to be the radiation detectors in this project.

3.3.2 Detector Design and Construction

The new detector system was built using an existing design by Dave Pinchin [31]. This design is tried, proven and modifiable. A new detector was not a vital part of this project, but it was thought the results would be better. The amplifier is in principle a photovoltaic diode and a current to voltage converter (see Fig 16).

A range of diode detectors could be used with this system. A smaller diode than the one supplied with the RFA water tank was preferred, so that smaller volumes can be scanned, and the detector can get closer to the surface. Diodes left over from an old commercial diode array were available, but these are similar in size to the RFA diodes. Ordinary electronics diodes were chosen for their compact size and the ease with which they can be replaced or modified.

Dave Pinchin built a prototype amplifier to go between the chosen detector diode and the analog-to-digital converter chosen. The amplifier had to

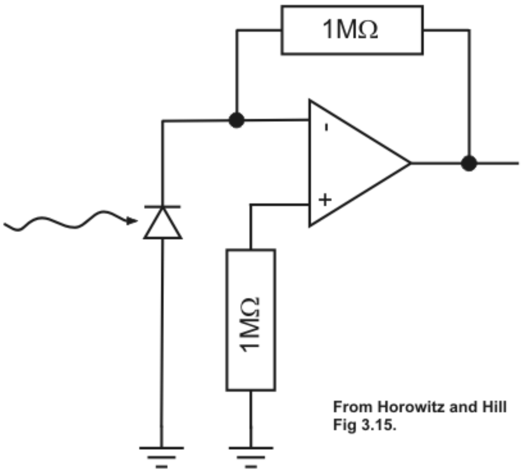

Figure 16: Basic operational amplifier circuit for use with a photovoltaic diode. *Reproduced from [24].*

be tunable to take the input characteristics of the diode, and give an output signal suitable for the ADC. Testing and refinement of the design using the prototype detector was followed by construction of more detectors to form an array.

Analog to Digital Converter

It was not intended to use fast detection or to acquire individual pulses from the accelerator. That could be useful, but would have required careful redesign of the detector and amplifier for accurate response at high frequency.

From the Picotech manufacturer there was a choice of a fast (up to 10kHz) 12bit ADC or a slow (1.5Hz) 16bit ADC. Given the speed of the existing water tank detector system, the slow ADC would have adequate speed. The input voltage range of the 16bit ADC is -2.5V to $+2.5$V; the input range of the 12bit ADC is 0V to $+2.5$V.

The linac outputs are approximately 2.5, 4.0 and 6.0 Gymin^{-1}. A 12bit ADC gives 4096 levels, giving a dose rate resolution of $\sim$ 1mGymin^{-1}, provided the analog signal spans the input voltage range of the ADC. The resolution of the 12bit ADC should be sufficient for most dosimetry applications. A 16bit ADC (65536 levels) would definitely be adequate.

The 12bit ADC was chosen for this project. This model has adequate resolution, high speed, and more analog inputs than the higher resolution model, allowing a larger array of detectors.

3.3.3 Prototype Testing

'Solid Water' was used for buildup and backscatter material when testing the prototype diode detector. 6MV x-rays were used for many test exposures. A 6MV photon beam is available on all the linacs at Christchurch Oncology, and the type of radiation should not significantly affect the diode performance. Solid Water block D/H40 has a hole designed to accommodate a Farmer type ion chamber. The diode is fed into this hole.

As an initial test, the prototype diode was connected to an oscilloscope without any amplification. A good, low noise signal was obtained. Individual radiation pulses from the accelerator could be seen. This test confirmed that the IN4004 diodes could be used as radiation detectors.

When the diode array instrument was planned, it was decided not to record the discrete radiation pulses. Instead, pulses were integrated to give the effective continuous dose rate, a similar output to that available from existing diode and ion chamber instruments in the department.

The prototype amplifier was initially configured as a single stage integrator, using a single CA3130 operational amplifier integrated circuit. The single stage amplifier provided a stable continuous dose rate signal with typical rise and fall forms at the beginning and end of an irradiation.

However, the maximum output voltage was only 150mV. A second amplifier stage, using another CA3130 chip, was added to provide additional gain. The second stage amplifier was initially set to provide a gain of 10, but this was later increased to 12 when it was found that electron beams generally gave a lower voltage than x-rays.

Fig 17 shows the output from the prototype detector in a 6MV photon beam from a Varian 600C linac. The dose rate was reduced in steps during this irradiation from 250MUmin^{-1} (2.5Gymin^{-1} at the calibrated output of 1cGy/MU) to zero. The Varian 600C emits a pulsed beam of radiation. To vary the dose rate from the linac, the pulse rate is changed. The dose rates used were: 250, 200, 150, 100 and 0 MUmin^{-1}. Individual pulses were not seen in the detector output, and no artifacts from the changes in pulse rate were seen either.

Fig 18 shows a beam profile of the 6MV photon beam. The diode detector and Solid Water phantom were set up on the treatment couch of the 600C linac. The profile was acquired by translating the couch, scanning the detector and phantom across the beam.

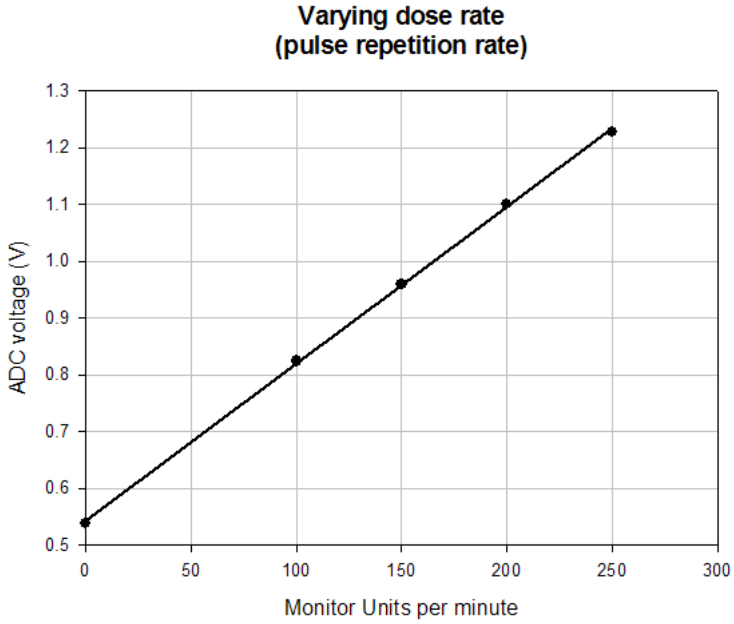

Figure 17: Effect of progressively reducing the pulse repetition rate, and hence the average dose rate, of a 6MV photon beam. The response of the detector was quite linear across this range of dose rates, a linear fit gave a R^2 value of 0.9996.

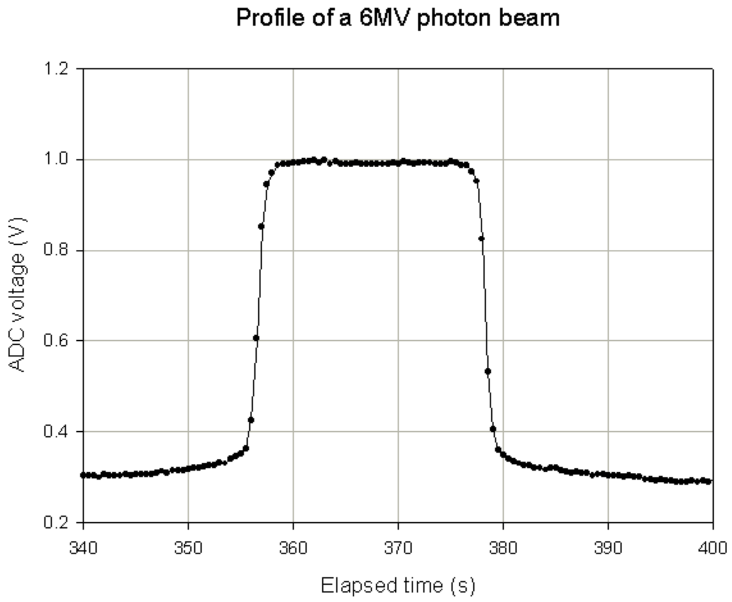

Figure 18: Profile of a 6MV photon beam obtained with the prototype diode detector.

Fig 19 was acquired by translating the treatment couch vertically during irradiation, increasing the source-to-detector distance. The resulting curve has the expected inverse square law shape.

The intention of these simple experiments was to demonstrate the prototype detector performing the kind of measurements commercial radiation detectors are used for. Precision measurement was not the objective at this stage, so neither the beam profile nor the source-to-detector distance graphs has been plotted against actual position.

With the second stage amplifier installed, low frequency noise was seen in the data. The amplitude of the noise increased when the beam was on, but the periodicity was unchanged. Fig 20 shows datapoints recorded with no radiation beam. The quantisation of the Analog to Digital Converter can be seen in the way the points take only a few discrete voltage levels. Fig 21 shows datapoints with the beam on. The periodicity is the highest frequency displayable with this sampling rate. The grouping of datapoints into high, middle and low bands suggests the data is aliasing a higher frequency variation. Measurements at a higher sample rate of 1kHz were made.

Runs were made with the same settings as previously, except the sam-

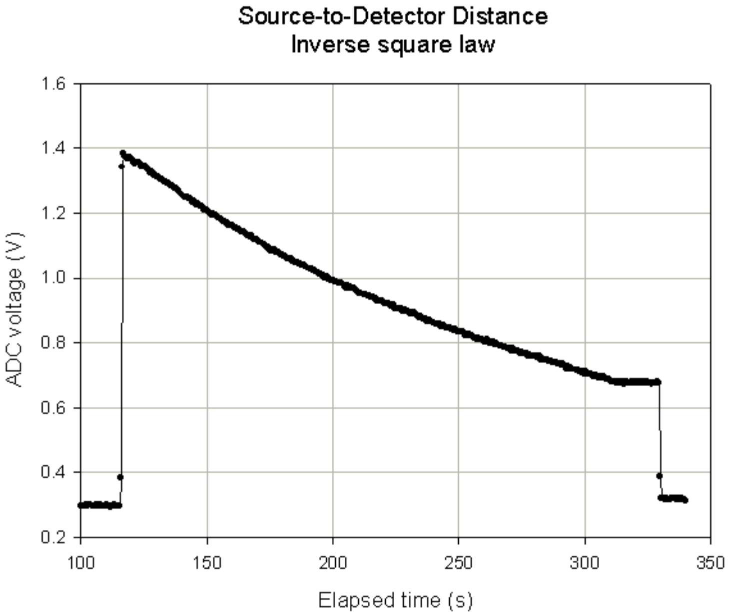

Figure 19: The inverse square law effect of increasing the source-to-detector distance during irradiation.

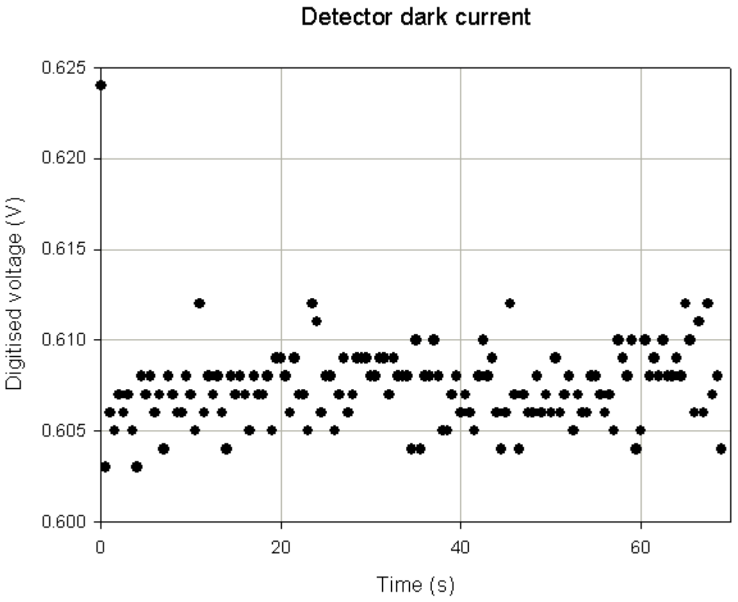

Figure 20: Prototype detector signal noise with no radiation.

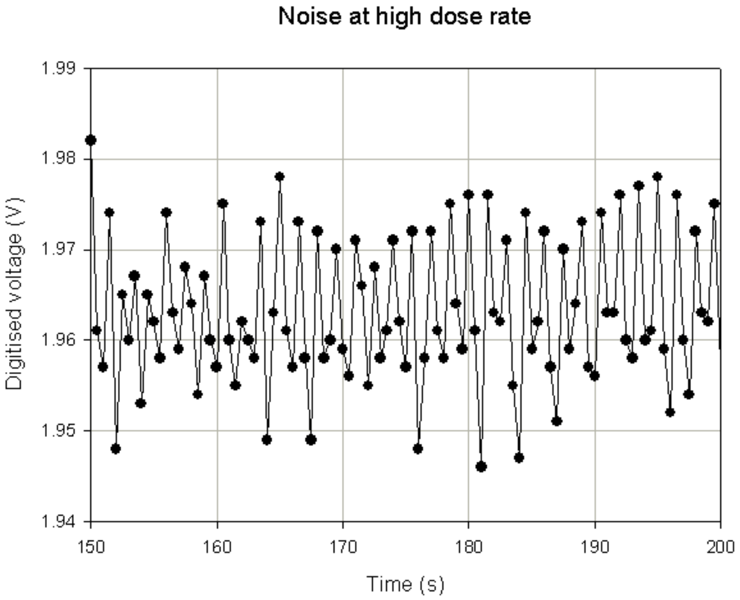

Figure 21: Signal noise during irradiation at 6Gy min^{-1} (600MU min^{-1}) with 6MV photons.

ple rate was increased to 1kHz, and other ADC sampling parameters were adjusted to allow this frequency.

ADC sampling parameters

Sample rate How often the sample scanning process is initiated.

Sample mode There are two modes, 'continuous' records as many readings as possible in available time, 'single' takes one reading.

Scan time The time allowed for readings. The readings acquired are averaged, and the average is the sample value.

A very noisy signal was obtained, both with the linac beam on and with the beam off (dark current). The noise had no obvious periodicity and an amplitude of 0.2V. The waveform resembled that obtained previously, but with greater amplitude. Averaging using the sampling parameters reduced the amplitude of the noise, but did not eliminate it.

Using an oscilloscope capable of higher frequencies than the ADC, the noise was found to be a 1.3MHz sine wave from the second stage of the amplifier. A strobe capacitor was fitted to the second stage to provide frequency compensation, and the noise disappeared. Subsequent measurements showed the dark current noise with the radiation beam off is set by the quantisation noise of the ADC (Fig 22).

Fig 23 compares the noise in a 6MeV electron measured before and after the second stage strobe capacitor was installed. The scatter of the datapoints is similar both with and without the strobe capacitor. The noise with the strobe capacitor installed appears slightly greater, but this is not thought to be significant. The source of the noise when the beam is on was never found. High frequency electromagnetic noise from the linac or instabilities in the radiation beam are suggested possibilities.

This process of discovering a fault, investigating and correcting it, illustrates how much of this project proceeded. Technical issues with the equipment required to perform experiments and simulations occupied more time than expected.

Frequency Compensation

Operational amplifiers are usually configured with negative feedback networks which trade gain for other desirable properties. In the case of this project, the negative feedback network on the first stage amplifier causes it to function as an integrator. On the second stage amplifier, negative feedback is used to set the gain of the op-amp.

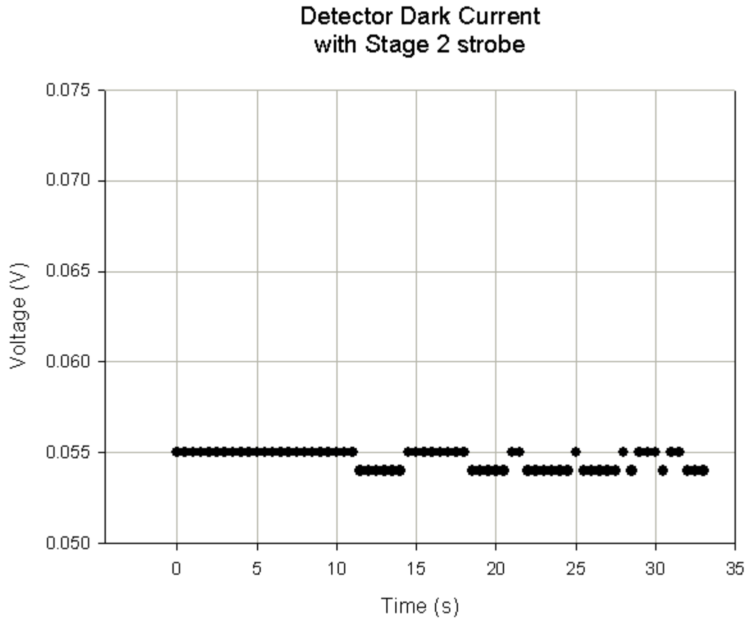

Figure 22: Signal noise with no radiation from the prototype detector with frequency compensation installed.

Op-amps (and connected negative feedback components) introduce a phase shift into AC signals which is frequency dependent. At some critical frequency, the phase of the amplifier is −180°, which changes negative feedback to positive feedback.

If the critical frequency falls within the frequency range over which the amplifier must operate, frequency compensation is used to shift the frequency response and the critical frequency.

Modern operational amplifiers have a built in frequency compensation circuit, and the user simply attaches a capacitor (in the case of the CA3130 used here) to set the desired compensation. In many cases, the preset internal compensation is sufficient, and no additional components are necessary.

3.3.4 Radiation Hardening of Diodes

With exposure to ionising radiation, diodes initially undergo radiation hardening. The irradiation causes defects in the crystal structure of the semiconductor, raising the resistivity of the material. The detector's sensitivity decreases with cumulative dose. After a certain dose the concentration of

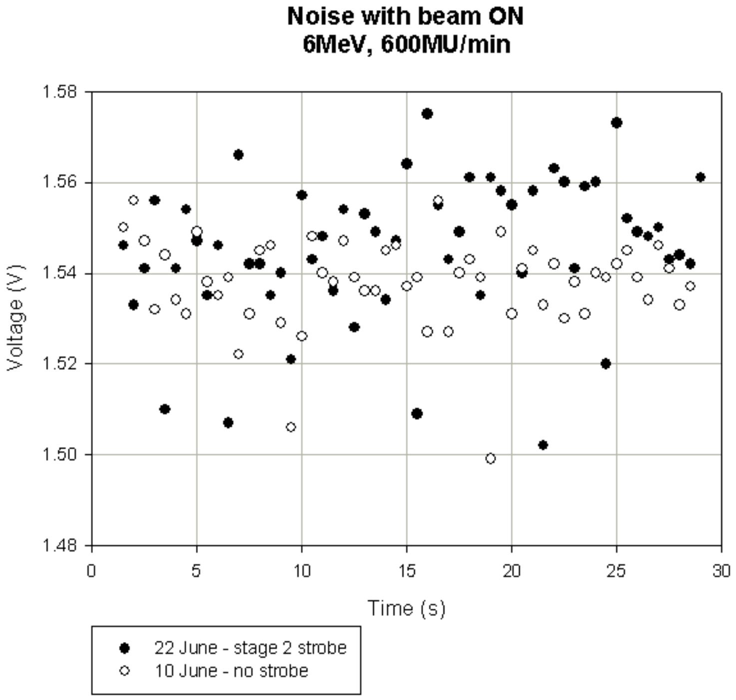

Figure 23: Signal noise during irradiation at 6Gy min^{-1} (600MU min^{-1}) with 6MeV electrons, before and after installing frequency compensation.

crystal defects reaches a maximum, with further irradiation the rate of defect repair equals the rate of defect production, and the diode is said to be hardened. The response of a hardened diode depends only on dose rate.

A search for information on diode hardening yielded only a margin note in the manual for the old diode detector system giving the hardening dose as 200Gy. The source of that figure has not been found. More recent papers on the subject of radiation hardening of semiconductors deal with complex integrated circuits in high energy proton and ion beams.

Papers on diode detectors for dosimetry in radiotherapy report manufacturers hardening their diodes with doses up to 10kGy [25].

The change in response from an unhardened diode is reported to be slow. At the doses anticipated for experiments with the water tank, the error due to hardening is expected to be less than the existing uncertainties in the dosimetric system.

It was decided not to deliberately harden the diodes. Initially it was planned to take measurements under fixed conditions before and after each experiment to provide data on the effects of hardening. This could reveal the dose required to harden diodes of this type. A deliberate hardening irradiation was planned if the errors due to gradual hardening were significant.

A long exposure of 3000 Monitor Units (30Gy with the linac calibrated to 1cGy/MU) was made. Fig 24 shows a rescaled graph of the long exposure. A linear fit to this data gave a gradient of zero, although the R^2 value and other indicators of the fit quality were very poor due to the noise in the signal. The signal noise is easily visible in this view. The prototype detector amplifier was quite noisy when this experiment was performed. The maximum spread of approximately ±0.02V in 2V indicates a maximum possible change of 2% over the course of this 30Gy exposure. The fit result suggests there was no significant change.

3.3.5 Diode Angular Dependence

Some diode detectors, particularly ordinary electronics diodes, have shown significant sensitivity to the angle of incidence in their response to irradiation. The angular dependence of the diodes used in the array was tested in the experiment described here.

The diode array was built to stand upright in the detector mount in the water tank. This orientation, with the beam incident along the longitudinal

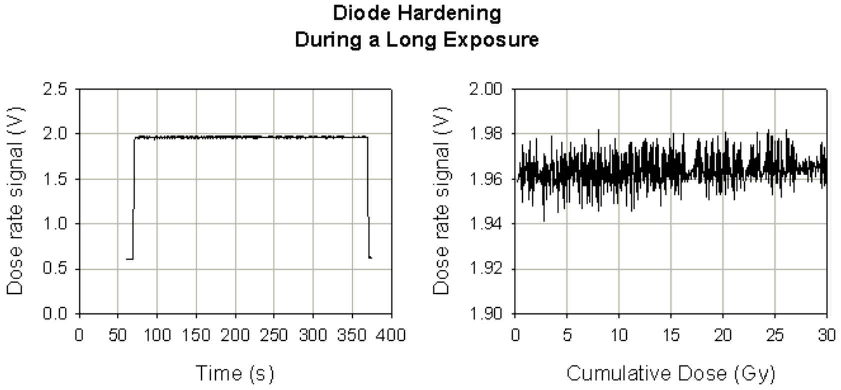

Figure 24: The prototype diode detector was irradiated with a 6MV photon beam to a dose of 3000MU (30Gy). The complete dataset is shown on the left. On the right is a magnified view. The noise most probably originates in the second stage amplifier. A linear fit to this data indicated no change in the detector output.

axis of the diodes, will be referred to as 0°. A rotation of 90° could be achieved using adhesive tape, but reliably orienting the diodes in any angle between 0° and 90° would have required construction of a new rotatable mounting. Rotating the linac gantry rather than the diode allows the gantry angle display built into the machine to be used.

Testing the angular dependence of diode response in water would have been difficult. The linac gantry cannot be turned very far without dipping the electron applicator into the water. The water surface would, of course, remain level.

Therefore, a solid phantom was constructed for the angular dependence test. The shape of the phantom is based on a sphere. With the diode junction at the centre of the sphere, the material will be the same thickness in all directions (see Fig 25, and Appendix for complete plans of the miniphantom).

The diode is symmetrical around its long axis, and symmetrical end to end about the junction (see Fig 30 and Fig 26). A single sweep from 0° to 90° should be representative of the angular dependence of the diode. Neither increasing the angle of incidence beyond 90°, nor rotating the diode about its axis was expected to reveal new variations in the signal. In all the experiments conducted here, the beam was incident from either 0° or 90°,

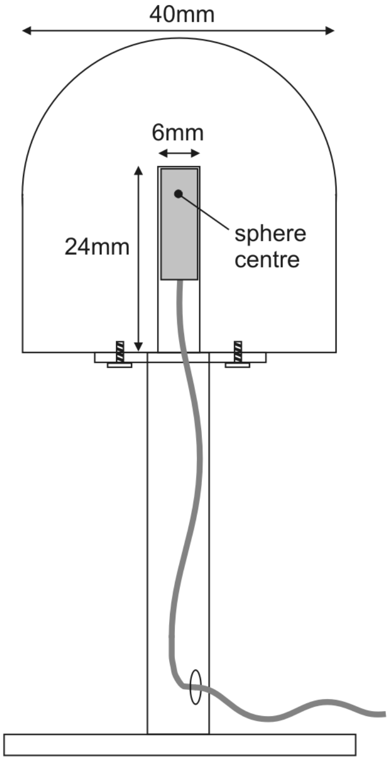

Figure 25: Plan of the miniphantom for testing diode detector angular dependence.

so the angular dependence beyond 90° is not relevant here. Accordingly, for ease of manufacturing, the shape of the phantom was modified to a hemisphere atop a cylinder.

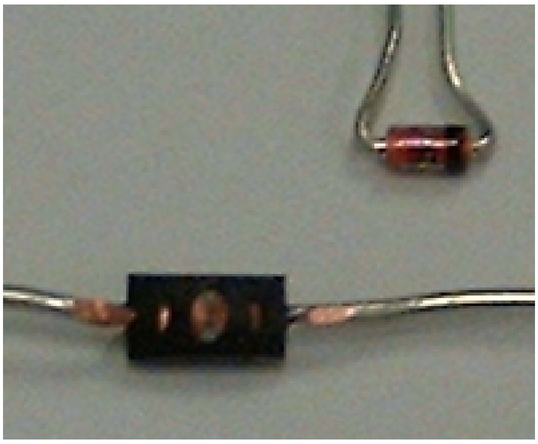

Figure 26: An IN4004 diode was filed down to expose a cross section. The diode junction material is grey. The copper contacts and wires are large compared to the junction. Most of the device is black plastic casing material. A smaller diode with a glass envelope is shown at top right for comparison.

The experimental setup is shown in Fig 27. One of the array diodes was inserted in the phantom. The phantom was mounted on a block polystyrene foam to position the diode junction at the accelerator isocentre with a minimum of solid material nearby. The phantom was positioned using the treatment room lasers (see Fig 28). The alignment of the lasers with the isocentre is checked every two weeks during normal quality assurance tests. The QA test tolerance is ±1mm.

From Fig 29 it can be seen that the diode is least sensitive to radiation incident from 0°. This direction is along the long axis of the diode, with the maximum amount of copper in the beam path (see Fig 30). The diode sensitivity is highest at an angle of incidence of 90°, where the edge of the diode semiconductor is not shielded by any copper.

Fig 31 shows the signal is well within the input voltage range for the ADC at all angles.

The angular dependence of the diode response is similar for both available photon energies. There is also less angular dependence for photon beams than electrons.

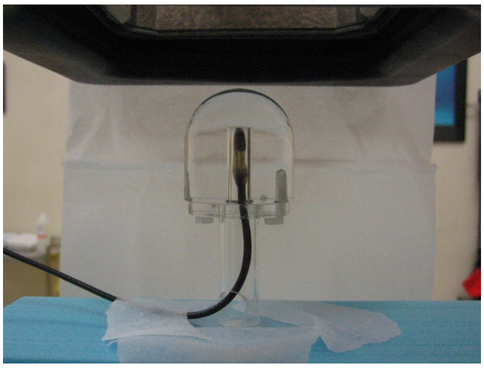

Figure 27: The miniphantom is shown here in position for the angular dependence test. The diode can be seen at the centre of the phantom. The end of the electron applicator is visible at the top of the frame.

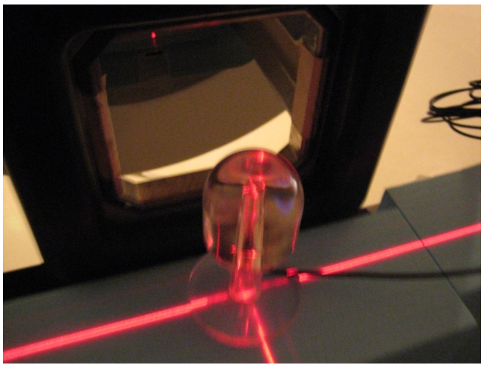

Figure 28: The laser system was used to position the miniphantom at the linac isocentre.

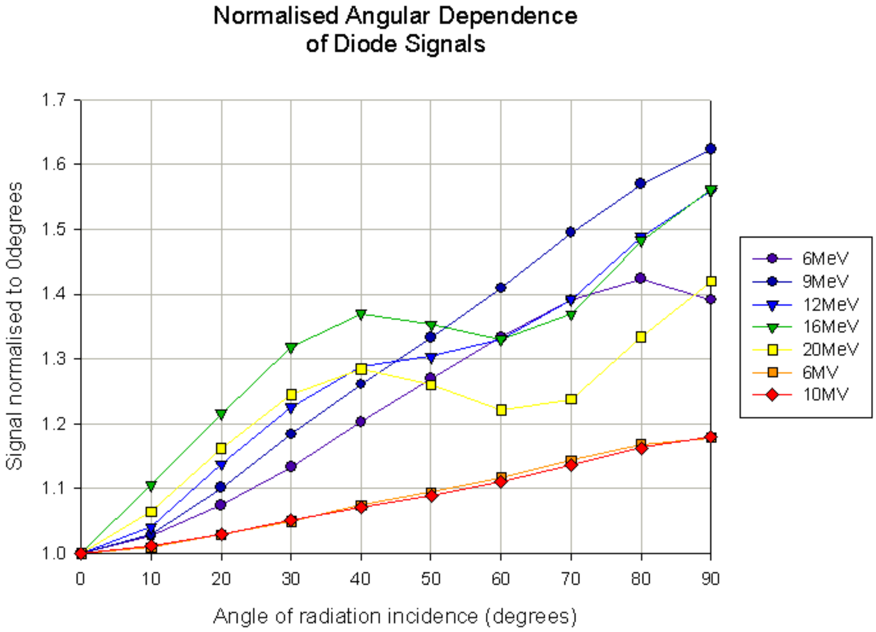

Figure 29: The normalised signals are lowest at an angle of incidence of 0°, where the diode junction is shielded by the maximum thickness of metal.

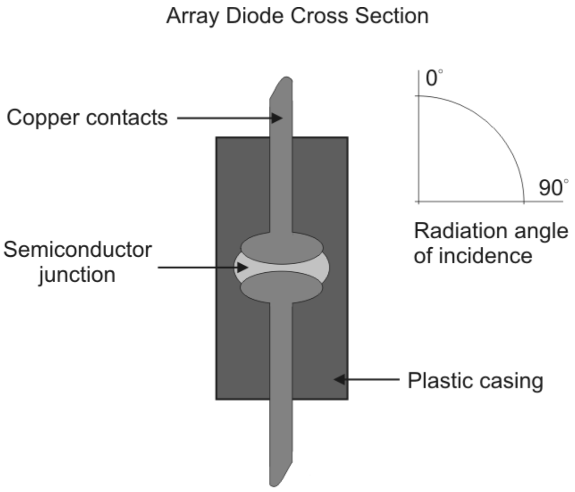

Figure 30: Internal structure of the IN4004 diodes used in the diode array.

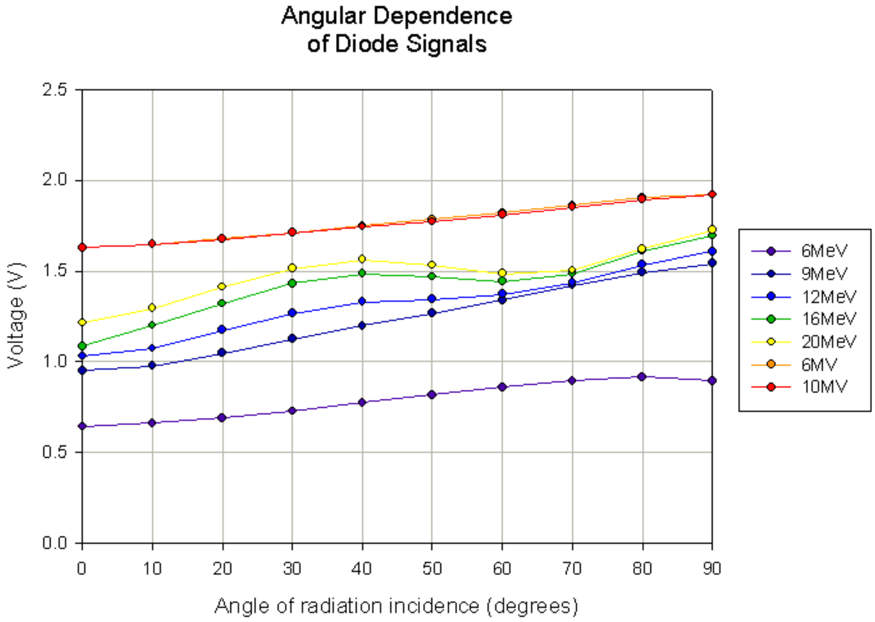

Figure 31: The angular dependence of the signal from a detector diode for a range of electron and photon beams. The buildup material around the diode was fixed at 20mm thick.

For electron beams, the variation in diode response with angle of incidence increases with beam energy. The higher energy electron beams showed a local minimum in dose rate at approximately 60°. This is attributed to production of secondary electrons changing as the amount of copper (which has a high atomic number) in the beam changes with angle. Secondary electron production becomes more significant at higher beam energies.

Conclusions should not be drawn from the relative signal strength obtained from each beam. The miniphantom provides a fixed buildup of 20mm, which does not correspond to the reference depth (where the dose rate is set) of any of the beams.

During this project, all measurements made with the diodes in water were at 0°, and all measurements made in ‘Solid Water’ plastic phantoms were at 90°. If measurements made at different angles are to be compared, the angular dependence must be compensated for.

3.4 Building and Testing the Array

3.4.1 Array Design and Construction

Early versions of the water tank system had a single detector, which scanned depth doses sequentially. The depth dose scans were arranged in a grid under the treatment field or region of interest. The diode array was designed to reduce the amount of time spent positioning the detector at scan start points. The array is a 2x5 grid of detector diodes (see Fig 32, and the Appendix for plans of the array). The gap between adjacent diodes is 2cm. This wide spacing was chosen to minimise perturbations of the radiation beam by adjacent detectors. A closer spacing on the order of 1cm is expected to be desirable for clinical work and advanced experiments. The plan is to interlace multiple scans with the array to give a minimum of approximately 20 scans with 1cm separation under a typical field.

Design issues included the thickness of the cable to the detector diodes. The cable should be coaxial for shielding of the small signal. As thin a cable as possible is desirable to reduce the mass of metal in the radiation beam. The cable passes through a plastic tube which supports the detector diode in position. The cable must be thin enough to fit through the tube; or alternatively the plastic tube must be wide enough to accommodate the cable. The tube needs to be strong enough the support the detector reliably and reproducibly, but the presence of the tube perturbs the radiation beam.

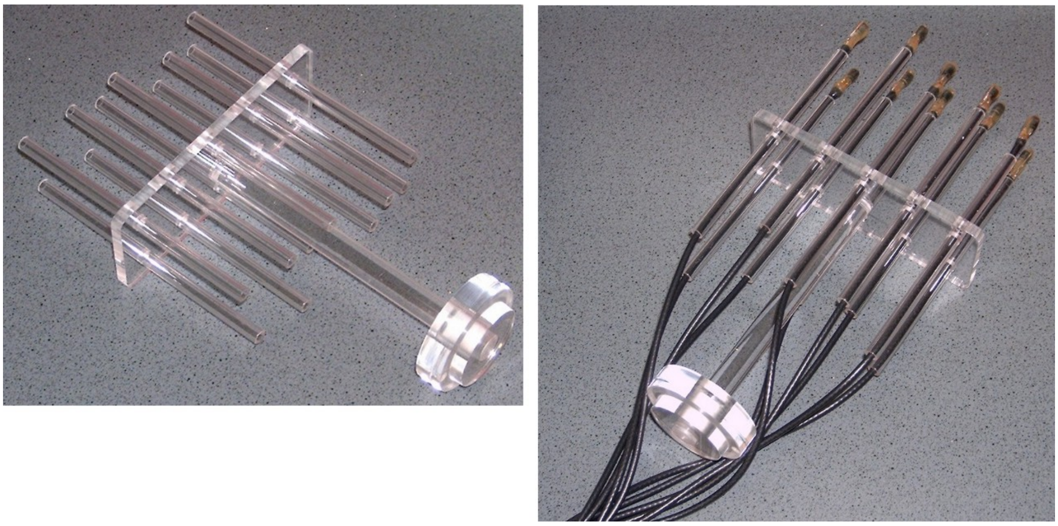

Figure 32: The diode array before (left) and after (right) installation of the detector diodes.

The diode array and amplifier box are a single inseparable unit (see Fig 33). The cable to each diode is soldered onto the amplifier board, and the diodes cannot be removed from the array. This may limit the flexibility of the instrument for purposes beyond this project. The main reason for this hardwired construction was practicality. Each waterproofed diode is too large to fit through its supporting tube, and fitting a plug and socket connection to each diode would not help, because any coaxial plug would also be too large to pass through the tube. So the diodes are trapped in the array mount. Fitting a single large plug to allow the array to be detached from the amplifier box has only slight convenience value. Putting plugs and sockets in the line between the diodes and the amplifiers also raises the possibility of connection problems and degraded signals.

The amplifier box incorporates two layers of shielding against electromagnetic noise. The box itself is metal, and inside, the amplifier board is enclosed in a smaller, metal coated box. On the amplifier circuit board, grounded shield tracks were laid either side of tracks carrying low strength signals.

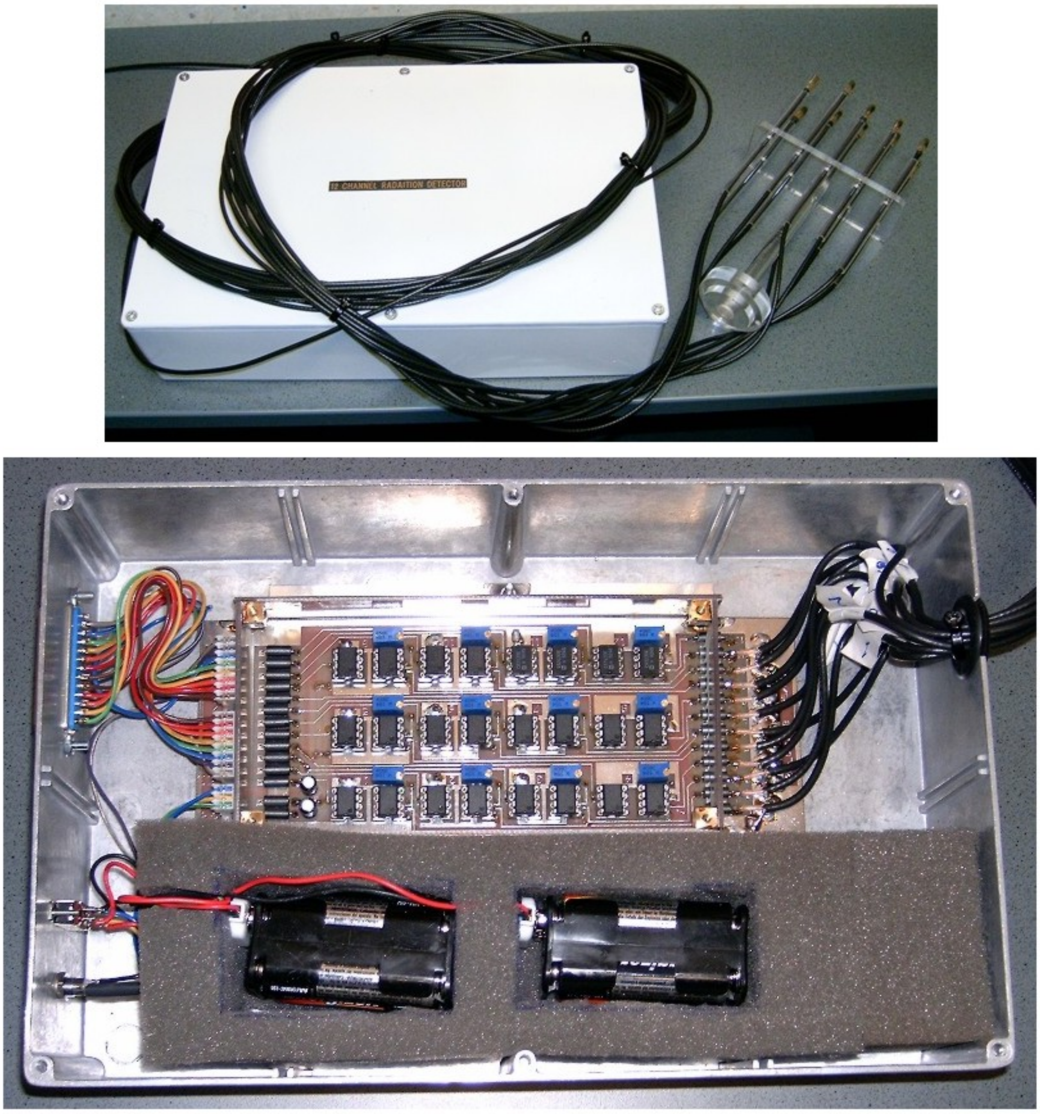

Figure 33: The box containing the diode array amplifier (top), and the amplifier inside (bottom). There are 12 amplifiers on the circuit board, 10 for the array, one for the refeence diode, and one spare. The circuit board itself is inside a second metal coated box for additional shielding against electromagnetic noise. The batteries provide 6V to the circuit board.

3.4.2 Testing the Array

The diode array detector system was initially tested by surrounding the array with Solid Water. Solid Water was placed above, below and between the two rows of detectors. The top row of diodes was at $\mathrm{d_{max}}$. The bottom row gave a smaller signal than the top row, consistent with detectors positioned below $\mathrm{d_{max}}$. Detectors on the same row had very similar signals, indicating the detectors have similar characteristics.

Comparison was then made between the array and commercial detectors used with the RFA water tank. Beam profiles and depth dose scans were made with a ‘grey’ Scanditronix diode, a RK type waterproof ion chamber, and the array. Five electron beams from 4MeV to 16MeV, and 6 MV and 18MV photon beams, were used in this experiment.

The array was operated here without a reference detector because the noise seen in the reference diode signal was much greater than the noise from the array diodes. The reference diode might give a usable reference signal with a larger buildup cap than was available for this test. The top section of the angular dependence test phantom may suffice.

Fig 34 shows the results for a 6MeV electron beam. This data was collected in a single irradiation. The centre of the array was positioned at the central axis of the radiation field. All the diodes were therefore off-axis, but prior measurement of the flatness of the beam showed a maximum output variation of ±2.8% for 18MV x-rays, a variation of ±1.3% for 4MeV electrons, and variations of ±0.7% or less for all other energies used. The diodes in the array are consistent with each other, but there are significant differences between the depth dose curves obtained with the array and the curves from the Scanditronix diode and the RK chamber. The steeper build up and drop off of the dose rate, and in particular the flat region near the surface, are attributed to shielding of the semiconductor junction of each diode by copper electrical contacts, the plastic casing of the diode, and the waterproofing glue coating the diode and wires (see Fig 26 and Fig 30). The flat region of constant dose rate is especially interesting. The depth at which the dose rate begins to increase reveals the effective, water equivalent thickness of the material covering the diode junctions. Each diode records a slightly different dose rate in the flat region, but they become more consistent through the buildup region. The difference in dose rates could be due to small differences in the amount of copper and plastic shielding each diode.

The change with depth may be due to the spectrum of the beam changing with depth (since the composition of each detector remains the same). The fluence of low energy secondary electrons and photon contamination increases through the buildup region, and the energy of the beam decreases with depth [8]. The array depth doses show more noise-like variation than the commercial detectors. This noise is thought to show fluctuations in the radiation output of the accelerator. The depth doses from the commercial detectors are ratios of a detector in water to a reference detector in air. The array was operating without a reference detector. The magnitude of the variations is consistent with output fluctuations typical of this linac.

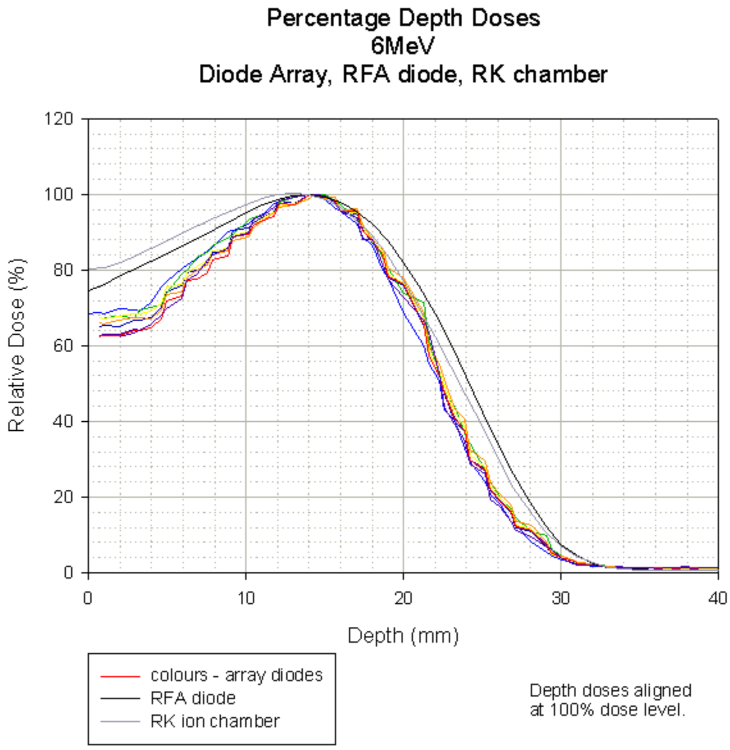

Figure 34: Relative depth dose curves of a 6MeV beam from a Scanditronix RFA diode, an RK type ion chamber, and the diode array.

Installing smaller diodes that have less material surrounding the diode junction in the array, and an improved reference detector for in-air measurements to compensate for fluctuations in linac output, may improve the performance of the diode array compared to commercial detector systems.

3.4.3 Z-positioning System

The Pico analog to digital converter system used with the diode array records voltages from its inputs, and elapsed time. It was initially planned to use this internally generated time and knowledge of how fast the RFA water tank system moves the array to determine the array position for a given measurement. All the ADC inputs were therefore used for diode detectors.

However, this method now appears unreliable and imprecise. The RFA motorised movement system is designed to move a detector in steps, pausing to take readings. As the RFA system has a readout of position in all three movement axes, no information on velocity or time is given. Smooth, continuous, slow movement is not possible. Only fast continuous movement for repositioning and slow, stepwise movement for measurement are available.

Design

A modification has been made to the water tank electronics to make a Z-axis position signal available to the ADC. The position of the detector mount in each of the three axes is determined by potentiometers geared to the detector movement motors. The output range of this system is 0V to +10V. A voltage dividing resistor network was designed and installed on the Z-axis potentiometer (Fig 35). This network provides an output from the Z-axis potentiometer compatible with the ADC input range (0V to +2.5V). An additional requirement was to keep the current drawn by this extra output low enough to avoid effecting the performance of the RFA positioning system.

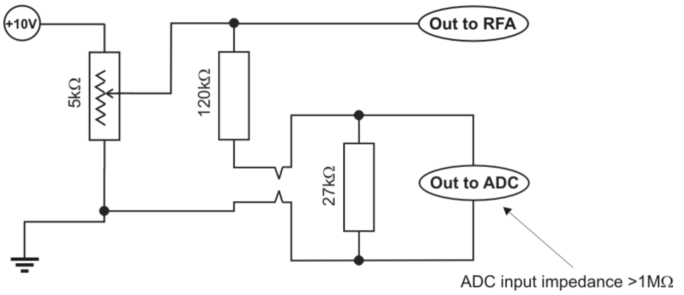

Figure 35: Z-position system circuit diagram. The ADC can be unplugged at the point denoted by the "V" shapes in the connections.

Having built the Z-position system, it needed to be wired into the amplifier box. The ADC is plugged into the box for use with the diode array, making the D25 socket on the box the only way to access the ADC inputs.

There were two faulty amplifiers in the array, numbers 3 and 10. These were disconnected from their respective ADC inputs. Diode number 3 was transferred to the spare amplifier, number 12, which was in turn connected to ADC input number 3. This should have restored detector number 3 in the array to functionality. The Z-position system was connected to ADC input 10.

Calibration and testing

The voltage output obtained with the voltage divider was calibrated using the water tank QA equipment: a ruler with an accuracy greater than the RFA positioning system with attachments to mount it in the tank. It should be noted that the RFA system measures depth downward from whatever zero point is set as the surface, while the QA ruler measures height above the floor of the water tank.

The properties of the resistor network are described by Ohm's Law (Equation 2)

$$V = IR \tag{2}$$

and the formulae for parallel (Equation 3) and series resistance (Equation 4)

$$\frac{1}{R_{total}} = \frac{1}{R_1} + \frac{1}{R_2} + \frac{1}{R_3} \cdots \tag{3}$$

$$R_{total} = R_1 + R_2 + R_3 \cdots \tag{4}$$

The ADC voltage divider resistors are in series with each other and with the portion of the potentiometer resistance between the +10V power supply and the movable tap. The voltage divider is in parallel with the portion of the potentiometer resistance between the tap and ground (see Fig 35). With the ADC voltage divider connected, the total resistance of the position measuring system changes with the potentiometer position. The total current through the system changes as the total resistance changes (assuming the power supply voltage is constant). The RFA voltage is changed by the resistance between the potentiometer tap and ground, and the change in current. The ADC voltage is a constant proportion of the RFA voltage. The Z-position data from the Pico ADC will be free of error if the curve fit converting the potentiometer voltage to position is good. The RFA system conversion formula is incorrect for the new resistance network, and unless corrected there will be errors in positions set using the RFA controller. The function for the output voltage, accounting for the changing resistance and current, was plotted, and gave a linear graph.

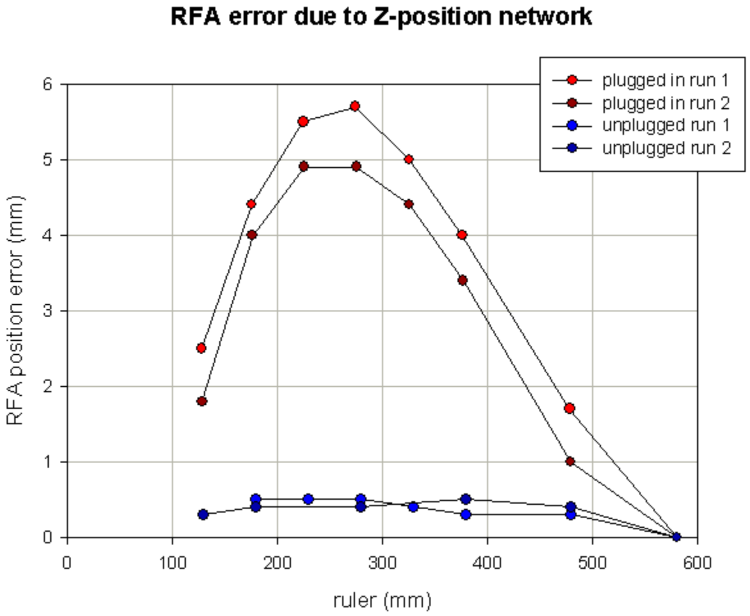

Figure 36: The error in the Z-positions reported by the RFA system, according to the QA ruler. The errors are attributed to the resistor network connecting the ADC to the Z-potentiometer.

Fig 36 shows the positioning errors made by the RFA system when the ADC voltage divider is connected to the system. Since only the RFA position shows any significant non-linearity, the existing linear fit will be used to obtain the Z-position from the ADC data. Fig 37 shows approximately linear relationships between the RFA motor system, the position according to the QA ruler and the ADC voltage. On this scale, the errors in Fig 36 are not apparent in the RFA data. A linear fit relating the ADC voltage to the QA ruler was made:

$$Z_{ruler} = a \times V_{ADC} + c \tag{5}$$

where Z_{ruler} is the height above the tank floor in mm, V_{ADC} is the ADC voltage, the value of a was found to be -3.05636 and c was found to be 1800.11. The software used, Sigmaplot 8.0, reported an R value of 0.9999 for the fit. This fit was used in the processing of data from the diode array, described below.

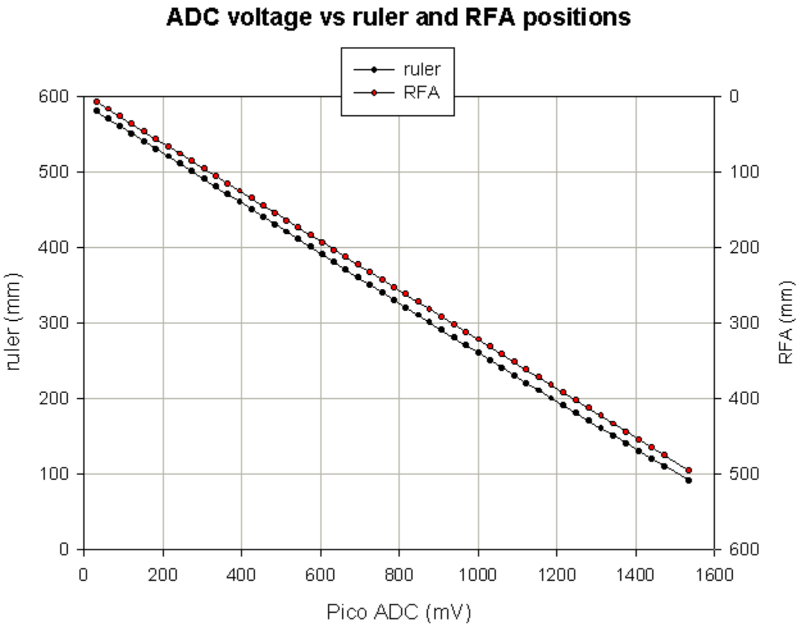

Figure 37: A good linear fit was made to this data to convert the potentiometer voltage recorded by the ADC to give the Z-position of the diode array.

The best solution to the problems with the Z-positioning system would be to replace the resistor network with an operational amplifier based device. An amplifier based system would have a much higher input impedance than the resistor network.

3.5 Data Processing and Analysis

The water tank system generates a lot of data. On the order of 25 depth dose scans are needed to cover a typical head-and-neck treatment area (5cm × 5cm field with scans 1cm apart). Larger fields will generate more data, unless the spacing of the scans is increased.

The work required to merge the diode array dose data and the patient geometry data, and to transform the data from multiple depth doses into an isodose map (the representation of anatomical and dose distribution data most commonly used in treatment planning) is also considerable.

It was therefore decided to automate some at least some of the data processing for this project. For future clinical use, full automation of data processing will be needed to reduce the workload and time required, and so that the system can be easily used by a wider range of personnel, who are not trained in mathematics and physics.

3.5.1 Software

C++: The C++ programming language was the first choice for automated data processing, as it the language GEANT4 uses. However, GEANT4 was replaced with EGS/BEAM for the Monte Carlo work, and C++ is a complicated language to learn.

Excel macros: Macros in Microsoft Excel were considered next. There are several stages in the current data analysis process which use spreadsheets and formulae.

Matlab: Matlab was the final choice for the processing stages that required programming work. Matlab has the flexibility of a programming language, but is relatively simple to use, and is intended for mathematical and scientific work.

3.5.2 Procedure

Data was recorded by the ADC in the form of a table with columns for elapsed time and each of the 11 channels. Here, one channel recorded the output of the reference detector, one channel the Z-position system output, and the remaining channels were used for diodes in the array. This data was processed using Microsoft Excel, Matlab and Sigmaplot to give isodose maps. The procedure is described below.

- Datapoints recorded before or after a scan, with the array stationary, were cropped and discarded.
- The dark current for each diode was established from a few datapoints from each channel, recorded with the radiation beam off. In Excel, the dark current for each diode was subtracted from the appropriate channel.
- All datapoints from a scan were normalised to the scan maximum dose.
- The sampling frequency of the ADC was higher than the movement rate of the detector mount. A formula to identify multiple datapoints recorded at the same depth was run in Excel. A new table was made, in which the last of a set of multiple entries was replaced with their mean, and the other rows were marked. The ‘array_collapse’ function was written in Matlab to delete the marked rows from the table.
- The Z-position system recorded the position of the entire array mount. The diode detectors in the array were set to different heights to match the shape of the mask. These height offsets were manually measured and recorded. The ‘offset’ function was written in Matlab which made individual spreadsheets for each data channel, and adjusted the Z-position data to include the appropriate offset.
- Extra datapoints recorded while the array was being moved into position for a scan were discarded. Datapoints recording a relative dose of less than 5% were discarded.
- To obtain isodose contours from the depth dose data, the INTERP1 interpolation function in Matlab was used. Interpolation was used to sample the depth dose data at 1mm intervals. The function was used again to determine the depths at which specified isodose values were reached within each depth dose.

  There were some instances of multiple readings from the same depth, jumbled and out of order. As the same pattern of these duplicates appeared in every channel of a given depth dose scan, these multiple readings are attributed to jitters in the detector positioning system. The detector mount would jump a couple of times between adjacent steps (approximately 0.3mm), before resuming normal motion. These multiple entries must be removed, as the interpolation works by fitting a function to the data, so it does not handle multiple values of the dependent variable assigned to a single value of the independent variable.

- At this stage, the data consisted of a table for each scan with a column for each isodose level and a row for each diode channel. Each diode had a corresponding position in the horizontal plane, so the data can be rearranged into a table of x, y and z values for each isodose.

This procedure was used to produce the isodose plots in Section 5 from experimental data.

4 Monte Carlo

Based on fundamental physics and statistics, the Monte Carlo technique is accepted as the most accurate method for modelling systems such as radiation therapy treatment. Monte Carlo was used in this project to verify the experimental results obtained with the water tank system. The simulation technique used here is similar to that described in papers reviewed in Section 2.3.

EGS/BEAM was chosen as the Monte Carlo software for use in this project, so a detailed description of the installation and operation of the EGS/BEAM software is given. GEANT4 software was also considered. Work on modelling the linear accelerators at Christchurch Hospital in EGS/BEAM is reported, including verification of models with measured linac commissioning data.

4.1 GEANT4

GEANT4 is a relatively new Monte Carlo toolkit [20]. It was developed at CERN for use with the LHC (Large Hadron Collider), primarily for modelling particle detectors. The GEANT4 code was written in object-oriented C++, a more modern language than the Fortran used for much of EGS and GEANT3. GEANT4 was originally intended for high energy particle physics work, but the modular design allows any part of the code to be modified or replaced, so GEANT4 has been tried in medical radiation therapy research.

As mentioned in Section 2.3, electron modelling in GEANT4 was found by Poon and Verhaegen [21] to be insufficently accurate for radiation therapy applications involving electron transport. Because of this, and Deloar Hossain's in depth knowledge of EGS/BEAM, it was decided to use EGS/BEAM for the Monte Carlo modelling aspect of this project.

4.2 EGS/BEAM

4.2.1 Installation

EGS/BEAM is a large and complex collection of software written in a combination of Fortran77, Mortran, C and C++. It is distributed as source code, not executable binary files, and must be compiled on each machine it is to be run on. For researchers who do not have experience in Unix system administration for programming and scientific applications, the workload and learning curve for EGS/BEAM installation and maintenance is considerable.

The current versions of EGS and BEAM are called EGSnrcMP and BEAMnrcMP, where MP stands for multi-platform. These versions are available for the Windows OS and Mac OS/X as well as Linux. However, the Windows installation, like the Linux installation, is source code that requires compilation.

In addition to the core simulation programs, a number of programs for building phantoms and displaying and analysing results are available. The programs used in this project are discussed below. Some of these programs require additional software packages such as Tcl/Tk, Qt, Python and xmGrace. Some of these programs (or their prerequisites) are only available for the Linux operating system.

Several Linux distributions were tried during this project. The Gentoo distribution is designed for customisation and optimisation, but consequently requires more time and expertise to administer. Redhat-based distributions are numerous and popular. The Fedora Core series and rebuilds of the Redhat Enterpruse Linux (RHEL) series are available for free. Fedora Core 4 performed well during this project. CentOS 4, a rebuild of RHEL 4, which in turn is the Enterprise version of Fedora 4, was recommended for use with EGS/BEAM by another researcher. Fedora 5 was less successful; there were problems with compilation of software, and with networking through proxies. The Debian-based Ubuntu distribution has (in this author's opinion) better package management software than the Redhat-based distributions. With the variety of programming languages, toolkits, libraries and supporting applications required for a complete EGS/BEAM system, good package management is very helpful.

As an example, the final problem encountered when installing the EGS/BEAM system was caused by the choice of Fortran compiler. Initially, the GFortran compiler was linked to the G77 name expected by the EGS and BEAM installers. This compiler successfully installed EGS and BEAM, but could not compile BEAM simulations. After changing the G77 link to point to G77-3.4 (an older GNU Fortran compiler), and reinstalling EGS/BEAM, simulations ran successfully.

At the time this thesis was written, the current versions of EGS and BEAM had an incompatibility issue. A solution was provided on the distribution website, two replacement files to be downloaded and saved over the incompatible files in an EGS/BEAM install.

4.2.2 BEAMnrc

A complete EGS/BEAM run, from specifying a linac to obtaining percentage depth doses and beam profiles, had three stages:

1. Simulating the linac.
2. Simulating dose delivery to a phantom.
3. Analysis of the dose distribution.

BEAM is the User Code for building linac simulations. With BEAM, a user does not need to specify the geometry of a linac from scratch; a variety of Component Modules are provided with predefined, but customisable, geometry for common linac components. For example, to build an electron applicator using one of the modules, only the number of scrapers, their vertical separation, aperture size, thickness and composition need to be specified. The detail of drawing all the rectangular shapes is done automatically. Similarly, a module for x-ray beam flattening filters is provided. The preset geometry for flattening filters is a stack of conical slabs, since a flattening filter is approximately conical in shape. The jaw module includes a tool which calculates jaw positions from the desired field size at SSD. The modules can be used for any purpose the preset geometry suits [29]. The information generally required to build a working linac head model is summarised in [36].

It is not intended to reproduce a procedure for specifying and building a linac here, the process is well documented in the BEAM manual [29]. The BEAM tools are helpful, but it is still many hours work to construct a simulated linac head.

The specifications of a linac are divided between two files: a module file, listing the prebuilt BEAM linac components to use; and an input file, specifying the values of various module parameters, the initial radiation source, and simulation parameters such as variance reduction and seeds for random number generation.

The output of a linac simulation is one or more phase space files. A phase space is a way of representing data about a large number of objects, each with several parameters. It is similar to a database in that each object is assigned a record containing the same fields in which data about the object is written. A phase space can also be thought of as a multidimensional graph, with each axis representing a parameter, and the position of the particle in that dimension is the value of the parameter for that particle.

A phase space file contains the position, direction of motion, energy and other parameters for each particle that passed through the plane specified for the phase space during the simulation. The plane of the phase space must be within an appropriately sized component module of the simulation. The phase space data can be used directly as a source of particles in subsequent simulations, or analysed to obtain fluence profiles and energy spectra.

An absorbed dose calculation requires a phantom and a radiation source. The radiation source can be a phase space file, an energy spectrum or a Multi Source Model.

Multi Source Modelling uses the Latch tool. The Latch is a set of bits in each particle history. Component modules in a BEAM simulation can be assigned one of the Latch bits, and every particle produced in that component module will have that Latch bit set to 1. Fluence and energy spectra can be generated for each linac component, allowing greater flexibility than a single spectrum representing the entire linac.

A phantom file or an input file describing the object the radiation beam will be absorbed in and deposit dose in. The phantom file stores EGS representations of complex objects such as patient anatomy converted from CT data. Input files contain parametric information such as composition and voxel size for simple specified objects like a cuboid water phantom.

A program developed by Deloar Hossain et al. replaces the dose distribution in an Xio plan with a distribution calculated by DOSXYZnrc. This program was written primarily to obtain DVHs for Monte Carlo simulations for a study of 3DCRT plans [37], but is useful here to visualise dose distributions from Monte Carlo simulations and Xio plans in the same format. The DVH capabilities of Xio will become important if the systems in this project are used clinically in future.

After a linac model has been built, it must be verified against experimental data to ensure the model is producing accurate results. Depth doses and beam profiles obtained during the commissioning and quality assurance tesing of a Varian 21IX linac were compared with simulated depth doses and profiles.

4.2.3 Linac Simulations

Simulated Varian 2100C linac heads for this project were constructed in BEAM using data on geometry and composition supplied by Varian [28]. Some parts of a decommissioned linac of a similar type were available for disassembly and measurement.

Models were made of each linac configuration used. Photon beams use a target and flattening filter, while electron beams use a scattering foil. Each energy has a different foil (except 6MeV and 9MeV electron beams, which share the same foil), or target and filter combination. There are six different sized electron applicators.

Electron scattering foils

Fig 38 shows one of the scattering foils from the decommissioned Varian 2100C linac. The foil assemblies each consist of 2 foils. The upper foil is supported by the crossbar. The lower foil is a button held between two sheets of aluminium (which also contribute to the scattering foil).

Jaws

The secondary collimators or ‘jaws’ of a linac are movable blocks of tungsten that set the size of photon beams. With an electron beam, the electron applicator and insert are the main means of beam collimation. The jaws assist with collimation, but are kept slightly wider than the intended beam size would dictate to reduce contamination of the beam with scatter from the jaws.

Electron applicators

An electron applicator is a frame that supports a set of fixed size collimators and a cutout mount between the linac and the patient, improving collimation of the electron beam. Applicators may also serve to improve the flatness of the beam profile. Varian linacs use open frame or diaphragm applicators. These produce fewer low energy scattered electrons than other applicator designs (such as fully enclosed cone shapes), reducing the skin dose. (Based on [30]).

Electron cutouts

The final scraper of an electron applicator holds an insert called an electron cutout. The electron cutout sets the shape and size of the electron field at the patient surface.

Electron cutouts are molded slabs of Cerrubend with holes through the middle. There is a standard thickness for the slab. The hole is molded to the size and shape of the area to be treated with radiation. The outer dimensions of the cutout match the smallest applicator that can encompass the hole.

Cerrubend is an alloy of Bi, Pb and Cd with a low melting point and high atomic number and density. It can be melted, poured and molded easily, and effectively attenuates high energy electron beams. (Based on [30]).

Manufacturing electron cutouts

To manufacture a cutout, the desired shape is drawn on paper and cut out. The shaped paper is affixed to a block of polystyrene foam. A hot wire cutter is used to cut the foam to match the paper. A mold is assembled with a base plate, a cutout holder, and the foam shape held down with a lead block. The mold is placed on a temperature controlled slab. The mold is filled with molten cerrubend. For pouring, the slab is heated to improve mobility of the cerrubend for good filling of the mold. The slab is then water-cooled to accelerate cooling of the cutout. Lastly, the base plate and foam shape are removed from the cutout. (Based on [30]).

The BEAM interface for specifying electron applicators offers only square and rectangular shapes. Simulating cutouts with arbitrary shapes would require modification of the applicator component module in the BEAM usercode, or a workaround using another component module. For the proof-of-concept purposes of this project, square fields were sufficient.

The following images, Figs 40, 41 and 42 show a completed model linac head, of a Varian 2100C (or similar machine) configured to produce a 6MeV electron beam with a 10x10cm square field.

Once an electron beam linac head had been built in BEAM, trial and error simulation was used to find the electron beam source that gave the final, clinical beam which best matched commissioning data.

Three different source geometries were tried, a pencil beam, a point source, and a parallel beam with a Gaussian radial distribution of intensity. The latter source geometry is the one recommended as most accurate by researchers at NRC [17] and linac manufacturers.

The global electron cutoff energy (ECUT) and photon cutoff energy (PCUT) were set to 0.5MeV and 0.1MeV respectively. When a simulated particle drops below the appropriate energy, the particle is stopped and its

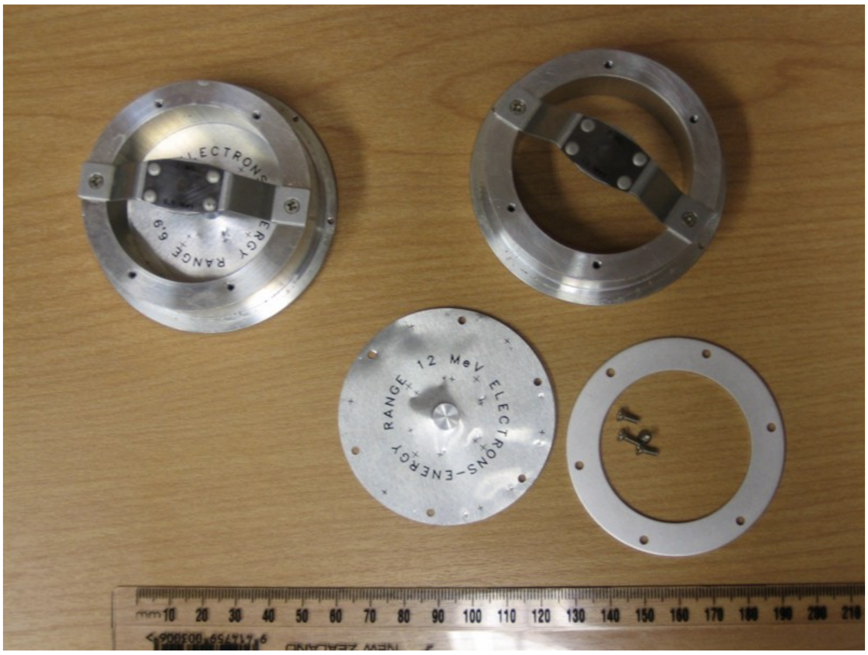

Figure 38: The three parts on the right are the disassembled components of the 12MeV scattering foil from a Varian 2100C linear accelerator. On the left is a complete foil assembly, for a different energy beam.

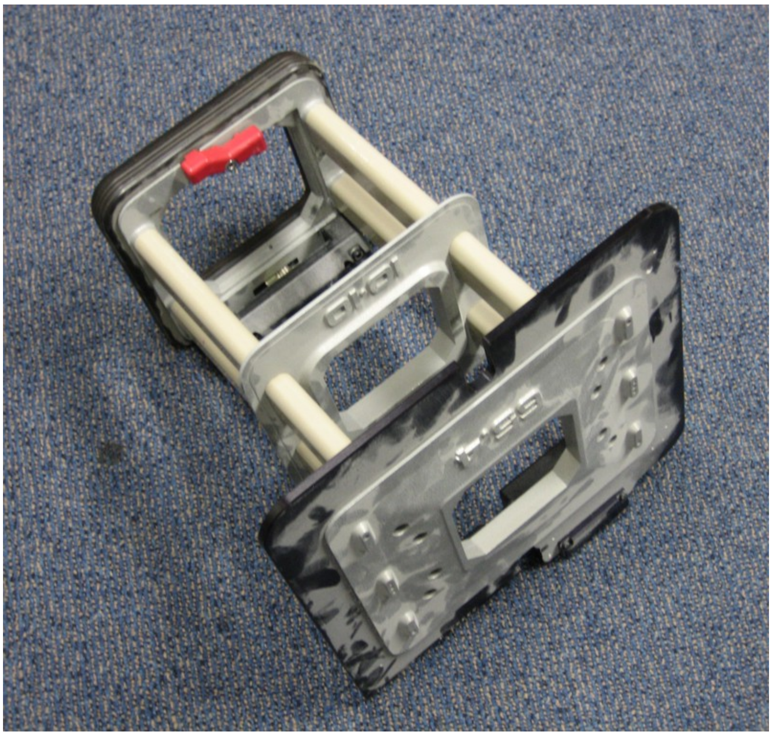

Figure 39: A disused Varian electron applicator. The top scraper is at lower right in this image, and the bottom scraper where an electron cutout or insert would be mounted is towards the upper left. The field size set by this applicator, 10x10cm, is embossed on the middle scraper. This applicator is designed to be mounted 65.4cm (embossed on the top scraper) from the reference origin of the linac head, which is taken from the top surface of the x-ray target.

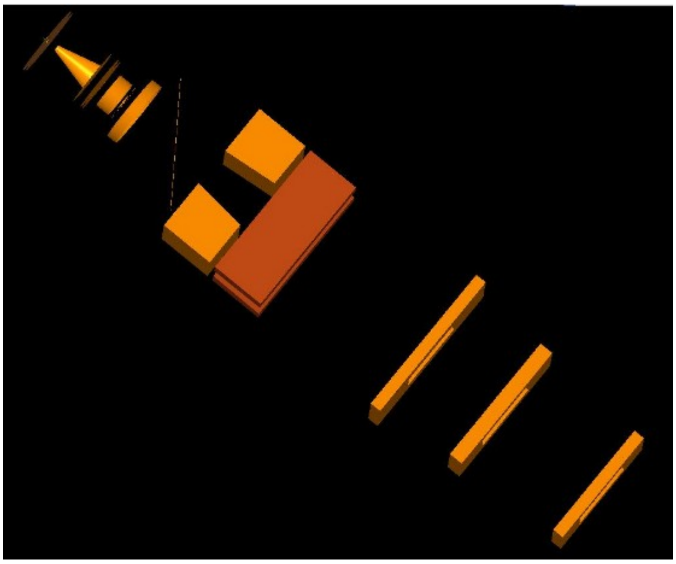

Figure 40: A EGS/BEAM model of a Varian 2100C type linac head, configured for a 6MeV electron beam. The electron beam source (corresponding to the bending magnet exit) is at the top left. The electron applicator scrapers are the three squares at the lower right. Only objects in the beam path are modelled - the frame that supports the scrapers is not shown, nor is the outer casing of the linac head, or any of the other equipment it contains.

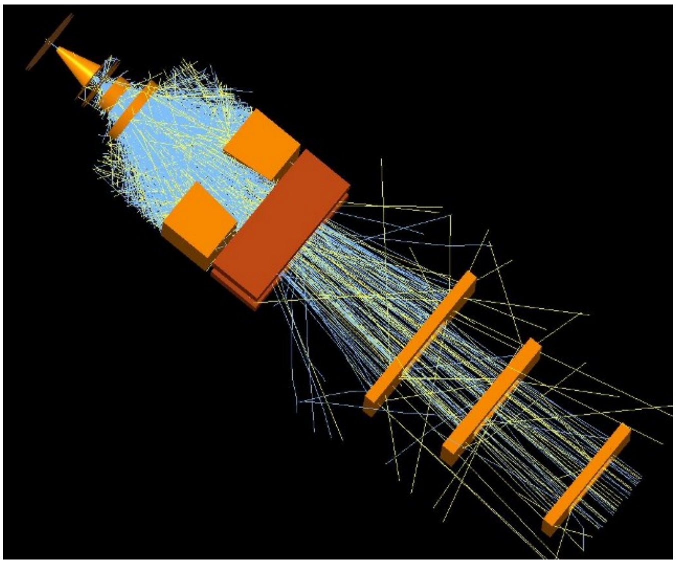

Figure 41: A EGS/BEAM model of a Varian 2100C type linac head, configured for a 6MeV electron beam, as shown in Fig 40, showing the paths of a representative sample of simulated particles. Electrons are blue, photons are yellow. It can be seen that only a small fraction of the total number of particles produced by a linac are used in the final treatment beam, and that photon contamination of clinical electron beams is significant.

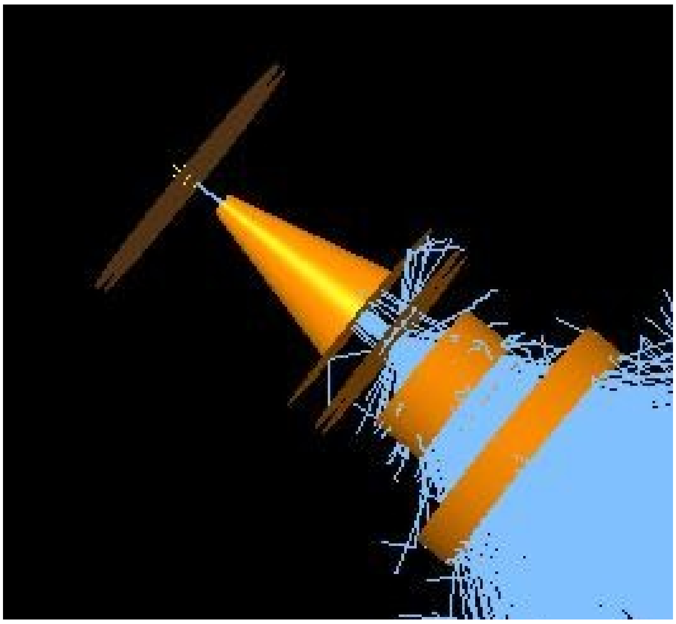

Figure 42: The upper part of a EGS/BEAM model of a Varian 2100C type linac head, configured for a 6MeV electron beam, as shown in Fig 40. The electron source, the inner wall of the primary collimator, the vacuum window, the scattering foils and the monitor ion chamber, are shown. Only electron particle tracks are shown.

remaining energy added to the dose in the current voxel. Increasing the cutoff energy reduces calculation time, as particle histories are terminated sooner, but if the range of a particle at the cutoff energy exceeds the size of the voxel then the simulation will not be accurate. Information on cutoff energies is available from help in the BEAM interface.

The electron beam of greatest interest had a nominal energy of 6MeV. This beam is the most frequently used in clinical practice. Neither the mean energy of the clinical beam leaving the linac head, nor the energy of the monoenergetic beam entering the head from the bending magnet, is exactly 6MeV.

The half-value depth in water method [4] uses formulae obtained by empirical experiments to calculate the mean beam energy from the depth in water at which the beam is attenuated to half its initial dose rate.

Several formulae are discussed in [4], each valid over a different energy range, and all of the linear form

$$E_0 = a \times HVD + c$$

where E_0 is the mean beam energy, HVD is the Half Value Depth, and a and c have experimentally determined values.

The formula used below is valid for all energies below 30MeV:

$$E_0 = 2.33 \times HVD \tag{6}$$

4.2.4 Simulations of Phantoms and Patients

The program for calculating dose distribution in a phantom is called ‘DOSXYZnrc’, where ‘XYZ’ denotes a Cartesian three dimensional coordinate system. Another version of the program uses cylindrical coordinates. As input, DOSXYZnrc requires a phase space file or other source of particles, and a phantom file or the user can manually specify phantom parameters from within the DOSXYZ interface. The output is an array of voxels and the dose deposited in each.

Setting up a simulation involves specifying a large number of variables and options. Some options and settings are well documented, with adjacent help buttons or entries in the manuals. Some options are less well documented.

In the case of the ZLAST feature (which records the Z-position of the last interaction of a particle), to run a dose distribution calculation using a phase space file as the source of radiation, the user must specify whether or not ZLAST was on during the simulation that generated the phase space file. A problem can arise because the default setting for ZLAST in BEAM is ‘on’, while in DOS it is ‘off’ by default. A user who had no interest in the ZLAST feature, and left the defaults in both programs unchanged, is given a generic message that their dose calculation run failed.

The source of three dimensional anatomical data for treatment planning systems is generally Computed Tomography (CT). To use a TPS to verify the results obtained with the diode array, CT data of the experimental water phantom was required. The Scanditronix water tank cannot be used with a CT machine (it cannot fit into the torus), so a miniature water tank was made by gluing a 1cm thick plastic panel to the bottom of one of the masks described in Section 3.1. This CT water phantom is shown in Fig 43. Initially a brass plug was used to seal the hole used to fill and drain the phantom, because a brass plug is more easily made. But that plug produced large CT artifacts (see Fig 44), and had to be replaced with a plastic plug.

A couple of minor problems were encountered with the CT water phantom. If the tank is filled with water directly from a tap, air dissolved in the water forms bubbles. If the tank is left full, changes in temperature cause leaks and presumably small deformations of the mask shape.

The CT scan data is reconstructed as axial slice images, each of which is exported as a DICOM image. There were 135 images in the complete scan of the CT water phantom. DOSXYXnrc, the EGS/BEAM code for calculating absorbed dose distribution, begins to have difficulty coping with the workload when a phantom is composed of more than about 100 slices. Slices, mainly depicting only the CT scanner table and the baseboard of the water phantom, were discarded from either end of the scan, leaving only 91 images. In addition, the resolution of each CT slice was reduced to 256×256 pixels.

There are two programs for building phantom files for DOSXYZnrc from sets of DICOM images. CTCREATE is distributed with EGS/BEAM, but was not used here. CTED was developed by Deloar *et al.* The output phantom is in a format called egs4phant. For both programs, the CT data needs to be in the form of *uncompressed* DICOM files. EGS uses the PEGS cross section data. Materials from the PEGS data are assigned to the phantom based on pixel values. The default PEGS dataset is ICRU700, which is

Figure 43: This miniature water tank was made for use with CT scanners. A plastic back panel was glued to the rectangular margin of a mask. It allows the same combination of uniquely shaped plastic mask and homogenous water fill, used in the linac experiments, to be imaged with CT.

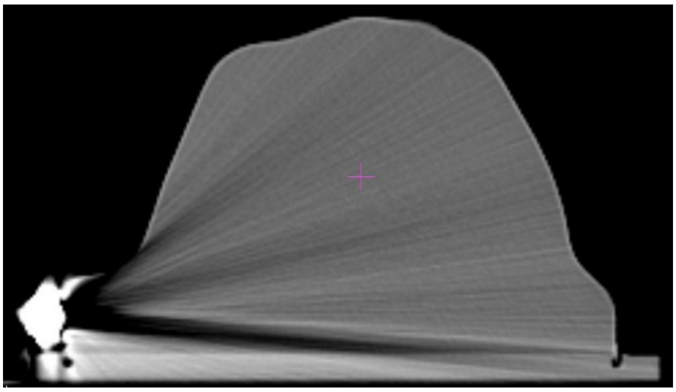

Figure 44: CT slice image of the water phantom in Fig 43. The tank was initially fitted with a brass plug (at left), which caused the ray artefacts visible in this image. The brass plug was replaced with a plastic one.

better for x-ray beam simulations. ICRU521 is preferred for electron beam simulations.

An interface program has been developed by Deloar *et al* to import a dose distribution calculated by EGS/BEAM into the Xio RTP treatment planning system (Xio version 4.2, CMS, St Louis, USA). The interface overwrites the dose distribution data in an existing Xio treatment plan with data from DOSXYZnrc. A plan must be created in Xio using the same CT data as the Monte Carlo simulation. The program 'DICOMcopy' in Xio converts DICOM images into Xio's format for CT slices. In Xio terminology, the images can then be used in Xio as cross sections forming a datapool of anatomical data. In the interface program, an offset must be entered to shift the origin of the Monte Carlo coordinate system to coincide with the origin in the Xio plan. The absolute dose values in the Monte Carlo data are usually very small ($\sim 10^{-14}$Gy), so a multiplicative factor can also be entered to normalise the dose.

In Xio, the tissue density of a pixel is determined from the pixel value and a CT number to electron density conversion file. This process is automatic, although it may be necessary for the user to specify the model of CT scanner (and hence the conversion file) if the DICOM files do not contain that information. Anatomical structures to be used in the planning process must be delineated with contours. Contours can be drawn manually, or automatically. The water phantom has no internal structure, so only one contour (the external outline) was required. This was contoured automatically using the auto-by-threshold option to draw the contour along the change in density between the phantom and the air.

Output files from the dose distribution simulator DOSXYZnrc have the suffix '.3ddose'. These results can be viewed graphically with the program DOSXYZ_show [35]. DOSXYZ_show requires both the dose distribution and a file (suffix '.egsphant') containing the phantom geometry. Generation of a .egsphant file must be selected when running DOSXYZnrc.

To extract numerical absorbed dose data from a .3ddose file for plotting depth dose curves and beam profiles, the 'statdose' program is used. Statdose is a command line interface program, run from a terminal. It calls the xmgrace software to display data as graphs. Statdose lists all .3ddose files available in the current directory, but can only enumerate 40 files, so if there are more than 40 files, some (listed alphabetically) will not be accessible.

Once a .3ddose file is selected, it must be assigned one of two numbered temporary files. This allows two .3ddose files to be compared. Once assigned to a temporary file, the data can be normalised, plotted and saved. ASCII format data can be retrieved from xmgrace plot files or saved files.

4.2.5 Verification Tests

Using the methods described above, linac models were built for 6MeV and 9MeV electron beams, both with 10x10cm applicators. The field size and beam energies were those chosen for the first tests of the diode array and water phantom experiments. Simulations were run to find the best initial energy for each electron beam. The best results are presented here, along with some less optimal results that were used in the simulations described in Section 5.

The less than optimal results were produced when the starting plane for particles in DOSXYZnrc dose calculations was mistakenly set to 1mm deep in the simulated water phantom, instead of at the surface, and the initial electron beam energies of the linac simulations were adjusted accordingly. The depth doses and beam profiles of these simulated electron beams are included here to demonstrate the effect of altering the initial electron energy, and to provide data on the Monte Carlo simulated beams used in Section 5.

The precise discrepancies between the Monte Carlo simulation results and measured beam profiles and depth doses are not analysed in depth here. A number of papers have been published which focus on the accuracy attainable with EGS/BEAM and other Monte Carlo programs, and it is not the objective of this project to repeat that work. The uncertainties in the Monte Carlo depth doses and profiles are typically approximately equal to the size of the dots marking the datapoints. Given the uncertainties in the RFA instrumentation and the Xio TPS, the errors apparent in the Monte Carlo simulations were considered acceptable for the purposes of this project.

Fig 45 shows percentage depth dose curves in water for a 6MeV electron beam from a Varian 21IX linac, and two Monte Carlo simulated beams with initial, monochromatic electron beam energies of 6.65MeV and 6.90MeV. The PDDs show the 6.90MeV simulation is clearly the better match for the measured data. The lower initial energy gives a shallower depth dose.

Initially, the 6.65MeV simulation was mistakenly run with the source of particles (the plane of the phase space), located 1mm below the surface of the water phantom. In that configuration, the 6.65MeV PDD matches the measured PDD more closely. This mistake is expected to have produced a corresponding 1mm error in the Monte Carlo results in Section 5.

The mistake also produced consistent discrepancies between the simulated and measured depth dose curves near the surface of the water, but these were initially disregarded as an artifact in the measured data caused by the diode detector.

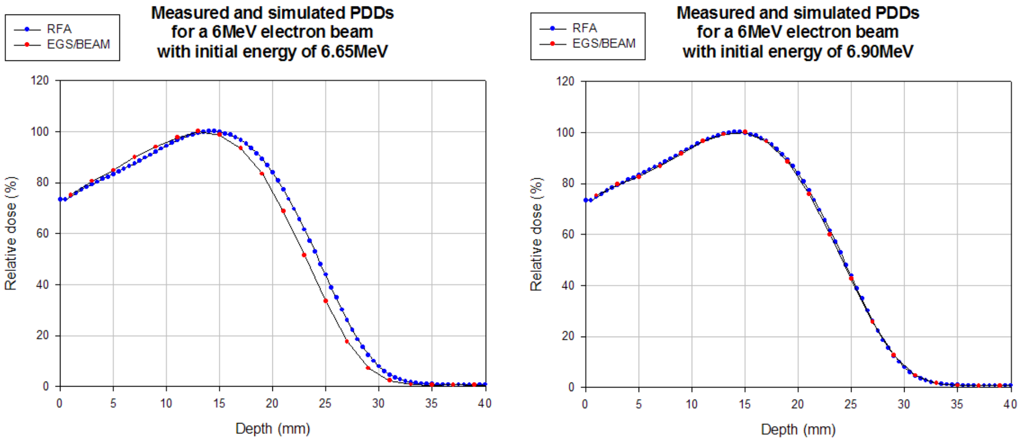

Figure 45: Comparison of the percentage depth dose of a clinical 6MeV electron beam measured in water with a Scanditronix RFA diode, and the calculated depth doses of simulations of the same beam with 6.65MeV and 6.90MeV electron sources.

Beam profiles of the same simulated and measured electron beams (Fig 46) show the 6.90MeV simulation as being the closer match for the measured data in the profile taken below d_{max}, and the 6.65MeV simulation matches similarly above d_{max}.

From Equation 6, the mean beam energy in the 6.90MeV simulation was 5.64MeV, very close to the mean energy of the measured Varian 21IX beam (5.66MeV).

The water phantom simulated by DOSXYZnrc is divided into voxels. In these simulations, the voxels were 4mm wide in each horizontal dimension, and 2mm thick in the Z-dimension. A larger number of smaller voxels would improve the spatial resolution, but the simulation would take longer to run. The depths of the beam profiles displayed here in Figs 46 and 48

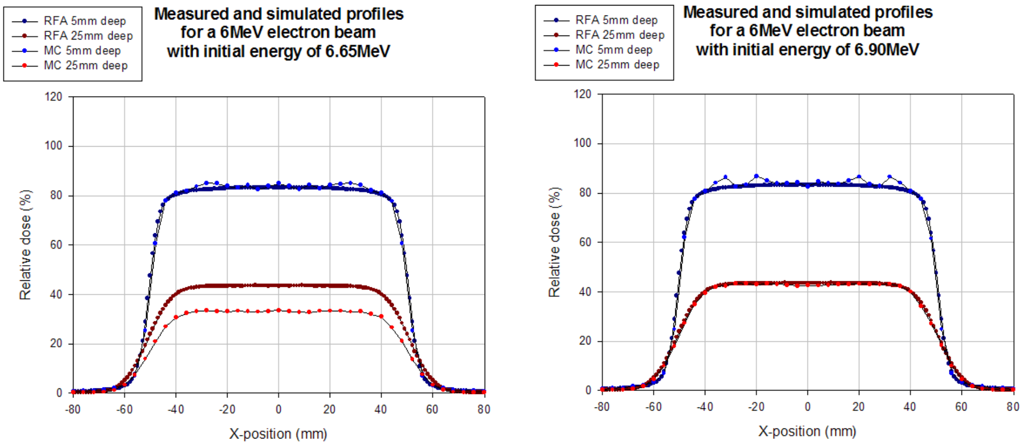

Figure 46: Comparison of beam profiles of a clinical 6MeV electron beam measured in water with a Scanditronix RFA diode, and the calculated depth doses of simulations of the same beam with 6.65MeV and 6.90MeV electron sources.

are restricted to the particular depths where the DOSXYZnrc output and the scans made with the RFA diode coincide. For 6MeV, profiles coincide at depths of 5mm and 25mm; for 9MeV the depths are 15mm and 35mm. The non-zero size of the voxels in DOSXYZnrc, and the non-zero size of the RFA diode, contribute to discrepancies between the Monte Carlo and measured results, especially where the dose changes rapidly with position, and especially in the beam profiles, where the DOSXYZnrc voxel size is large. For the purpose of determining the best initial electron beam energy, the voxel size used here is thought to be adequate.

Fig 47 shows measured and simulated percentage depth doses for a 9MeV beam in the same linac used for the 6MeV beam. Fig 48 shows beam profiles for the same 9MeV beam. The simulation with the initial, monochromatic beam energy of 9.90MeV was the best match obtained for 9MeV. From Equation 6, the mean beam energy in the 9.90MeV simulation was 8.48MeV. The mean beam energy of the measured Varian 21IX beam was 8.43MeV. The obvious effects of reducing the initial energy by just 270keV can be seen from the 9.63MeV simulation. The 9.63MeV simulation is actually a closer match above $d_{\max}$ than the 9.90MeV simulation. A small local maximum in the depth dose at approximately 5mm depth is exaggerated in the 9.90MeV simulation.

The profiles in Fig 46 also show the 6.90MeV simulation is noisy at shal-

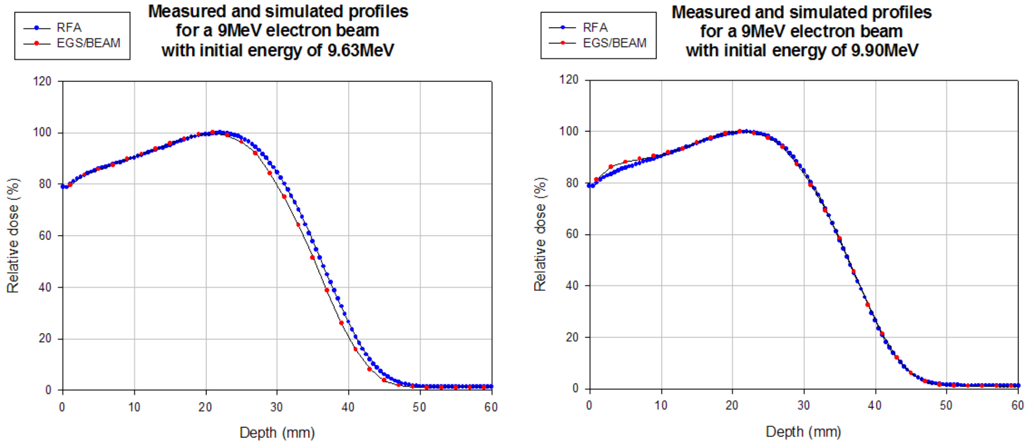

Figure 47: Comparison of the percentage depth dose of a clinical 9MeV electron beam measured in water with a Scanditronix RFA diode, and the calculated depth doses of simulations of the same beam with 9.63MeV and 9.90MeV electron sources.

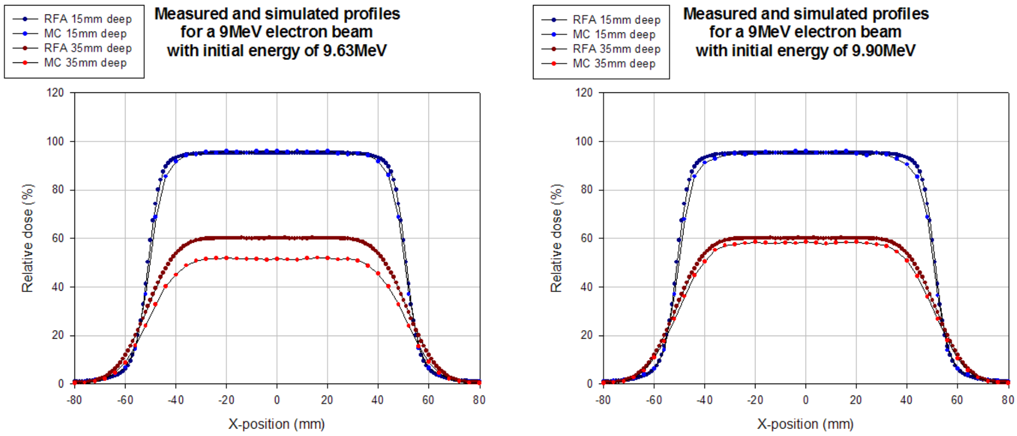

Figure 48: Comparison of profiles of a clinical 9MeV electron beam measured in water with a Scanditronix RFA diode, and the calculated depth doses of simulations of the same beam with 9.63MeV and 9.90MeV electron sources.

low depth. The source of the noise is uncertain, as the number of simulated particles was the same for both simulations.

The simplest way to reduce noise in a Monte Carlo simulation is to increase the number of simulated particles. The linac simulations in Figs 45, 46, 47 and 48 were each set for 25 million initial particles, which yielded between 1 and 5 million histories in each phase space file. These histories were redistributed and recycled [34] to obtain 100 million particles incident on the model water phantom. Reusing particles in this way increases the noise and statistical errors.

Once the best initial energy was found, the linac simulations were rerun to increase the number of initial particles to 100 million, and the number of histories in each phase space file increased accordingly. The larger phase space files were used for determining dose distributions in the mask phantom simulations.

5 System Tests and Intercomparisons

The project objective was to develop a system for accurate assessment by experimental measurement of the dose distribution delivered to an irregularly shaped object by an electron beam.

This Section presents the results of an early experiment using a mask water phantom to test a proposed custom electron bolus treatment plan, and the results of an experiment comparing the diode array and water phantom measurement system with the EGS/BEAM Monte Carlo system and CMS Xio.

The possible clinical applications of the systems developed in this project are also discussed.

5.1 Patient Selection

The three treatment types considered for investigation in this project were: custom electron bolus, deep x-ray therapy of the brain, and complex lead compensators. Only custom electron bolus experiments had been performed at the time of writing. The other treatments may be investigated in subsequent work.

It was decided to restrict experiments to head and neck treatments to use the irregular shape advantage of the mask and water tank system. Some scans were made of a flat water field for testing and calibration purposes. Manufacturing special shapes of other body parts was not attempted here.

Real patient face mask molds and laser scans were used because manufacturing a realistic artificial face would have been significantly more difficult. Use of real patient treatment planning data in future work will allow comparison between the results of experiments, professionally planned treatments and, in some cases, actual patient dose measurements.

Four patient datasets were selected for use in this project. One was a custom electron bolus treatment, another was a photon beam treatment of a region of the brain, and the other two used complicated compensator arrangements.

The process of designing, building and testing the equipment and Monte Carlo software for the project took much longer than initially anticipated. Consequently, less progress was made towards preparing the system for clinical use, and much of the patient data went unused.

Custom electron bolus design was the primary area of interest for this project. Previously, all electron bolus was designed manually from basic first principles, and there was no verification of the design. Thermoluminescent dosimeters may be used during one or more fractions of a patient's treatment to ensure the dose delivered does not exceed the limits for organs at risk.

Experiments on deep x-ray treatment were proposed mainly to test the versatility of the water tank and mask system.

Compensators are for photon beam treatments. The transmission of compensator material has been measured and entered into the TPS. The Xio photon beam modelling is thought to be quite accurate (more accurate than the electron beam model). It may still be worth performing experiments to test the modelling of complex compensator sets with irregular shapes for head and neck treatment.

5.2 Custom Electron Bolus Experiment

In a typical treatment for a facial skin lesion, a Radiation Oncologist will outline an area of skin to be treated, specify the depth to treat to and prescribe a radiation dose. By convention, the entire volume specified should receive at least 90% of the prescribed dose. The entire volume cannot usually be irradiated to 100% of the prescribed dose. Achieving the highest possible dose uniformity within the treatment volume and minimising the dose to tissue outside the treatment volume is the objective of treatment planning.

Fig 49 shows a typical scan of a patient's face made with the ARANZ laser scanner. The area for treatment here included the nose. The prescription specified treatment to a depth of 10mm. Achieving uniform irradiation of this treatment volume is a significant challenge.

Points in Fig 49 are sparsest on flat planes, such as the operator specified end of this mask at the neck. Points are densest where the shape is complex and rapidly changing, such as the nose region here. There were approximately 20000 points in the original scan - only a fraction are plotted here.

The treatment plan devised by Oncology Centre staff used a custom made electron cutout (see Section 4.2.3) to collimate a 6MeV electron beam to the treatment area, and a 10mm thick layer of wax bolus material shaped to conform to the skin surface to obtain irradiation to the desired depth.

An experiment was performed to find out if the water phantom system

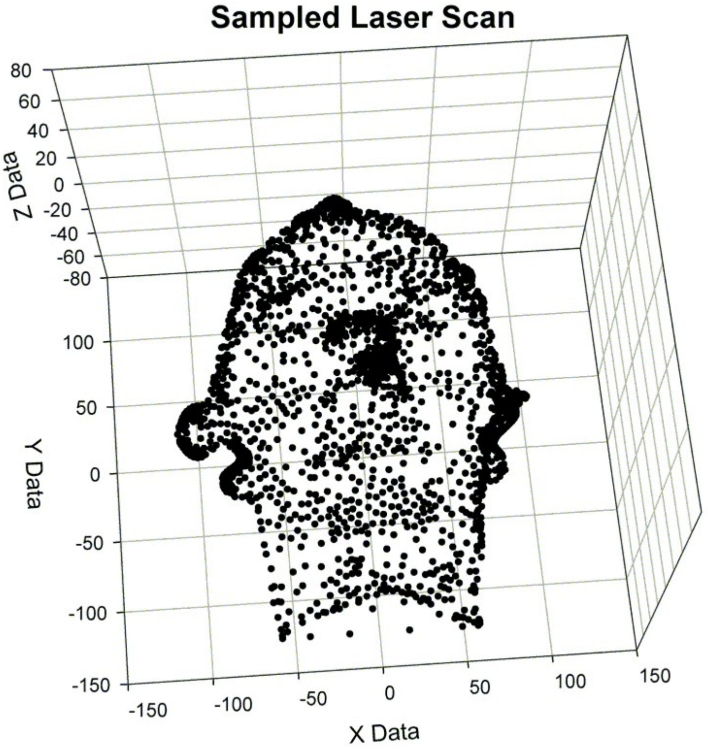

Figure 49: The ARANZ laser scanner represents a shape as a collection of points in a three dimensional space. For clarity, only a fraction of the saved points are shown in this graph.

could produce data that would assist in the treatment planning process. A mask was made using the procedure described in Section 3.1. The experiment used the first version of the mask mount (see Fig 8) and first version of the detector mount. With the single RFA diode, seven depth dose scans were made under the mask with the 10mm thick wax bolus in place on the mask. Fig 50 shows the relative depth dose curves obtained in four of these scans. According to these results, the dose dropped below the preferred minimum level of 90% well before the prescribed depth of 10mm was reached. Fig 51 shows results of this experiment presented as an isodose plot.

From this result, the medical physicist reviewing the plan recommended that the thickness of the wax bolus be reduced to 5mm.

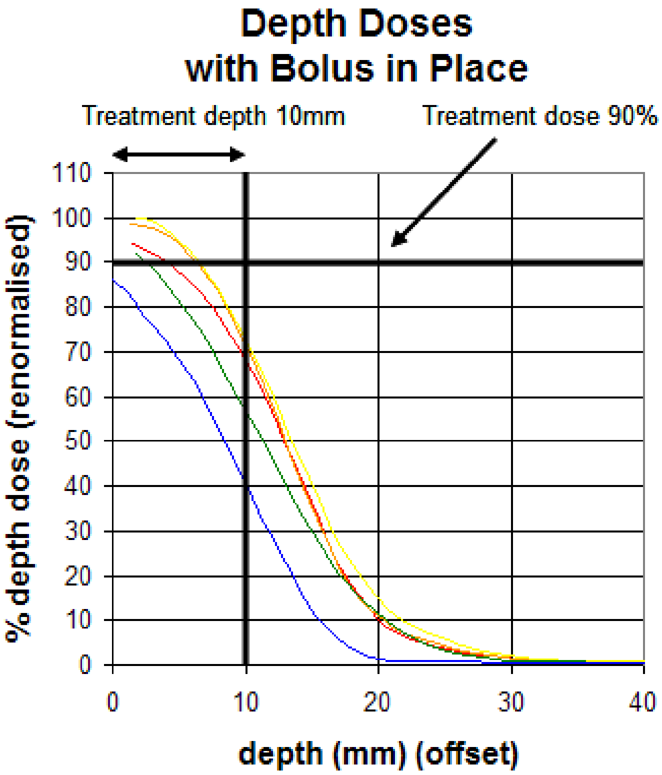

Figure 50: Percentage depth dose curves for a 6MeV electron beam at several points under a mask water phantom overlaid with a 1cm thick layer of wax bolus. The measurements here were obtained using a Scanditronix RFA diode. The depth of the treatment volume (10mm) and the minimum dose required within the treatment volume (90%) are marked.

5.3 Flat Fields

During the recent commissioning of a linac, measured data was entered into the Xio treatment planning system, and the beam models were matched to the measured data. The same commissioning data was used here to verify the Monte Carlo simulations, with the results reported in Section 4. The same linac and quality assurance instruments were used to test the diode array, with the results reported in Section 3. Quality Assurance tests are performed regularly on the linac to detect any deviation from its performance at commissioning.

An additional comparison of the dose distribution to a flat water phan-

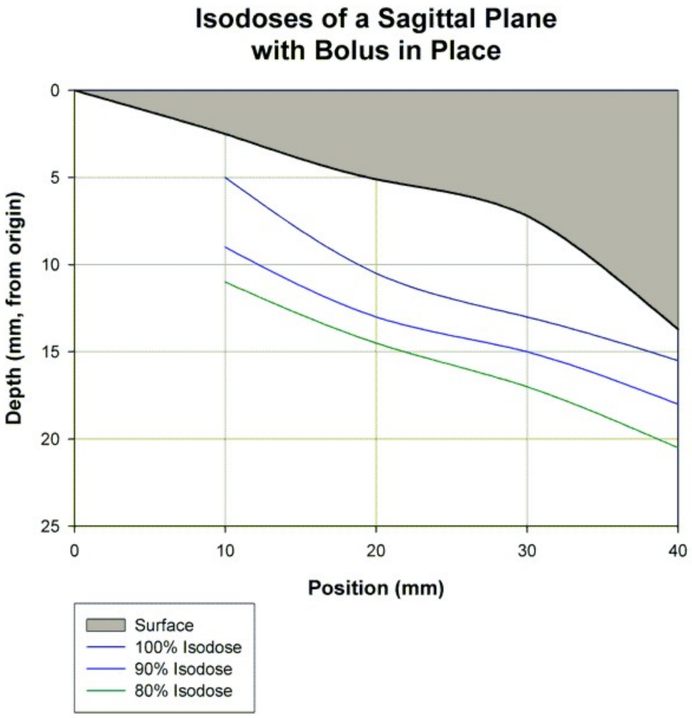

Figure 51: Isodose plot of the midline sagittal plane under a mask water phantom overlaid with a 1cm thick layer of wax bolus in a 6MeV electron beam. The measurements here were obtained using a Scanditronix RFA diode.

tom from electron beams, as measured by the diode array, and simulated by EGS/BEAM and the Xio treatment planning system, was planned. Experimental measurements have been made, and simulations run.

This flat field comparison experiment is now considered unnecessary, given the verification and quality assurance work described above, and can be cancelled without invalidating the other work presented here.

The matching of the Xio pencil beam algorithm to measured data from the linac commissioning is shown in Fig 52. The data was obtained from the Christchurch Oncology Centre Xio RTP system, and is discussed in the linac commissioning report [38]. The pencil beam algorithm parameters were adjusted to achieve the best possible match at d_{max} for each energy at a source-to-surface distance (SSD) of 100cm. Above and below d_{max} the match is not as good.

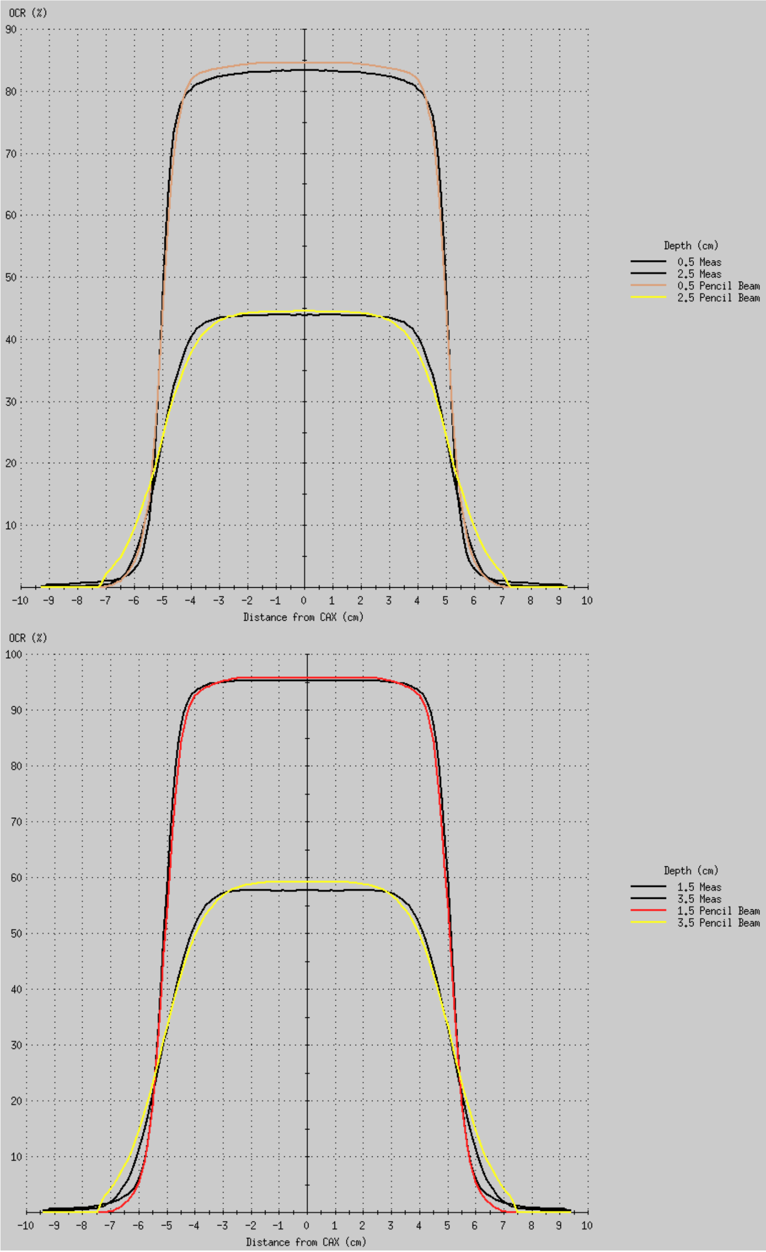

Figure 52: Comparison of the Xio electron pencil beam algorithm with measured data from linac commissioning tests [38]. Both graphs show profiles of $10 \times 10\mathrm{cm}$ beams in flat water phantoms at a source-to-surface distance of 100cm. The upper graph is for a 6MeV electron beam, the lower graph 9MeV. The profile depths are the same as were plotted in the Monte Carlo verification tests (Section 4.2.5).

5.4 Mask Phantom

An experiment was performed comparing the measurement system described in Section 3 (consisting of the diode array and the mask water phantom), the Monte Carlo system described in Section 4 and the CMS Xio treatment planning system.

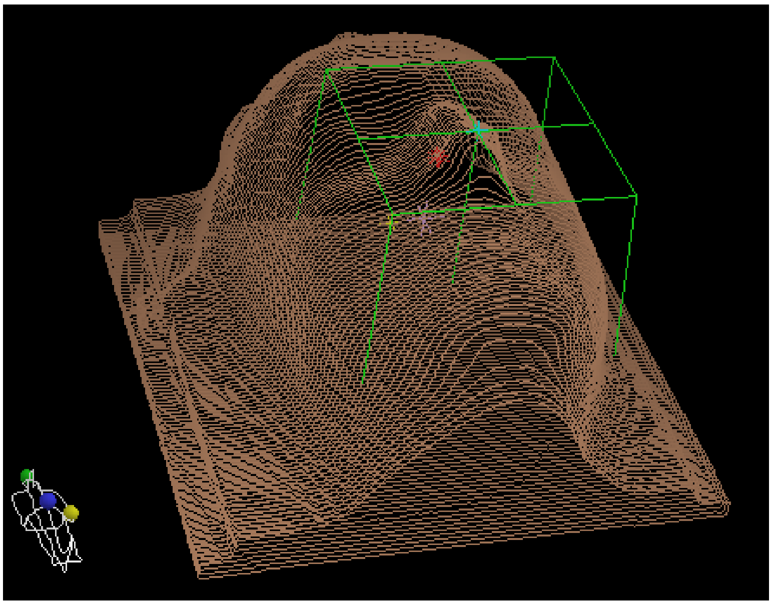

Figure 53: The CT water phantom in Xio. 91 transverse CT images of the phantom were used to form an anatomical datapool in Xio. The Automatic-by-threshold method of contouring was used, where a contour is automatically drawn along a user definable change in CT number. Only the surface contour was required, as the phantom is a homogenous volume of water.

After imaging the phantom by CT, 91 transverse images were used to form an anatomical datapool in Xio. In Xio, the surface contour is mandatory, and defines the volume for dose calculations. Additional contours can be added, delineating organs or other regions of interest. This can be useful for obtaining Dose Volume Histograms from a treatment plan. Here, only the surface contour was required, as the phantom is a homogenous volume of water. The thin plastic mask and perspex base of the phantom were ignored.

Two methods were available for displaying the results from DOSXYZnrc Monte Carlo dose distribution calculations. DOSXYZ_show is distributed

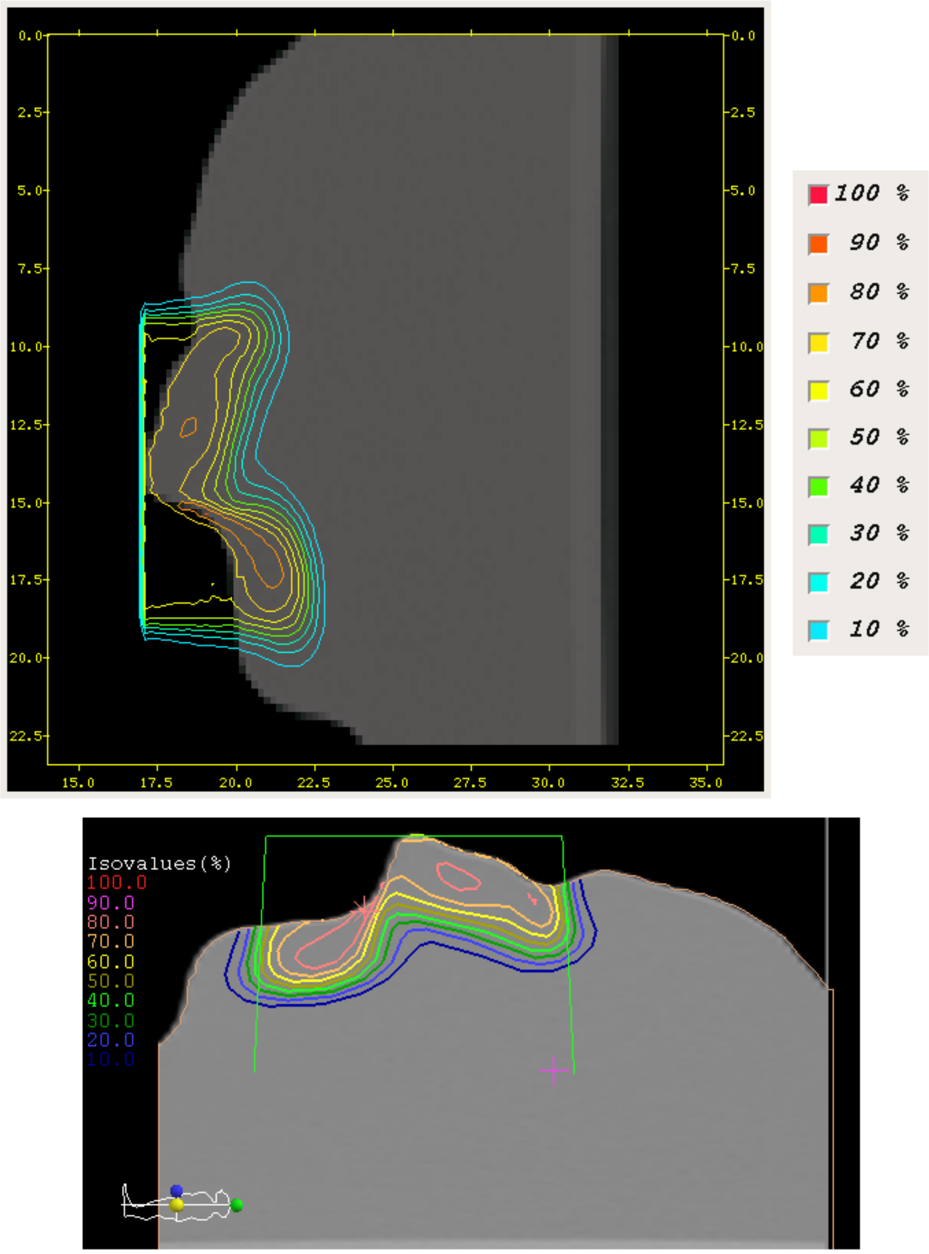

Figure 54: Two isodose plots showing the dose distribution to a sagittal cross section of an irregularly shaped water phantom from a 6MeV, 10×10cm electron beam. This sagittal slice was through the geometric centre of the phantom and the electron beam. The upper plot was generated by DOSXYZ_show. The lower plot was made in CMS Xio. Both were plotted from the same data.

as part of the EGS/BEAM software from NRC. CMS Xio is the conventional treatment planning system used at the Christchurch Oncology Centre. Fig 54 is a comparison of the isodose displays available from these programs.

The upper plot was generated by DOSXYZ_show. The lower plot was made in CMS Xio. Both were plotted from the same data. The differences in the isodose maps, for example, the area encompassed by 80% isodose lines is greater in the Xio plot, may be explained by the programs' use of different coordinate systems. The two plots may not show exactly the same slice of the phantom. This is another reason to import Monte Carlo simulation results into Xio for display and comparison with conventional treatment planning algorithms.

Figs 55, 56, 57 and 58 show the results of the comparison experiment, as isodose graphs. Xio was used to display both the Xio and the EGS/BEAM (DOSXYZnrc user code) results. The diode array data was plotted using a different program, Sigmaplot.

The Monte Carlo dose calculations used linac models with initial electron beam energies that were approximately 250keV lower than optimal, as described in Section 4.2.5. The differences between dose distributions calculated by Xio and EGS/BEAM described here are therefore not reliable. Unfortunately, the Xio hardware and software used in this experiment is no longer available to redo the isodose maps using better Monte Carlo data. Future work using the Matlab-based CERR (Computational Environment for Radiotherapy Research) software may resolve this situation.[39]

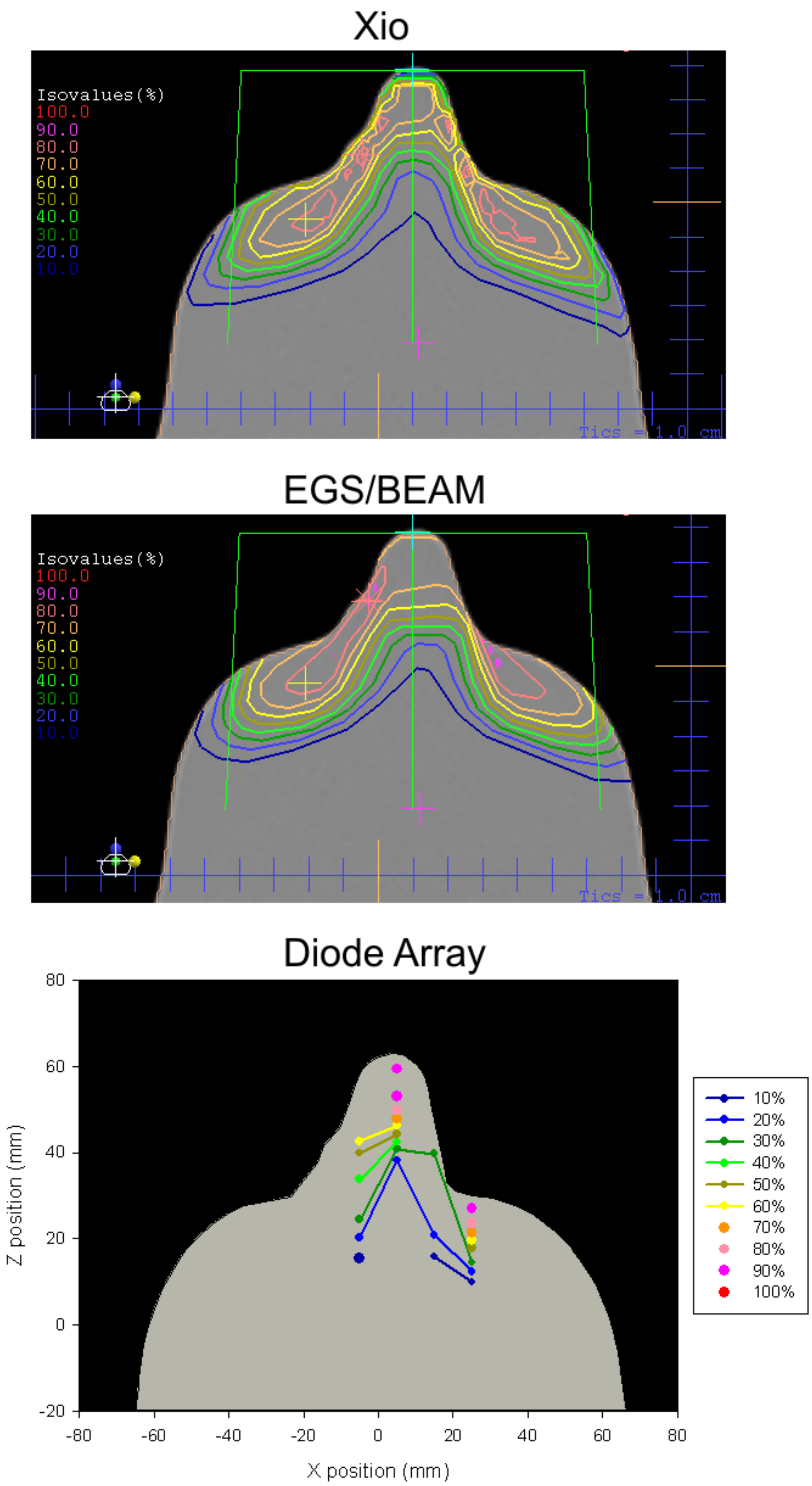

Figure 55: Isodose plots showing the dose distribution to a transverse cross section of an irregularly shaped water phantom from a 6MeV, 10×10cm electron beam. The plots show the dose as calculated by Xio (top) and EGS/BEAM (middle), and as measured using the diode array (bottom). The placement and direction of the incident beam is depicted with fine green lines in the upper two plots.

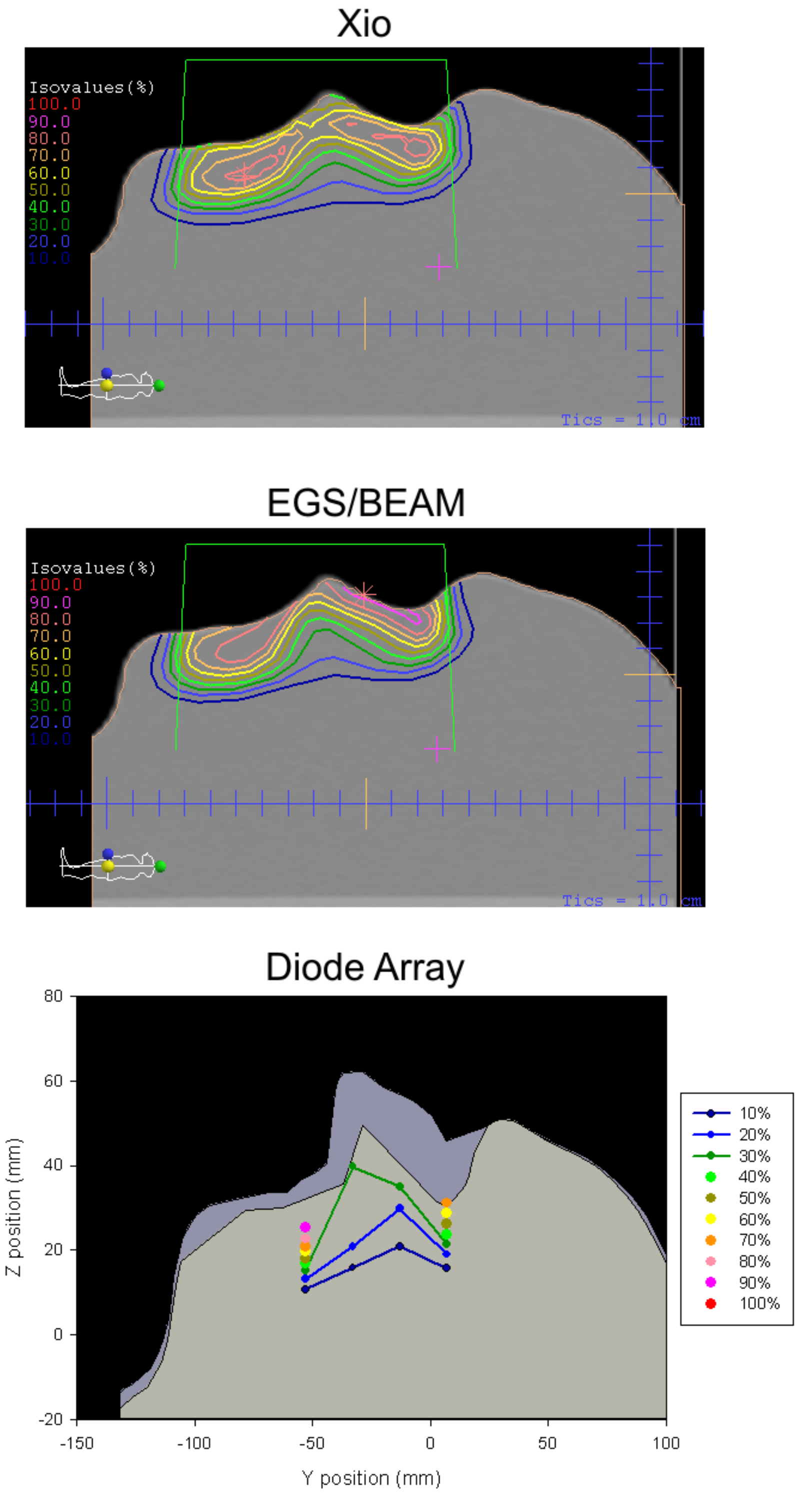

Figure 56: Isodose plots showing the dose distribution to a sagittal cross section of an irregularly shaped water phantom from a 6MeV, 10×10cm electron beam. The plots show the dose as calculated by Xio (top) and EGS/BEAM (middle), and as measured using the diode array (bottom). To better show the position of the slice the isodoses refer to, and because of the low resolution of the surface contour in the diode array plot, the midline surface contour has also been plotted in the background (darker gray).

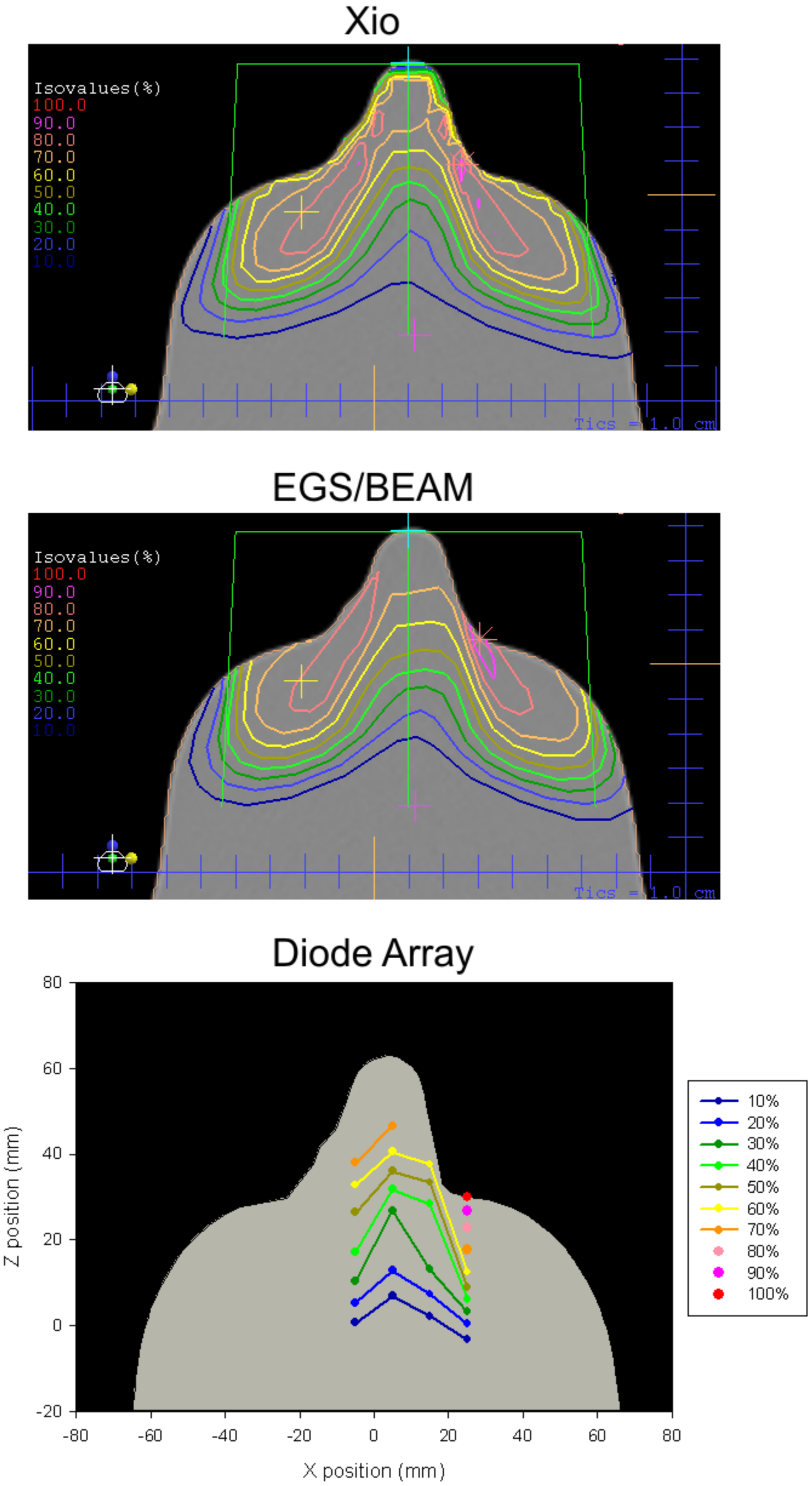

Figure 57: Isodose plots showing the dose distribution to a transverse cross section of an irregularly shaped water phantom from a 9MeV, 10×10cm electron beam. The plots show the dose as calculated by Xio (top) and EGS/BEAM (middle), and as measured using the diode array (bottom).

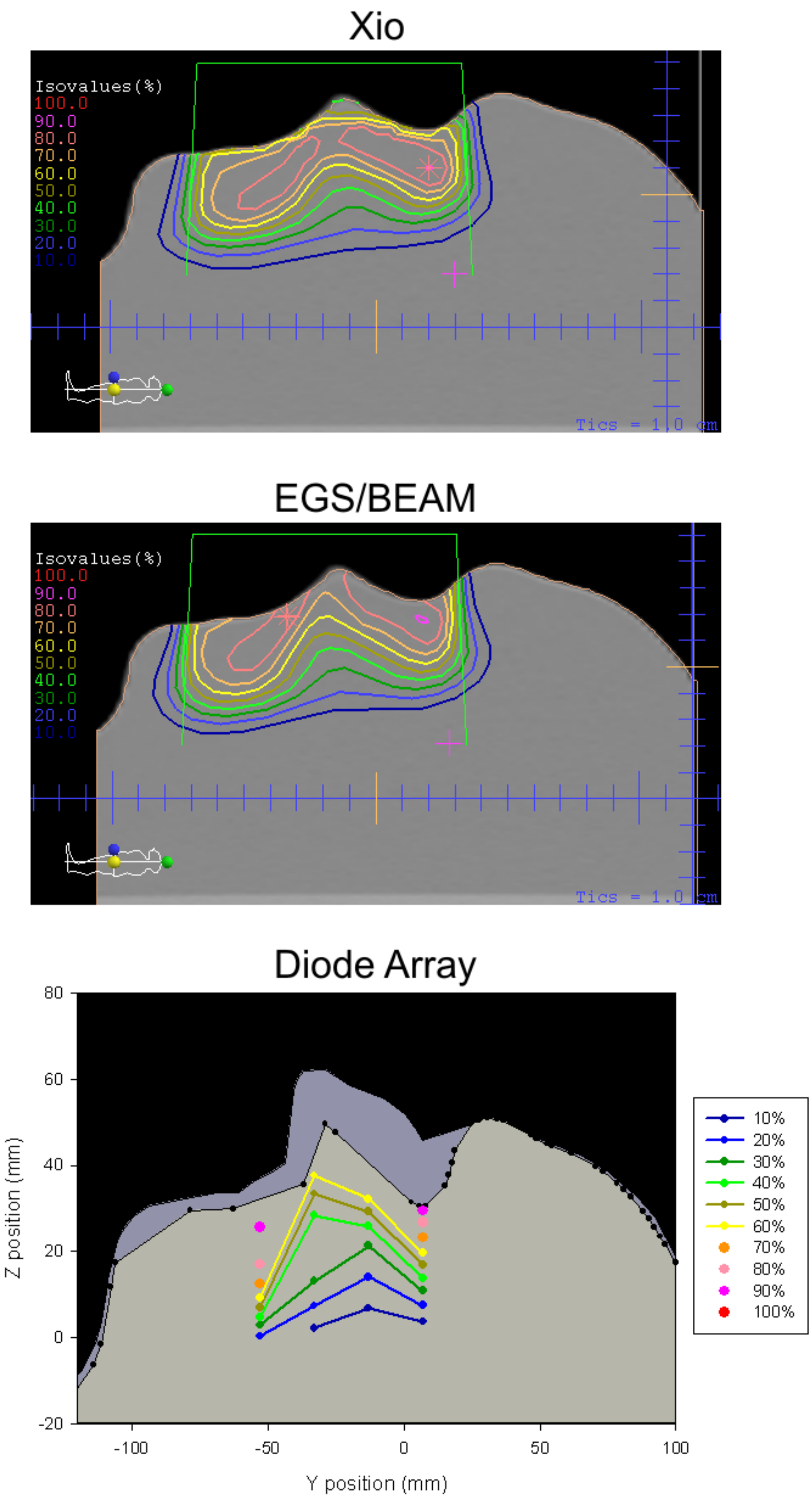

Figure 58: Isodose plots showing the dose distribution to a sagittal cross section of an irregularly shaped water phantom from a 9MeV, 10×10cm electron beam. The plots show the dose as calculated by Xio (top) and EGS/BEAM (middle), and as measured using the diode array (bottom).To better show the position of the slice the isodoses refer to, and because of the low resolution of the surface contour in the diode array plot, the midline surface contour has also been plotted in the background (darker gray).

The dose distributions predicted by Xio and EGS/BEAM differ significantly. EGS/BEAM consistently gives a high dose at the phantom surface, typically 80% of the maximum. Xio predicts a lower dose for the first $\sim$ 5mm of tissue immediately below the surface, with the maximum dose reached somewhat deeper, depending on the shape of the phantom.

The largest disagreements between Xio and EGS/BEAM occur on the nose of the phantom, the most irregularly shaped part of the mask. At the tip of the nose, EGS/BEAM predicts a high dose, while Xio predicts a low dose. The result is reversed on the side of the nose, where the electron beam strikes the phantom at the most oblique angle. Over these small regions, the difference in dose between the Monte Carlo and pencil-beam algorithms can be up to 50%.

EGS/BEAM also consistently reports the beam penumbra to be larger than Xio does, with a higher dose. The dose at the edges of the beam is generally 5-10% higher in EGS/BEAM, and the penumbra several millimetres broader. The differences are greatest where the electron beam is incident on the phantom at a shallow angle. In this experiment, the diode array did not make any measurements in the penumbral region.

The results from the diode array are not yet good enough to be used to determine which of the theoretical models, Monte Carlo or pencil-beam, more accurately predicts the dose distribution in this experiment. The diode array has not produced enough data in this experiment to match the spatial resolution available from the computer models.

The isodose points and lines derived from the diode array measurements are generally consistent with the theoretically predicted results from Xio and EGS/BEAM. In Fig 55, the diode array results are more consistent with the dose distribution calculated by EGS/BEAM, with high doses at the tip of the nose and beside the base of the nose. In Figs 56, 57 and 58 the diode array results are consistent with both theoretical models.

The large volume of data produced by the diode array means that an automated data processing system will be needed for clinical use of the array. The main limitation on the diode array system at the conclusion of this project is the lack of good data processing software. To obtain the isodose maps in Figs 55, 56, 57 and 58, data from the ARANZ Fastscan software and the Pico ADC software had to be combined. This was achieved using a combination of Matlab, Sigmaplot and Excel. A combination of formulae and logic operations in Excel spreadsheets and small programs in Matlab were used to achieve partial automation of the data processing. The Sigmaplot graphing software was used to display the processed results.

6 Conclusion

This project was an initial study of ways to improve the design of custom electron bolus, the planning of electron beam therapy, and other radiation therapy simulation tasks.

Electron beam therapy planning and custom electron bolus design were identified as areas in which improvements in equipment and techniques could lead to significant improvements in treatment delivery and patient outcomes.

6.1 Progress to Date

Equipment for experimental determination of the radiation dose distribution inside irregularly shaped objects has been developed and tested. Section 3 described the design, construction and testing of the diode array. Experiments were performed to prove the concept of an array of inexpensive electronics diodes as an instrument for determining the dose distribution in irregularly shaped water phantoms. The operation of a prototype diode detector and a full array were demonstrated. The capabilities and limitations of the diode detectors and the array were explored. The process of developing this instrument was described.

A Monte Carlo simulation system has been installed, and models of the Christchurch Oncology Centre linacs in the more commonly used electron beam modes have been built and commissioned.

The selection and installation of the EGS/BEAMnrcMP Monte Carlo software, and the process of modelling 6MeV and 9MeV electron beam linacs, was described in Section 4. Linac models were built from information supplied by the manufacturer, Varian, with additional measurements of components from a decommissioned linac. The initial electron beam energy and related parameters were adjusted to obtain matches between the simulations and commissioning data from a Varian 21IX linac.

A test was run comparing the experimental measurement technique using the mask water phantom and the diode array with the EGS/BEAM Monte Carlo system and the CMS Xio conventional treatment planning system. This test was successful as a proof of the concept of the experimental technique. The results were presented and discussed in Section 5. This experiment confirmed that Monte Carlo and pencil-beam algorithms predict significantly different dose distributions to an irregularly shaped object from megavoltage electron beams. The dose distributions measured with the diode array were consistent with the theoretical models.

Fig 59 shows a plan of experiments to intercompare the three systems used here, and possible applications for evaluating treatment plans. At the time of writing, some intercomparison tests from the blue and green groups, and an experiment on custom electron bolus have been performed.

6.2 Future Developments

By the end of this project, the diode array and the water phantom systems were still at an early stage of development, and a lot of additional work will be needed to produce an instrument for clinical use. Some possible directions for future development of these systems are listed below.

Smaller diodes on diode array

Smaller diodes such as the glass enveloped one shown at the top right of Fig 26 could be substituted for the IN4004 diodes currently used in the array, potentially improving spatial resolution and reducing the shielding effects of the electrical contacts and casing material.

Anatomical modifications to masks

A plastic mask filled with water may accurately reproduce the external shape of a patient, but it does not accurately model the internal anatomy of a patient. This is especially true of the head, which contains bones, soft tissue and air spaces.

It may be possible to modify masks to improve the modelling of internal anatomy. An insert, possibly made of aluminium foil, might simulate part of the skull. Foam or air filled capsules might simulate low density tissue and air spaces.

If an organ of interest is significantly larger than the lateral extent of the radiation beam, it could be simulated by a miniphantom mounted on the detector mount and enclosing the detector. Scanning the detector (and miniphantom) across the beam would reveal the effect of the irregular mask shape on the dose to the organ.

Comparison of water phantom CT and real patient CT

A simpler proposition than making an anatomically accurate phantom is using real patient CT data for treatment simulations. Comparing the dose distribution calculated using a patient CT scan with the dose distribution calculated for a water phantom made with a mask of the same patient would

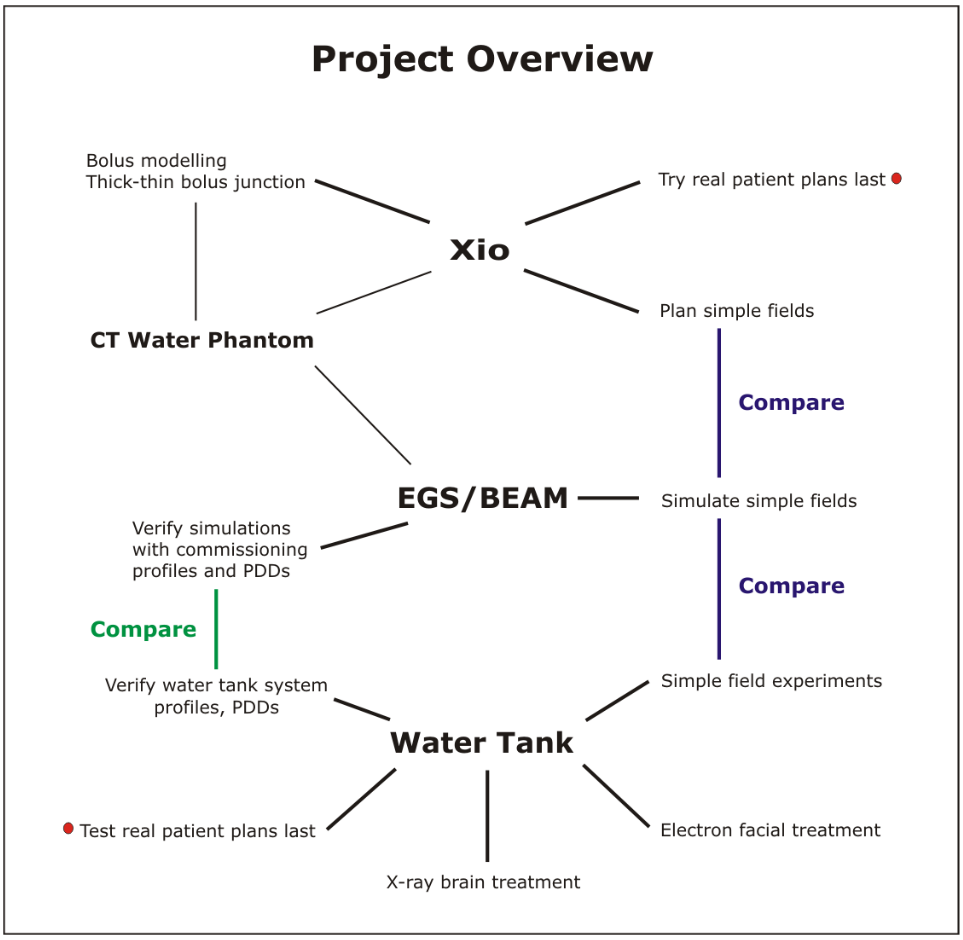

Figure 59: A plan of intercomparisons and experiments for the three dosimetry systems used in this project, CMS Xio, EGS/BEAM and the diode array and water tank system.

reveal the effect of facial bones and the airway and sinuses.

Compensator experiments

Compensators are 0.9mm thick Pb sheets used to improve dose homogeneity by reducing the radiation dose to 'hotspots' found during treatment planning. Each layer of compensator reduces the intensity by $\sim 6\%$. Stacks of irregularly shaped compensators are now being used in conjunction with shields. The water tank system could be used to verify that the effect of these complex assemblies of compensators on the dose distribution is consistent with the treatment planning system predictions.

Op-amp Z-position system

The Z-position system provides a signal compatible with the Pico ADC which allows the height of the diode array to be recorded at each dose measurement. In this project, the Z-position system used a voltage divider. This network of resistors alters the resistance of the RFA detector mount positioning system, potentially a source of error in future experiments.

Replacing the existing Z-position system with one based on operational amplifiers, which have very high input impedance, could improve the characteristics of the system and avoid future problems.

Mushroom miniphantom as buildup cap

The diode array is equipped with 10 detectors. There is an identical, eleventh detector diode which is not built into the array. This diode was intended to be used as a reference detector. A reference detector is held stationary in the radiation beam, so the signal from it is dependent only on changes in the beam, such as variations in the linac output. Taking a ratio of the field detector (in this case the array) signal to the reference signal provides relative dose measurements which are independent of variations in the linac output. Reference detectors used with the Scaditronix water tank are usually positioned in air at the edge of the radiation beam above the tank.

Unfortunately, in air measurements with the reference IN4004 detector diode had high noise. Taking a ratio of the array diode signals to this noisy reference signal would increase the noise and uncertainty in the results. The noisy reference signal is attributed to the lack of buildup material around the diode in air.

The “mushroom” miniphantom designed and built to test the angular dependence of the detector diodes used in the array could be modified for use as a buildup cap for the reference diode. The miniphantom provides 20mm of perspex all around a diode, a suitable thickness of buildup material for all the electron and photon beams available at Christchurch Oncology.

Monte Carlo simulation of a diode radiation detector

The EGS/BEAM Monte Carlo software could be used to simulate various diodes, if the internal structure and composition can be determined. The structure of the IN4004 was determined by abrading the plastic casing with a file (see Figs 26 and 30). The composition of the diode junction semiconductor material has not been established, except that it is silicon-based. It may be more difficult to use such direct methods on a diode with a glass casing.

EGS/BEAM dose distribution format

It is desirable to view the results from Xio, EGS/BEAM and the diode array in the same format. A program to transfer the results of Monte Carlo simulations into Xio plans is already in use. This program reads dose distribution data from .3ddose files written by DOSXYZnrc, and writes a new file in Xio format. If the data processing software for the diode array is developed further, provision could be made to write the dose distribution in .3ddose format, so that the same program used to transfer EGS/BEAM results into Xio could be used with the array.

Monte Carlo computer hardware benchmarking

As an aside to the MC work done in this project, benchmarking the performance of EGS/BEAM on different computer hardware was considered. Specifications for two computers equipped with CPUs from different manufacturers (Intel and AMD) using different processor architectures were composed. These machines would have had as many other components in common as possible, allowing the performance of the CPUs to be compared. However, when the computers were delivered, they did not meet these specifications, and insufficient time remained to run the benchmark tests.

References

[1] ‘Dose calculation - Pencil beam algorithm’; CMS Reference Library; CMS Inc. (2003).

[2] F. Verhaegen, J. Seuntjens; ‘Monte Carlo modelling of external radiotherapy photon beams’; Phys. Med. Biol. **48**, pg R107-R164 (2003).

[3] Hossain M. Deloar; ‘Monte Carlo simulation and its applications to medical physics’; presentation at Medical Physics and Bioengineering Department, Christchurch Hospital, November 2005.

[4] S. C. Klevenhagen; ‘Physics of Electron Beam Therapy’, Medical Physics Handbooks 13; Adam Hilger Ltd (1985).

[5] ‘Convolution’; Wikipedia; http://en.wikipedia.org/wiki/Convolution

[6] R. J. Kudchadker, K. R. Hogstrom, A. S. Garden, M. D. McNeese, R. A. Boyd, J. A. Antolak; ‘Electron conformal radiotherapy using bolus and intensity modulation’; Int. J. Radiation Oncology Biol. Phys., Vol. 53, No. 4, pg. 1023-1037 (2002).

[7] R. J. Kudchadker, J. A. Antolak, W. H. Morrison, P. F. Wong, K. R. Hogstrom; ‘Utilization of custom electron bolus in head and neck radiotherapy’; Journal of Applied Clinical Medical Physics, Vol. 4, No. 4, pg. 321-333, Fall 2003.

[8] Ervin B. Podgorsak (editor); ‘Review of radiation oncology physics: A handbook for teachers and students’; IAEA (2003).

[9] G. H. Perkins, M. D. McNeese, J. A. Antolak, T. A. Buchholz, E. A. Strom, K. R. Hogstrom; ‘A custom three-dimensional electron bolus technique for optimization of postmastectomy irradiation’; Int. J. Radiation Oncology Biol. Phys., Vol. 51, No. 4, pg 1142-1151 (2001).

[10] R. Boyd, K. R. Hogstrom, J. A. Antolak, D. I. Rosenthal; ‘Custom electron bolus treatment planning with skin collimation using the pencil-beam redefinition algorithm’; No. 2139, Proceedings of the 45th annual ASTRO meeting.

[11] D. A. Low, G. Starkschall, S. W. Bujnowski, L. L. Wang, K. R. Hogstrom; 'Electron bolus design for radiotherapy treatment planning: Bolus design algorithms'; Med. Phys. 19 (1), pg. 115-124, Jan-Feb 1992.

[12] S. Babic, A. T. Kerr, M. Westerland, J. Gooding, L. J. Schreiner; 'Examination of Jeltrate Plus as a tissue equivalent bolus material'; Journal of Applied Clinical Medical Physics, Vol. 3, No. 3, pg. 170-175, Summer 2002.

[13] E. M. F. Damen, M. J. P. Brugmans, A. van der Horst, L. Bos, J. V. Lebesque, B. J. Mijnheer, D. L. McShan, B. A. Fraass, M. L. Kessler; 'Planning, computer optimization, and dosimetric verification of a segmented irradiation technique for prostate cancer'; Int. J. Radiation Oncology Biol. Phys., Vol. 49, No. 4, pg 1183-1195 (2001).

[14] B. A. Perrin, T. J. Jordan, A. R. Hounsell; 'The design and evaluation of a phantom for the audit of the treatment chain for prostate radiotherapy'; Radiotherapy and Oncology, 60, pg. 37-43 (2001).

[15] M. M. Glegg; 'Electron dose calculations: a comparison of two commercial treatment planning computers'; Medical Dosimetry, Vol. 28, No. 2, pg. 99-105 (2003).

[16] M. Fippel, F. Haryanto, O. Dohm, F. Nüsslin; 'A virtual photon energy fluence model for Monte Carlo dose calculation'; Med. Phys. 30 (3), pg. 301-311, March 2003.

[17] Daryoush Sheikh-Bagheri, D. W. O. Rogers; 'Sensitivity of megavoltage photon beam Monte Carlo simulations to electron beam and other parameters'; Med. Phys. 29 (3), pg. 379-390, March 2002.

[18] Daryoush Sheikh-Bagheri, D. W. O. Rogers; 'Monte Carlo calculation of nine megavoltage photon beam spectra using the BEAM code'; Med. Phys. 29 (3), pg. 391-402, March 2002.

[19] Daryoush Sheikh-Bagheri; 'Dosimetric evaluation of the clinical implementation of the first commercial IMRT Monte Carlo treatment planning system at 6MV'; Med. Phys. 31 (10), pg2771-2779, Oct 2004.

[20] 'Geant 4'; http://geant4.web.cern.ch/geant4/index.shtml

[21] E. Poon, F. Verhaegen; ‘Accuracy of the photon and electron physics in GEANT4 for radiotherapy applications’; Med. Phys. 32 (6), pg. 1696-1711, June 2005.

[22] Thomson—Nielsen and Medtec websites; www.thomson-elec.com; www.medtec.com

[23] ‘Frequency compensation’; Wikipedia; http://en.wikipedia.org/wiki/Frequency_compensation

[24] P. Horowitz, W. Hill; ‘The art of electronics’; Cambridge University Press (1980).

[25] A. S. Saini, T. C. Zhu; ‘Dose rate and SDD dependence of commercially available diode detectors’; Med. Phys. 31 (4), pg. 914-924, April 2004.

[26] Jie Shi, W. E. Simon, T. C. Zhu; ‘Modelling the instantaneous dose rate dependence of radiation diode detectors’; Med. Phys. 30 (9), pg. 2509-2519, Sep 2003.

[27] I. Griessbach, M. Lapp, J. Bohsung, G. Gademann, D. Harder; ‘Dosimetric characteristics of a new unshielded silicon diode and its applicatio in clinical photon and electron beams’; Med. Phys. 32 (12), pg 3750-3754 (Dec 2005).

[28] ‘Varian Oncology Systems Monte Carlo project’; Varian; confidential information, unpublished.

[29] D. W. O. Rogers, B. Walters, I. Kawrakow; ‘BEAMnrc users manual’, PIRS509; Ionizing Radiation Standards, National Research Council of Canada (2005).

[30] J. A. Griffin; ‘TEAP Module 5: Depth ionisation and depth dose in electron beams’; (unpublished).

[31] D. A. Pinchin; ‘Diode probe service manual’, ‘O.F.E. meter service manual’, ‘Cesium source identifier’.

[32] G. X. Ding, D. W. O. Rogers; ‘Energy spectra, angular spread and dose distributions of electron beams from various accelerators used in radiotherapy’, PIRS439; Institute for National Measurement Standards, National Research Council of Canada (1995).

[33] A. F. Bielajew, H. Hirayama, W. R. Nelson, D. W. O. Rogers; 'History, overview and recent improvements of EGS4', PIRS436; Institute for National Measurement Standards, National Research Council of Canada (1994).

[34] B. Walters, I. Kawrakow, D. W. O. Rogers; 'DOSXYZnrc users manual', PIRS794; Ionizing Radiation Standards, National Research Council of Canada, http://www.irs.inms.nrc.ca/inms/irs/BEAM/beamhome.html (2005).

[35] I. Kawrakow; 'The dose visualization tool *dosxyz_show*'; Ionizing Radiation Standards, National Research Council of Canada, http://www.irs.inms.nrc.ca/inms/irs/BEAM/user_manuals/DISTRIBUTION.html (2005).

[36] D. W. O. Rogers; 'Information needed to simulate a linac using BEAM'; http://www.irs.inms.nrc.ca/inms/irs/BEAM/info_needed_to_model_linac.text (1996).

[37] E. Kunieda, H. M. Deloar, S. Takagi, K. Sato, T. Kawase, H. Saitoh, M. Ozaki, T. Fujisaki, A. Myojoyama, K. Saito, O. Sato, A. Kubo; 'Development of an interface for DOSXYZnrc Monte Carlo dose on Xio RTP system'; Biomedizinische Technik, Vol. 50, Supplementary vol. 1, Part 2 (2005).

[38] M. Bird; 'Treatment 2 - Clinac 21iX commissioning report'; Christchurch Hospital Oncology Service (2006).

[39] http://radium.wustl.edu/CERR/about.php

Appendix

- Radiation detector: Diode and amplifier block diagram
- Radiation detector: Diode and amplifier circuit diagram
- Radiation detector: Detector diodes
- Radiation detector: Diode array mount
- Spherical miniphantom for radiation detector diode
- Matlab program: Collapse_array.m
- Matlab program: Offset.m
- CA3130 operational amplifier datasheet
- IN4004 diode datasheet

01/07/2005
Rev 2

Radiation Detector: Diode and Amplifier Block Diagram

The Diode Radiation Detector System is intended to be a 2D array of diodes, plus a single reference detector. The signals from the detectors are amplified, digitised and logged.

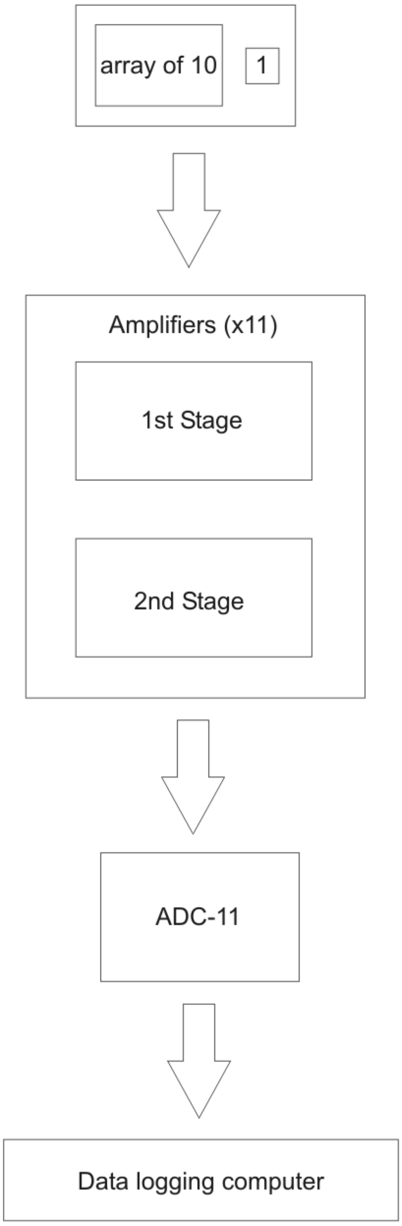

Diode radiation detectors,
array of 10, plus one reference.

Analog signal cable ~1m

1st Stage: Current to voltage,
Amplify and integrate

2nd Stage: Amplify signal
to span ADC input range.

D-25 connector

Analog to Digital Converter
Pico ADC-11

Digital signal cable ~10m
parallel cable.

Parallel port input to Pico data logging software.

Jonathan Griffin
364 1596
jag97@student.canterbury.ac.nz

Radiation Detector: Diode and Amplifier Circuit Diagram

19/10/2005
Rev 3

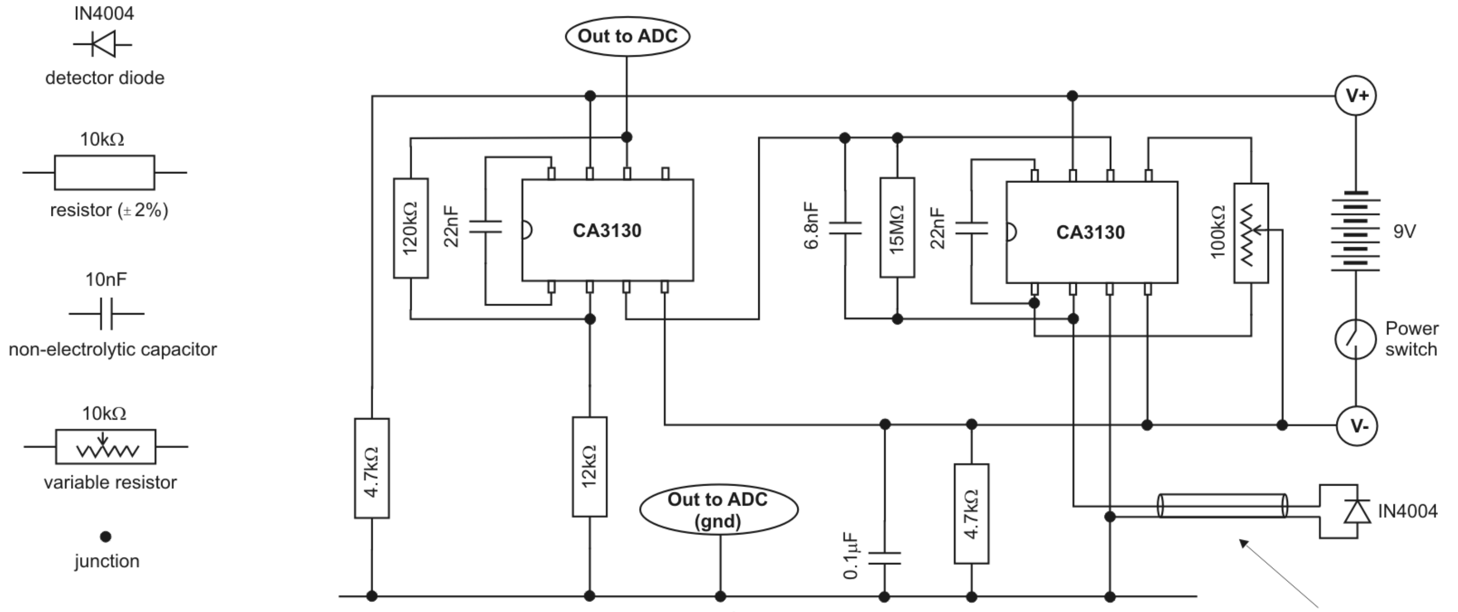

CA3130E or similar op-amp IC

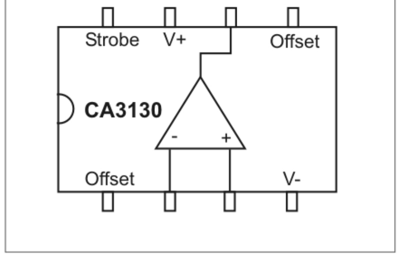

ADC is a Pico TechADC-11
11 inputs
0 - +2.5V input

11 copies of the amplifier, one to each ADC input. →

Output to ADC
25-way male D-type

Pin	Function
1	Digital output
2	Signal ground
3-13	Channels 1-11
14	Aux digital output (not connected)
15-25	Not used

Jonathan Griffin
364 1596
jag97@student.canterbury.ac.nz

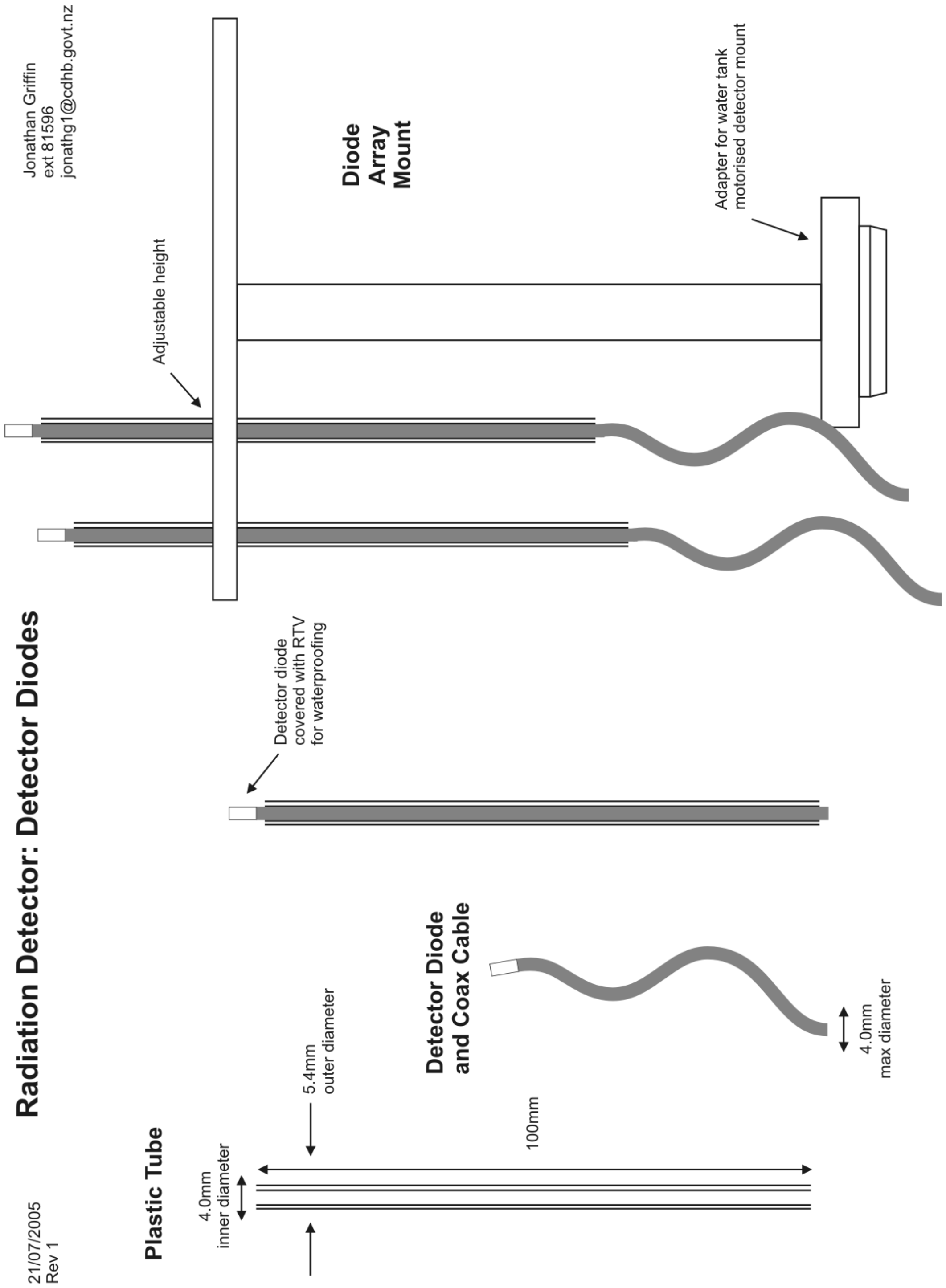
21/07/2005
Rev 1
Radiation Detector: Detector Diodes
Jonathan Griffin
ext 81596
jonathg1@cdhb.govt.nz
Plastic Tube
4.0mm
inner diameter
5.4mm
outer diameter
100mm
Detector Diode
and Coax Cable
4.0mm
max diameter
Detector diode
covered with RTV
for waterproofing
Diode
Array
Mount
Adjustable height
Adapter for water tank
motorised detector mount

19/07/2005
Rev 1

Radiation Detector: Diode Array Mount

Jonathan Griffin
ext 81596
jonathg1@cdhb.govt.nz

Materials all plastic for minimum scatter of radiation.

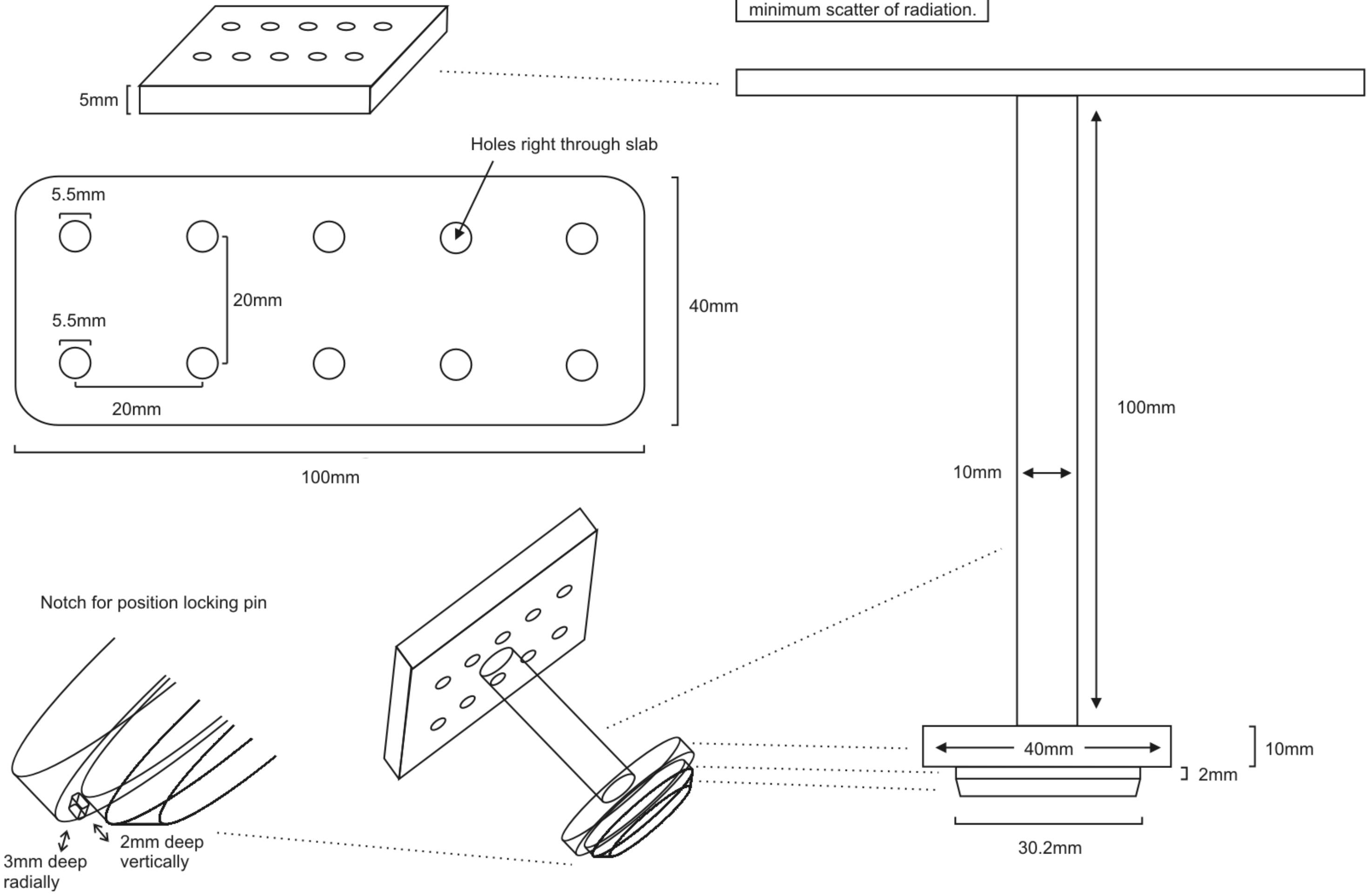

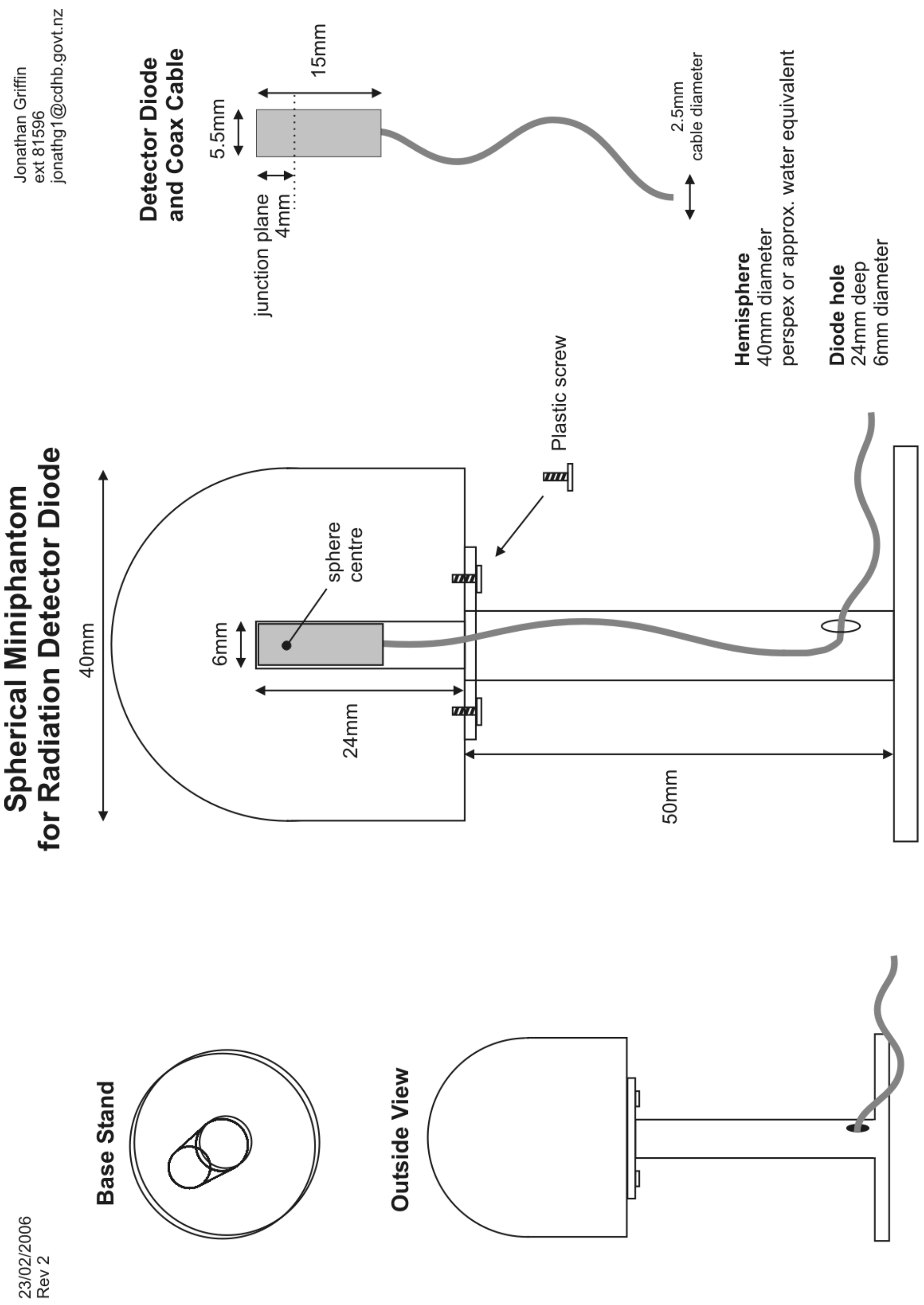
Jonathan Griffin
ext 81596
jonathg1@cdhb.govt.nz
Detector Diode and Coax Cable
15mm
5.5mm
junction plane
4mm
2.5mm cable diameter
Hemisphere
40mm diameter
perspex or approx. water equivalent
Diode hole
24mm deep
6mm diameter
Spherical Miniphantom for Radiation Detector Diode
40mm
sphere centre
6mm
24mm
Plastic screw
50mm
Base Stand
Outside View
23/02/2006
Rev 2

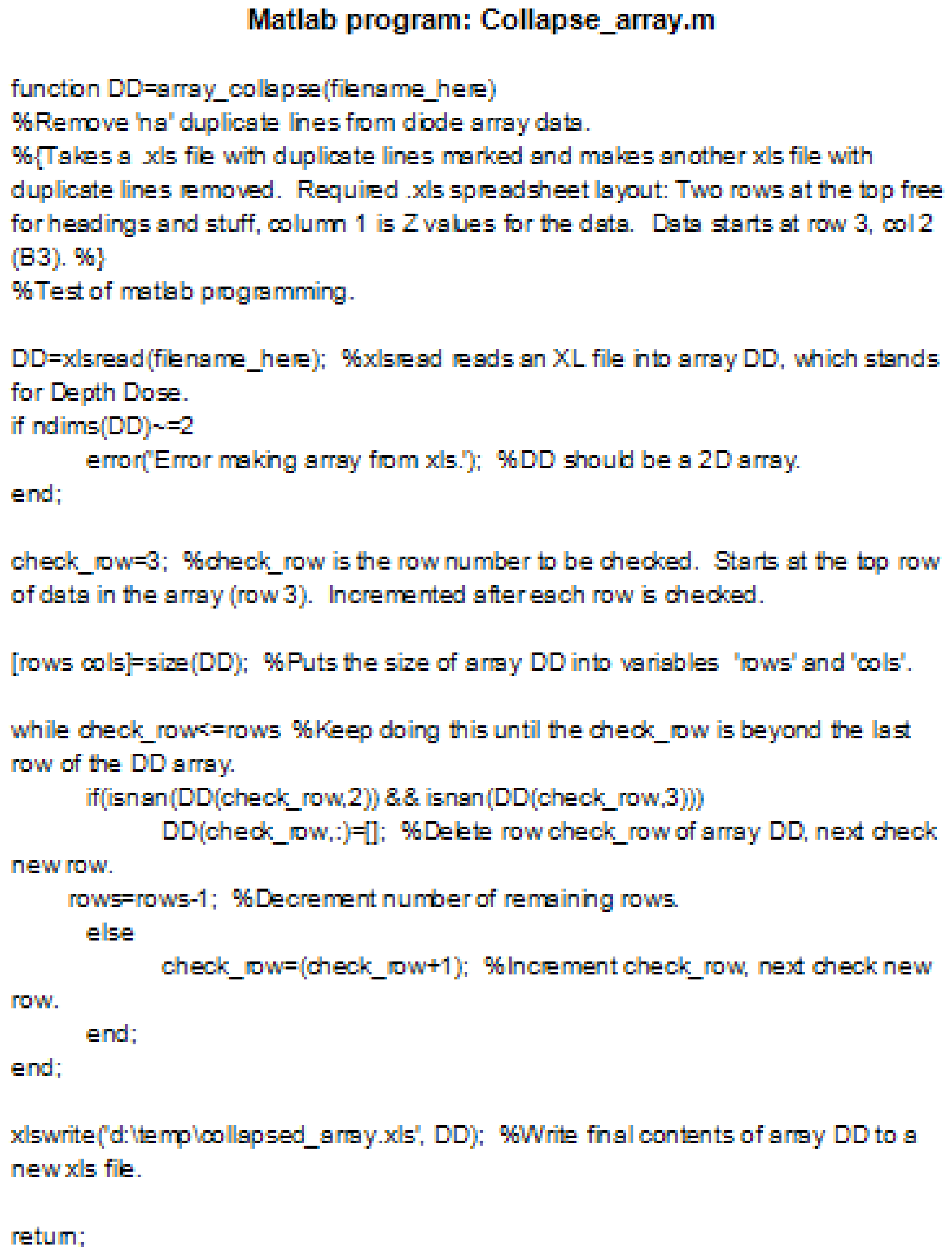

Matlab program: Collapse_array.m

```
function DD=array_collapse(filename_here)
%Remove 'na' duplicate lines from diode array data.
%{Takes a .xls file with duplicate lines marked and makes another xls file with
duplicate lines removed.  Required .xls spreadsheet layout: Two rows at the top free
for headings and stuff, column 1 is Z values for the data.  Data starts at row 3, col 2
(B3). %}
%Test of matlab programming.

DD=xlsread(filename_here);  %xlsread reads an XL file into array DD, which stands
for Depth Dose.
if ndims(DD)~=2
        error('Error making array from xls.');  %DD should be a 2D array.
end;

check_row=3;  %check_row is the row number to be checked.  Starts at the top row
of data in the array (row 3).  Incremented after each row is checked.

[rows cols]=size(DD);  %Puts the size of array DD into variables  'rows' and 'cols'.

while check_row<=rows  %Keep doing this until the check_row is beyond the last
row of the DD array.
        if(isnan(DD(check_row,2)) && isnan(DD(check_row,3)))
                DD(check_row,:)=[];  %Delete row check_row of array DD, next check
new row.
      rows=rows-1;  %Decrement number of remaining rows.
        else
                check_row=(check_row+1);  %Increment check_row, next check new
row.
        end;
end;

xlswrite('d:\temp\collapsed_array.xls', DD);  %Write final contents of array DD to a
new xls file.

return;
```

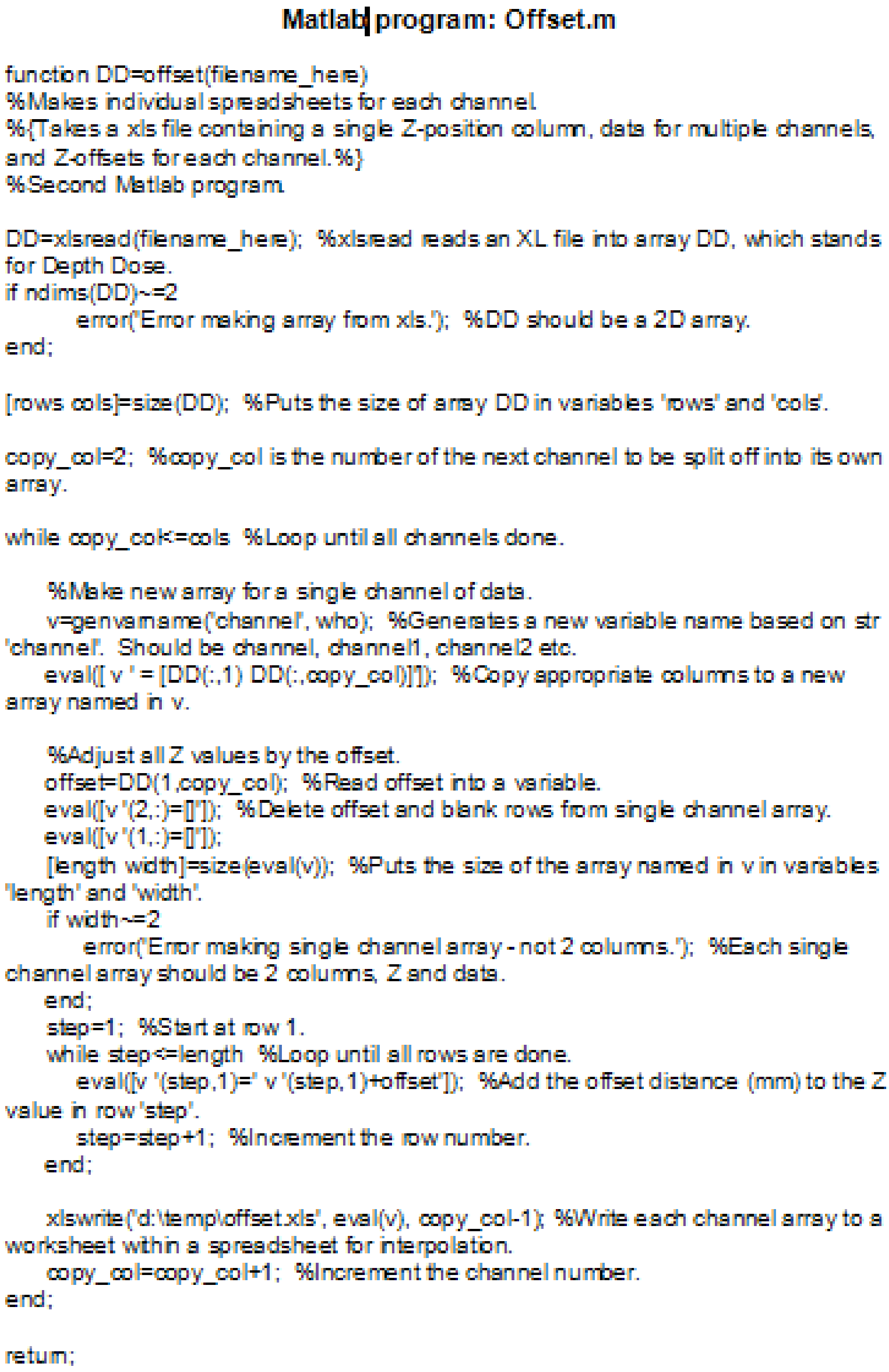

Matlab program: Offset.m

```
function DD=offset(filename_here)
%Makes individual spreadsheets for each channel.
%{Takes a xls file containing a single Z-position column, data for multiple channels,
and Z-offsets for each channel.%}
%Second Matlab program.

DD=xlsread(filename_here);  %xlsread reads an XL file into array DD, which stands
for Depth Dose.
if ndims(DD)~=2
        error('Error making array from xls.');  %DD should be a 2D array.
end;

[rows cols]=size(DD);  %Puts the size of array DD in variables 'rows' and 'cols'.

copy_col=2;  %copy_col is the number of the next channel to be split off into its own
array.

while copy_col<=cols  %Loop until all channels done.

     %Make new array for a single channel of data.
     v=genvarname('channel', who);  %Generates a new variable name based on str
'channel'.  Should be channel, channel1, channel2 etc.
     eval([ v ' = [DD(:,1) DD(:,copy_col)]']);  %Copy appropriate columns to a new
array named in v.

     %Adjust all Z values by the offset.
     offset=DD(1,copy_col);  %Read offset into a variable.
     eval([v '(2,:)=[]']);  %Delete offset and blank rows from single channel array.
     eval([v '(1,:)=[]']);
     [length width]=size(eval(v));  %Puts the size of the array named in v in variables
'length' and 'width'.
     if width~=2
          error('Error making single channel array - not 2 columns.');  %Each single
channel array should be 2 columns, Z and data.
     end;
     step=1;  %Start at row 1.
     while step<=length  %Loop until all rows are done.
         eval([v '(step,1)=' v '(step,1)+offset']);  %Add the offset distance (mm) to the Z
value in row 'step'.
         step=step+1;  %Increment the row number.
     end;

     xlswrite('d:\temp\offset.xls', eval(v), copy_col-1); %Write each channel array to a
worksheet within a spreadsheet for interpolation.
     copy_col=copy_col+1;  %Increment the channel number.
end;

return;
```

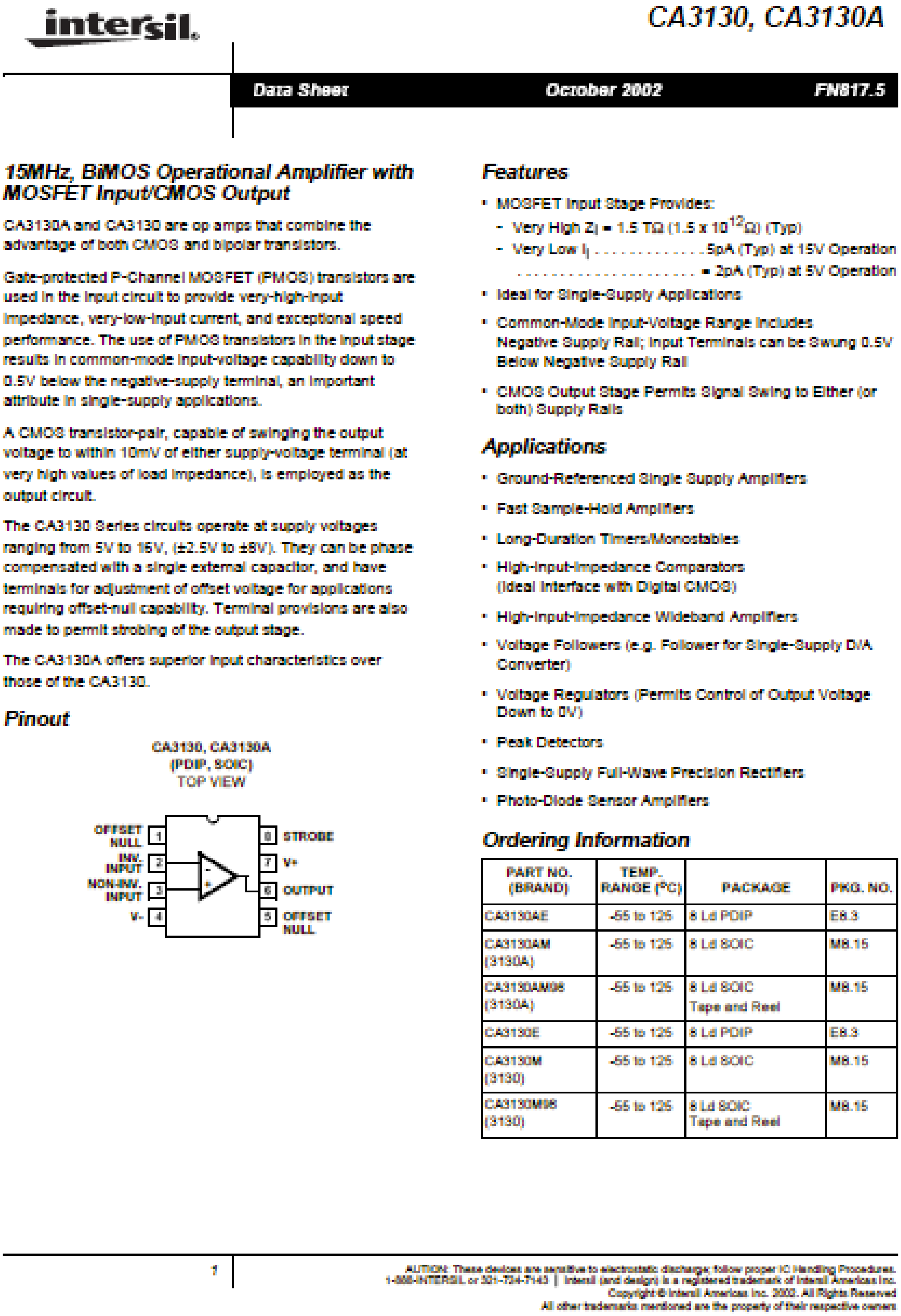

intersil

CA3130, CA3130A

Data Sheet **October 2002** **FN817.5**

15MHz, BiMOS Operational Amplifier with MOSFET Input/CMOS Output

CA3130A and CA3130 are op amps that combine the advantage of both CMOS and bipolar transistors.

Gate-protected P-Channel MOSFET (PMOS) transistors are used in the input circuit to provide very-high-input impedance, very-low-input current, and exceptional speed performance. The use of PMOS transistors in the input stage results in common-mode input-voltage capability down to 0.5V below the negative-supply terminal, an important attribute in single-supply applications.

A CMOS transistor-pair, capable of swinging the output voltage to within 10mV of either supply-voltage terminal (at very high values of load impedance), is employed as the output circuit.

The CA3130 Series circuits operate at supply voltages ranging from 5V to 16V, (±2.5V to ±8V). They can be phase compensated with a single external capacitor, and have terminals for adjustment of offset voltage for applications requiring offset-null capability. Terminal provisions are also made to permit strobing of the output stage.

The CA3130A offers superior input characteristics over those of the CA3130.

Pinout

CA3130, CA3130A
(PDIP, SOIC)
TOP VIEW

Features

- MOSFET Input Stage Provides:
  - Very High Z_I = 1.5 TΩ (1.5 x 10^{12}Ω) (Typ)
  - Very Low I_I . . . . .5pA (Typ) at 15V Operation
    . . . . = 2pA (Typ) at 5V Operation
- Ideal for Single-Supply Applications
- Common-Mode Input-Voltage Range Includes Negative Supply Rail; Input Terminals can be Swung 0.5V Below Negative Supply Rail
- CMOS Output Stage Permits Signal Swing to Either (or both) Supply Rails

Applications

- Ground-Referenced Single Supply Amplifiers
- Fast Sample-Hold Amplifiers
- Long-Duration Timers/Monostables
- High-Input-Impedance Comparators (Ideal Interface with Digital CMOS)
- High-Input-Impedance Wideband Amplifiers
- Voltage Followers (e.g. Follower for Single-Supply D/A Converter)
- Voltage Regulators (Permits Control of Output Voltage Down to 0V)
- Peak Detectors
- Single-Supply Full-Wave Precision Rectifiers
- Photo-Diode Sensor Amplifiers

Ordering Information

PART NO. (BRAND)	TEMP. RANGE (°C)	PACKAGE	PKG. NO.
CA3130AE	-55 to 125	8 Ld PDIP	E8.3
CA3130AM (3130A)	-55 to 125	8 Ld SOIC	M8.15
CA3130AM96 (3130A)	-55 to 125	8 Ld SOIC Tape and Reel	M8.15
CA3130E	-55 to 125	8 Ld PDIP	E8.3
CA3130M (3130)	-55 to 125	8 Ld SOIC	M8.15
CA3130M96 (3130)	-55 to 125	8 Ld SOIC Tape and Reel	M8.15

1

AUTION: These devices are sensitive to electrostatic discharge; follow proper IC Handling Procedures.
1-888-INTERSIL or 321-724-7143 | Intersil (and design) is a registered trademark of Intersil Americas Inc.

1N4001 THRU 1N4007

GENERAL PURPOSE PLASTIC RECTIFIER

***Reverse Voltage** - 50 to 1000 Volts* ***Forward Current** - 1.0 Ampere*

DO-204AL

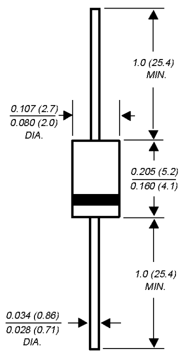

NOTE: *Lead diameter is* $\frac{0.026\ (0.66)}{0.023\ (0.58)}$ *for suffix "E" part numbers*

Dimensions in inches and (millimeters)

FEATURES

- ♦ The plastic package carries Underwriters Laboratory Flammability Classification 94V-0
- ♦ Construction utilizes void-free molded plastic technique
- ♦ Low reverse leakage
- ♦ High forward surge current capability
- ♦ High temperature soldering guaranteed: 250°C/10 seconds, 0.375" (9.5mm) lead length, 5 lbs. (2.3kg) tension

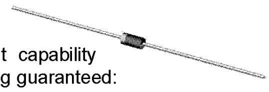

MECHANICAL DATA

Case: JEDEC DO-204AL molded plastic body

Terminals: Plated axial leads, solderable per MIL-STD-750, Method 2026

Polarity: Color band denotes cathode end

Mounting Position: Any

Weight: 0.012 ounce, 0.3 gram

MAXIMUM RATINGS AND ELECTRICAL CHARACTERISTICS

Ratings at 25°C ambient temperature unless otherwise specified.

	SYMBOLS	*1N 4001*	*1N 4002*	*1N 4003*	*1N 4004*	*1N 4005*	*1N 4006*	*1N 4007*	*UNITS*
*Maximum repetitive peak reverse voltage	V_{RRM}	50	100	200	400	600	800	1000	Volts
*Maximum RMS voltage	V_{RMS}	35	70	140	280	420	560	700	Volts
*Maximum DC blocking voltage	V_{DC}	50	100	200	400	600	800	1000	Volts
*Maximum average forward rectified current 0.375" (9.5mm) lead length at T_A=75°C	$I_{(AV)}$	1.0							Amp
*Peak forward surge current 8.3ms single half sine-wave superimposed on rated load (JEDEC Method) T_A=75°C	I_{FSM}	30.0							Amps
*Maximum instantaneous forward voltage at 1.0A	V_F	1.1							Volts
*Maximum full load reverse current full cycle average 0.375" (9.5mm) lead length at T_L=75°C	$I_{R(AV)}$	30.0							µA
*Maximum DC reverse current at rated DC blocking voltage	T_A= 25°C T_A=100°C	I_R	5.0 50.0						µA
Typical reverse recovery time (NOTE 1)	t_{rr}	30.0							µs
Typical junction capacitance (NOTE 2)	C_J	15.0							pF
Typical thermal resistance (NOTE 3)	$R_{\Theta JA}$ $R_{\Theta JL}$	50.0 25.0							°C/W
Maximum DC blocking voltage temperature	T_A	+150							°C
*Operating junction and storage temperature range	T_J, T_{STG}	-50 to +175							°C

NOTES:

(1) Measured on Tektronix Type "S" recovery plug-in. Tektronix 545 Scope or equivalent, I_{FM}=20mA, I_{RM}=1mA

(2) Measured at 1.0 MHz and applied reverse voltage of 4.0 Volts

(3) Thermal resistance from junction to ambient and from junction to lead at 0.375" (9.5mm) lead length, P.C.B. mounted

*JEDEC registered value

GENERAL
SEMICONDUCTOR

RATINGS AND CHARACTERISTIC CURVES 1N4001 THRU 1N4007

FIG.1 - FORWARD CURRENT DERATING CURVE

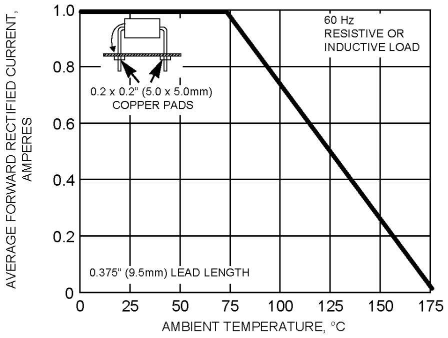

FIG. 2 - MAXIMUM NON-REPETITIVE PEAK FORWARD SURGE CURRENT

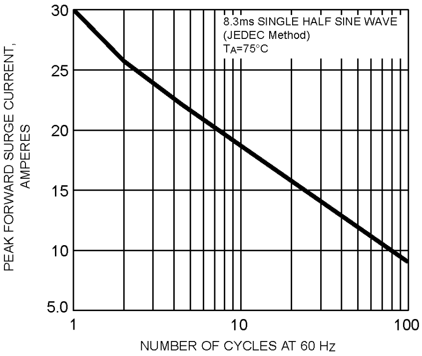

FIG. 3 - TYPICAL INSTANTANEOUS FORWARD CHARACTERISTICS

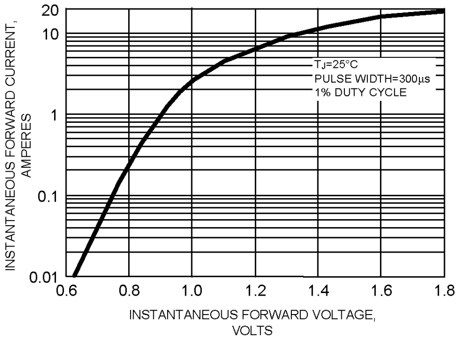

FIG. 4 - TYPICAL REVERSE CHARACTERISTICS

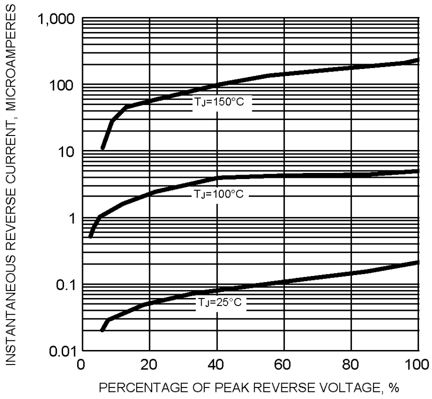

FIG. 5 - TYPICAL JUNCTION CAPACITANCE

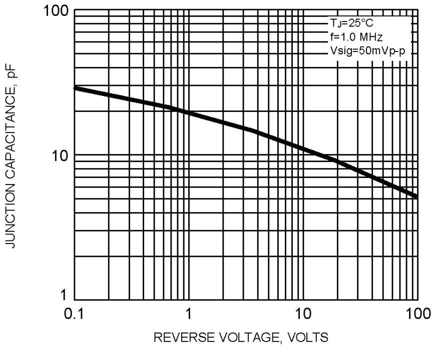

FIG. 6 - TYPICAL TRANSIENT THERMAL IMPEDANCE

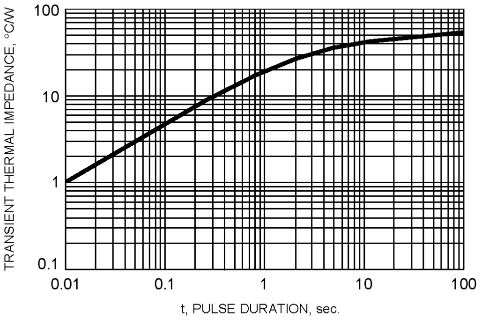

GENERAL
SEMICONDUCTOR